Lipid Speciation and Ion Interactions at the Air-Aqueous Interface in Atmospheric Aerosol Model Systems

DISSERTATION

Presented in Partial Fulfillment of the Requirements for the Degree Doctor of Philosophy
in the Graduate School of The Ohio State University

By
Ting Zhang
Graduate Program in Chemistry

The Ohio State University
2018

Dissertation Committee:
Prof. Heather C. Allen, Advisor
Prof. Terry L. Gustafson
Prof. Abraham Badu-Tawiah

Abstract

Sea spray aerosols (SSA) are known to influence the climate directly by affecting the absorption and scattering of solar radiation and, indirectly, by acting as cloud condensation nuclei and ice nuclei. The chemical composition of SSA is driven by organic species and ions present in the sea surface microlayer (SSML), the organic film that coats the ocean surface. These organics are taken up into SSA and affect aerosol climate properties such as hygroscopicity and albedo. In addition, metal ions have been shown to alter the surface organization, speciation, and solubility of organic surfactants. Thus understanding the surface behavior of organics in SSA in response to factors including but not limited to surface area, pH and interactions with cations is necessary to fully realize the impact of SSA on climate.

Langmuir monolayers of dipalmitoylphosphatidic acid (DPPA), a simple surfactant phospholipid, are utilized as proxies for studying the organic coating at the ocean surface and on marine aerosols. There are two themes of study in this work. The first theme addresses selectivity of metal cations binding to organics at the ocean surface resulting in enrichment in the sea surface microlayer (SSML) and sea spray aerosol (SSA), and their impact on surface properties upon binding. The second theme addresses the phenomena that speciation of organics is different at interfaces such as the SSML and surface of SSA. The speciation of organic surfactants on SSA is considered to be an important factor controlling the interfacial and climate properties of SSA. However, correctly predicting the surface speciation requires the determination of the surface dissociation constants (surface-pK_a) of the protic functional group(s) present.

Phase behavior, stability, and surface morphology of DPPA films with and without metal cations were studied using surface pressure compression isotherms and imaged with Brewster angle Microscopy (BAM). The surface speciation of DPPA was studied using surface tension pH titration. The binding interactions of DPPA with cations was further investigated using surface tension salt titration. Finally infrared reflection-absorption spectroscopy (IRRAS) was utilized to probe the molecular level structure and interaction of DPPA with and without metal cations.

To explore metal enrichment selectivity, a systematic metal cation affinity study on surfactant lipids containing various functional headgroups (-OH, $-H_2PO_4$, -COOH, $-N(CH_3)_2$) was conducted. DPPA is a model lipid for studying a phosphate headgroup. The phosphate headgroup is observed to exhibit the strongest trace metal binding, followed by the carboxylate headgroup. Hydroxide and dimethylammonium headgroups does not exhibit significant trace metal binding. Thus DPPA is determined to have the greatest impact on trace metal enrichment.

The impact of pH and cations on phase behavior, stability, and surface morphology of DPPA was further investigated. At $pH < 10$, DPPA monolayers on water are found to be predominantly neutral species and display the highest packing density. Cations are qualitatively found to expand and stabilize the monolayer in the following order of increasing magnitude at pH 5.6: $Na^+ > K^+ \sim Mg^{2+} > Ca^{2+}$. Additionally, cation complexation is tied to the pH and protonation state of DPPA, which are the primary factors controlling the monolayer surface behavior. The binding affinity of cations to the headgroup and thus deprotonation capability of the cation, is ranked in the order of $Ca^{2+} > Mg^{2+} > Na^+ > K^+$. Nucleation of surface 3D lipid structures is observed from Ca^{2+}, Mg^{2+}, and Na^+, but not from K^+, consistent with the lowest binding affinity of K^+.

A more expansive and quantitative order of metal cation binding affinities to phosphatidic acid was investigated using the Langmuir- Szyszkowski model. The order of affinity strength is quantitatively determined to be: $Al^{3+} > Fe^{3+} \sim> Zn^{2+} > Mg^{2+} > Ni^{2+} > Mn^{2+} \sim Ca^{2+}$, an order not predicted from molecular area expansion nor bulk properties such as solid formation constants of metal-phosphonates.

Finally, the pK_a to remove the second proton of DPPA (surface-pK_{a2}) at the aqueous interface was investigated by examining the molecular area expansion at basic pH, In addition, the vibrational modes of the phosphate headgroup were directly probed and the stretches assigned to understand DPPA charge speciation with increasing pH. Results show that a condensed DPPA monolayer has a surface-pK_{a2} of 11.5, a value higher than previously reported (~7.9–8.5). This surface-pK_{a2} is further altered by the presence of Na^+ cations in the aqueous subphase, which reduced the surface-pK_{a2} from 11.5 to 10.5. It is also found that the surface-pK_{a2} value of DPPA is modulated by the packing density (i.e., the surface charge density) of the monolayer, with a surface-pK_{a2} as low as 9.2 for DPPA monolayers in the 2D gaseous phase over NaCl solutions. The experimentally determined surface-pK_{a2} values are also in good agreement with those predicted by Gouy-Chapman theory, validating these methods and showing that surface charge density is the driving factor behind changes to the surface-pK_{a2}.

These studies signify that phospholipids such as DPPA are significant source of trace metal enrichment within the SSML and SSA. The environment dependent speciation of DPPA further shows that the interfacial properties of SSA are significantly impacted by the presence of an organic coating and ions. Thus all these factors must be taken into consideration when attempting to understand the impact of SSA on climate and the environment.

Acknowledgements

I would like to acknowledge my advisor Prof. Heather C. Allen for her guidance and mentorship over the course of my time at The Ohio State University. I would also like to especially thank Dr. Dominique Verreault for his guidance and mentorship as well through my graduate studies. I am also thankful to all the Allen Lab group members past and present whom I’ve learned from and worked with, particularly Dr. Dana-Marie Telesford, Dr. Ellen Adams, Bethany Rudd, and Jennifer Neal, as well as my undergraduate researchers Matthew Cathcart, Raja Dhankani, and Michelle Fiamingo. Finally I would like to thank my friends and wonderful wife Xun Shi for their continued support outside of lab.

Vita

2012………………………………………	B.S. Chemistry, College of William & Mary
2014………………………………………	M.S. Chemistry, The Ohio State University, Columbus, OH, USA
2012 – Present……………………………	Graduate Teaching Associate, Department of Chemistry and Biochemistry, The Ohio State University
2015 – Present………………………….....	Graduate Research Associate, Department of Chemistry and Biochemistry, The Ohio State University

Publications

- Hogg, D.; Alfeeli, B.; Hoover, A.; Zhang T.; Rice, G.; Agah, M., "Trace organics monitoring in drinking water using Tenax-coated fibers," Sensors, 2011 IEEE, 2011, 1093-1096.
- Zhang, T.; Cathcart M.G; Vidalis, A.S.; Allen H.C., "Cation effects on phosphatidic acid monolayers at various pH conditions" Chemistry and Physics of Lipids, 2016, 200, 24-31.
- Zhang, T.; Brantley S.; Verreault D.; Dhankani R. Corcelli S.A.; Allen H.C., "Effect of pH and Salt on Surface pKa of Phosphatidic Acid Monolayers" Langmuir, 2018, 34 (1), 530–539
- Zhang, T.; Fiamingo M.; Allen H.C., "Trace Metal Enrichment driven by Phosphate Functional Group Binding Selectivity" Journal of Geophysical Research: Oceans, 2018, [submitted]

Field of Study

Major Field: Chemistry

Table of Contents

List of Figures

List of Tables

List of Abbreviations and Symbols

Abbreviations

BAM	Brewster angle microscopy
DAG	1,2-dipalmitoyl-sn-glycerol
DAP	1,2-dipalmitoyl-3-dimethylammonium-propane
DFT	Density functional theory
DMPA	Dimyristoylphosphatidic acid
DPPA	Dipalmitoylphosphatidic acid
DPPC	Dipalmitoylphosphatidylcholine
EM-CCD	Electron multiplying charge coupled device
FTIR	Fourier Transform Infrared
G	Gaseous
GC	Gouy-Chapman
HPLC	High pressure liquid chromatography
IR	Infrared
IRRAS	Infrared reflection-absorption spectroscopy
L	Liquid
LC	Liquid-condensed
LE	Liquid-expanded
MMA	Mean molecular area
RA	Reflectance-absorbance

SA	Stearic acid
SP	Surface pressure
SSA	Sea spray aerosol(s)
SSML	Sea surface microlayer
STST	Surface tension salt titration
TC	Tilted-condensed
UC	Untilted-condensed

Symbols

UC	Untilted-condensed
Π-A	Surface pressure-area
R_p	p-polarized reflectance
R_s	s-polarized reflectance
λ	wavelength
Π-Ax	Surface pressure-area
Π	Surface pressure
Γ	Surface excess
K	Surface adsorption constant
R_p	p-polarized reflectance
R_s	s-polarized reflectance
λ	Wavelength
γ_o	Surface tension of neat water
γ_m	Surface tension of the monolayer

γ	Surface tension of solution
θ_i	Incident angle.
θ_r	Refracted angle
$\tilde{r}$	Complex reflection coefficient
n_i	Refractive index of incident medium
n_t	Refractive index of refracted medium
R	Reflectance of aqueous surface
R_0	Reflectance of monolayer
n_{mx}	Complex monolayer refractive index perpendicular to surface normal
n_{mz}	Complex monolayer refractive index parallel to surface normal
h	Monolayer thickness
ψ_0	Surface potential
T	Temperature
R	Ideal gas constant
F	Faraday constant
σ_0	Maximal surface charge density
e	Electronic charge
A_L	Lipid area
ε_0	Vacuum permittivity
ε_r	Relative permittivity of aqueous phase
C_b	Bulk ion concentration
C	Concentration

Chapter 1. Introduction

1.1 Motivation

The ocean is the largest source of aerosol emissions, releasing an estimated 2-100 x 10^{15} g of sea spray aerosols (SSA) per year.[1] SSAs are known to impact climate directly through light scattering and absorption, and indirectly by acting as cloud condensation nuclei and ice nuclei.[2-7] SSA are produced in varying sizes through bubble bursting and wave breaking, and in the process, incorporate oceanic ions and organics from the sea surface microlayer (SSML), the organic layer that coats the ocean surface ocean surface.[8-16] It has been shown that organics affect SSA particle size distributions which in turn impact their climate altering properties. [11, 17] In addition, metal ions have also been shown to alter the surface organization, speciation, and solubility of organic species in SSA. [8, 18-19]

The presence of a mixed organic coating complexed with inorganic ions at the surface of sea spray aerosols alters not only their optical properties but other properties such as hygroscopicity, i.e., an aerosol's capacity to attract water molecules. As marine aerosols have regional distributions of ions and organic matter that can be distinctly different, they will have, as stated by Elliott et al.: "[…] *different critical organic parameters not limited to interfacial coverage, the two dimensional phase state, chemically dependent hygroscopicities, mass to carbon ratio and even density.*"[13, 20-21] These parameters critically affect aerosol climate activity including aerosol growth and volatility, radiative absorption and scattering, reactivity with atmospheric gases, and cloud condensation nuclei activity [6, 22-27].

Interestingly, this complexity is generally not modeled in current atmospheric simulations as primary organic aerosols are still treated as uniform, and differences in aerosol size and hygroscopicity due to organic matter are typically neglected.[22] Thus understanding the surface properties of model organic films with environmentally-relevant ions at air-aqueous interfaces will help to improve atmospheric aerosol climate modeling.

In addition, while there have been recent studies that revealed the impact of salt concentrations and organics on these properties, there is a paucity of data on pH effects and surface speciation of common organic surfactants relevant to sea spray aerosols.[28-30] A recent study by Freedman et al. showed that the protonation state of organic molecules on aerosol particles affects their solubility, that then directly influences the aerosols' hygroscopic properties including efflorescence, deliquescence, phase separation and mixing transitions.[17] Thus, knowledge of the surface speciation of an organic molecule is relevant to understanding its impact on the sea spray aerosol properties.

In that regard, dipalmitoylphosphatidic acid (DPPA) monolayers can be useful and relevant proxy systems for the SSML and organic coatings on marine aerosol surfaces.[31] DPPA constitutes a simple lipid model consisting of a phospholipid with two C_{16} length alkyl tails and a single phosphate headgroup, but has great biological importance in cell membranes. Although it exists in small amounts (~1%) due to its high turnover rate, DPPA is crucial for the maintenance of cell membranes as it is a key metabolite in the synthesis and breakdown of larger membrane phospholipids in addition to participating in other important cellular functions, e.g., vesicle fission and fusion, cell signaling, and protein binding rate. [32-37] Besides being a minor phospholipid in the cell membranes of mammals and plants, DPPA is also known to be widely distributed among different species of marine microorganisms and has been found in SSA.[38-40] DPPA is also a source of other marine relevant lipids such as dipalmitoylphosphatidylcholine, and decomposes into C_{16} saturated fatty acids which are among the most abundant fatty acids found in both SSML and SSA.[41-43] Thus we selected DPPA as an relevant and ideal simple model system for studying the effects of speciation and ions on lipid surface behavior and morphology, including alkyl chain conformation, hydration state, and ion interactions with the phosphate headgroup at air-aqueous interfaces.

1.2 Dissertation Highlights

Chapter 2 covers the basic theory required for practical application and understanding of surface tensiometry, Brewster angle microscopy (BAM) and infrared reflection-absorption spectrometry (IRRAS), as well as the instrumentation setup used for experiments discussed in this study. Chapter 3 reports on the preferential binding of various metal cations to a phosphate headgroup over –COOH, –OH, and $–N(CH_3)_2$ headgroups with application to enrichment at the ocean surface. Chapter 4 discusses the relative binding affinities of common ocean cations Na^+, K^+, Ca^{2+}, and Mg^{2+} to DPPA under the influence of pH. It was qualitatively observed that the binding affinity to DPPA was ordered $Ca^{2+} > Mg^{2+} > Na^+ > K^+$. The phosphate protonation state was found to be altered such that it remained partially protonated at higher pHs when it was actually expected to be fully deprotonated. Chapter 5 investigates the pK_{a2} of DPPA in further detail, employing titration and spectroscopy techniques to elucidate the precise pK_{a2} where DPPA become predominantly fully deprotonated. The pK_{a2} was found to be shifted to higher values up to 3 pH units, but was also influenced by both monolayer coverage density as well as presence of cations. Chapter 6 returns to the issue of selective preference of metal cations binding to phosphate headgroups. Metal binding affinity constants to the phosphate headgroup of DPPA were quantitatively determined and their underlying physical binding mechanisms investigated. The binding affinities of metal cations to DPPA was found to be in the order $Al^{3+} > Fe^{3+}$ ~>~ $Zn^{2+} > Mg^{2+} > Ni^{2+} > Mn^{2+} > Ca^{2+}$, with Fe^{3+} being variable due to its complex dependence on speciation and pH. Finally, Chapter 9 discusses the conclusions and implications of this research on atmospheric and biological interfaces.

1.3 Collaborations

Assistance in understanding DPPA spectra and peak assignments through theoretical computational work were performed by Shelby L. Brantly and Dr. Steven A. Corcelli in the department of Chemistry and Biochemistry at the University of Notre Dame. Harmonic vibrational frequencies for truncated models of the DPPA molecule in two different protonation states were computed with density functional theory (DFT) as implemented in Gaussian 09.[44] The DFT calculations utilized the B3LYP[45-47] functional and the 6-311++G(d, p) basis set. The optimized geometries of the truncated DPPA molecules in protonation states that correspond to low and high pH conditions, where the phosphate headgroup is singly deprotonated ($-\mathrm{PO_2}^-$) and fully ($-\mathrm{PO}_3^{2-}$) deprotonated. The truncated models of DPPA were deemed satisfactory because vibrational frequencies involving the phosphate headgroup were found to converge with respect to the chain length in preliminary calculations performed with a more modest basis set (data not shown).

Chapter 2. Theory & Instrumentation

2.1 Theoretical Overview and Background

2.1.1 Surface Tensiometry

Fundamental thermodynamic principles of surface tension have been extensively discussed elsewhere, hence only a cursory review will be given.[48-49] In summary, surface tension is the work required to increase the area of a surface. Thus by definition the units of surface tension are Joules/m^2, however surface tension is commonly reported in units of mN/m, or less commonly, dynes/cm. For neat water, the surface tension at 20°C is 72.8 mN/m. This high value is due to the nature of an interface: in the bulk region of water, the intermolecular hydrogen bonding forces are isotropic or equal in all directions. However at an air-aqueous interface, the forces are different between the liquid phase and the gas phase above the liquid; thus there is an excess downwards force into the bulk. The high surface tension of water reflects the strong preference of interfacial water to go into the bulk and minimize surface area, reducing the excess energy at the interface. For Langmuir monolayers, surface tension is often discussed as surface pressure (Π) where

$$\boldsymbol{\Pi = \gamma_o - \gamma_m} \tag{2.1}$$

which is defined by the surface tension of neat water (γ_o) minus the surface tension of the monolayer (γ_m). Thus a surface pressure of 0 mN/m is equivalent to a surface tension of 72.8 mN/m at 25°C.

Surface tension studies of a Langmuir monolayer employing a Langmuir trough are reported as surface pressure-mean molecular area (Π-A) isotherms. Monolayers lie along a plane at the aqueous-water interface and exhibit quasi 2-D phases that are analogous to 3-D liquid, solid and gas phases. When the surface pressure of the monolayer is 0 mN/m, the monolayer is in the gaseous phase (G). When an increase in surface pressure is observed, the monolayer transitions into a liquid phase (L). Based on the slope of the isotherm and type of intermolecular interactions, further liquid phase subcategories exist. When long range interactions are present and the monolayer molecules are weakly interacting, as exhibited by a shallow isotherm slope, the monolayer is in the liquid-expanded phase (LE). As the molecules draw closer and surface pressure and slope of the isotherm increases, stronger short range interactions also occur resulting in transition into a liquid-condensed phase (LC). A horizontal slope in the isotherm represents a coexistence phase between LE and LC where both phases are present simultaneously. The LC phase can be further divided into two subcategories based on the tilt of acyl chains; the lower slope tilted-condensed phase (TC) and the higher slope untilted-condensed phase (UC). Upon further compression, the monolayer exhibits its maximum surface pressure which is defined as the solid phase. If compressed even further, the monolayer is disrupted, breaking up into 3-D structures, which is the collapsed phase.

2.1.2 Brewster Angle Microscopy (BAM)

Brewster Angle Microscopy is a technique used to image the surface of insoluble Langmuir films at the air-aqueous interface. Fundamental principles of BAM have been extensively discussed elsewhere, hence only a brief review will be given here.[50-52]

BAM takes advantage of the phenomena that *p*-polarized light is perfectly transmitted, and not reflected at the Brewster angle when it passes from a lower refractive index medium to a higher refractive index medium. *p*-polarized light and its partner *s*-polarized light refer to light in which the electric field oscillates either parallel or perpendicular, respectively, to the plane of incidence. The reflectances R for *p*-polarized and *s*-polarized light are given by the Fresnel equations r̃

$$R_p = |\tilde{r}_p|^2 = \left(-\frac{\tan(\theta_i - \theta_t)}{\tan(\theta_i + \theta_t)}\right)^2 \tag{2.2}$$

$$R_s = |\tilde{r}_s|^2 = \left(-\frac{\sin(\theta_i - \theta_t)}{\sin(\theta_i + \theta_t)}\right)^2 \tag{2.3}$$

Where r̃ are the complex reflection coefficients and θ_i and θ_t are the incident and refracted angles. For *p*-polarized light, reflectance R_p is 0 when $\theta_i + \theta_r$ = 90°. For light passing between two different isotropic medium, the incident and refracted light angles are related by Snell's law

$$n_i \sin\theta_i = n_t \sin\theta_t \tag{2.4}$$

where n_i and n_t are the refractive indices of the incident medium and refracting medium respectively. At the Brewster condition, where R_p is 0 and $\theta_i + \theta_t$ = 90°, Snell's law can be rearranged as

$$n_i \sin\theta_i = n_t \sin(90 - \theta_i) \tag{2.5}$$

Which can be further simplified to

$$\tan\theta_i = \frac{n_t}{n_i} \tag{2.6}$$

Thus the Brewster angle is given by the simplified equation

$$\theta_i = \tan^{-1}\left(\frac{n_t}{n_i}\right) \tag{2.7}$$

At the Brewster angle, the refracted and reflected light are 90° apart. As the electric field vector is transverse to the direction of propagation, the dipole moment induced by the electric field of the refracted light is parallel to the direction of propagation of the reflected light. However, since the dipoles cannot oscillate and propagate in the same direction, propagation of the reflected light is impossible.

For an air-water interface, when a *p*-polarized light source and detector are positioned at the Brewster angle (~53.1°), no reflection is observed. However when a Langmuir monolayer is present, the refractive index is altered; thus the Brewster angle is also altered. Reflection of *p*-polarized light is once again possible. This change in reflection allows light contrast of water and monolayer. BAM images of water-rich regions will appear dark, while monolayer-rich regions will appear bright.

2.1.2 Infrared Reflection-Absorption Spectroscopy (IRRAS)

IRRAS is a surface sensitive variant of infrared (IR) spectroscopy. By reflecting an IR beam off an aqueous surface, the IR spectra of the surface species can be collected. This provides information such as packing orientation, degree of headgroup dissociation and binding/interaction with ions and other organics.[53-57] IRRAS spectra are reported as reflectance–absorbance (RA) spectra, where RA is defined as

$$RA = -\log\left(\frac{R}{R_0}\right) \tag{2.8}$$

where R_0 and R are the reflectances of the bare and monolayer-covered aqueous surfaces, respectively.

For a thin anisotropic film like a monolayer, the reflection coefficients of *p*-polarized and *s*-polarized light for IRRAS are modified from the Fresnel equations and are given

$$r_s = -\frac{\sin(\theta_i - \theta_t) - \frac{i2\pi}{\lambda n_t}\sin\theta_i\, I_i}{\sin(\theta_i + \theta_t) - \frac{i2\pi}{\lambda n_t}\sin\theta_i\, I_i} \tag{2.9}$$

$$r_p = \frac{\sin(\theta_i - \theta_t)\cos(\theta_i + \theta_t) - \frac{i2\pi}{\lambda n_t}\sin\theta_i\,(I_i\cos\theta_i\cos\theta_t - I_t\sin\theta_i\sin\theta_t)}{\sin(\theta_i + \theta_t)\cos(\theta_i - \theta_t) - \frac{i2\pi}{\lambda n_t}\sin\theta_i\,(I_i\cos\theta_i\cos\theta_t + I_t\sin\theta_i\sin\theta_t)} \tag{2.10}$$

where

$$I_i = ({n_{mx}}^2 - {n_t}^2)h \tag{2.11}$$

and

$$I_t = \frac{({n_{mz}}^2 - {n_t}^2)}{{n_{mz}}^2}h \tag{2.12}$$

where n_{mx} and n_{mz} refer to the complex refractive indices of the anisotropic monolayer perpendicular and parallel to the surface normal, and h the monolayer thickness.[58]

Based on the Fresnel equations, IRRAS absorption bands can be positive or negative depending on the angle of the incident beam.[52, 58] In the case of *s*-polarized light, IRRAS bands are negative at all practical angles (up to ~70°). For *p*-polarized light, IRRAS bands are negative below the Brewster angle and positive above the Brewster angle. For unpolarized light, the bands will shift from negative to positive slightly above the Brewster angle due to the joint contribution of *s*- and *p*-polarized bands. IRRAS peak intensities are also angle-dependent. In the case of a lipid monolayer, the peak intensities are maximized around ~57° and ~47° due to the sigmoidal nature of *p*-polarized angle intensities. A more in-depth explanation and analysis of IRRAS angular dependence can be found in Ref 58. In addition to angular dependencies, IRRAS peak intensities are also affected by experimental parameters including ambient water vapor backgrounds, IR beam energies and optics placement. Further in depth discussion on IRRAS optimization is presented in Appendix C.

2.2 Instrumentation

2.2.1 Compression Isotherm Setup

Surface pressure-molecular area (Π–*A*) compression isotherms of DPPA monolayers on neat water and salt solutions were obtained using a computer-controlled Langmuir trough (KSV Minitrough, Biolin Scientific, Finland). The trough is made of Teflon and has dimensions of 168 mm × 85 mm. The monolayer is symmetrically compressed using two Delrin-coated barriers. Surface pressure was measured during compression by the Wilhelmy plate method. Filter paper (Ashless grade, Whatman) was used as Wilhelmy plates. Prior to each experiment, the presence of extraneous surface-active contaminants was checked by sweeping the surface of the aqueous solution with the barriers until no significant change in the surface pressure (<0.1 mN/m) was observed. A measured amount of DPPA was spread dropwise onto the aqueous surface using a glass microsyringe (1725RN, Hamilton, Reno, NV). After spreading, solvent evaporation was allowed for approximately 10 min. The barriers were compressed at a rate of 5 mm/min/barrier. All experiments were performed at room temperature (21 ± 1.5 °C) and atmospheric pressure and humidity. Isotherms were repeated in sets of triplicates, with a maximum allowed error of ±0.25 $Å^2$. A maximum difference of ±0.5 $Å^2$ exists between sets due to small daily fluctuations in temperature.

2.2.2 BAM Setup

BAM images were collected simultaneously with the compression isotherms on a custom-built BAM setup.[59-60] A picture of the setup is shown in Fig. 2.1. The laser source (Research Electro-Optics, Boulder, CO) emits 5 mW *p*-polarized light at 543 nm. The output laser beam is first attenuated by a half-wave plate (Ekspla, Lithuania) then filtered by a Glan polarizer (Ekspla, diameter 14 mm) before reaching the aqueous surface at the Brewster angle (53.1° on water; this value was slightly adjusted for the various salt solutions). The reflected beam is collected by a 10× infinity-corrected super-long working distance objective lens (CFI60 TU Plan EPI, Nikon Instruments, Melville, NY; NA 0.21) and collimated by a tube lens (MXA22018, Nikon Instruments; focal length 200 mm) onto a back-illuminated EM-CCD camera (iXon DV887-BV, Andor Technology USA, Concord, MA; 512 × 512 active pixels with 16 μm × 16 μm pixel size). Because the inclined position of the imaging optics results in only a narrow region of the image being well focused, final images were cropped down from their full size (800 μm × 800 μm) to show the most resolved region. The lateral resolution of the BAM images was ~1.3 μm. In the BAM images shown here, a blue color scale was chosen to enhance imaging contrast. Light and dark blue areas correspond to regions with high and low lipid coverage, respectively.

2.2.3 IRRAS Setup

IRRAS spectra were collected using a customized setup built in the chamber of a FTIR spectrometer (Spectrum 100, Perkin Elmer, Waltham, MA). The setup consists of a breadboard upon which sits a Langmuir trough (KSV Minitrough, Biolin Scientific, Finland) and two planar gold mirrors (2 inch diameter) held above a trough or petri dish surface. The input and output mirrors were mounted on a horizontal sliding bar facing directly down onto the trough and their angles adjusted with rotation mounts. The input mirror was positioned at an incident angle of 46° (relative to the surface normal), chosen to maximize signal intensity. The incident IR beam is reflected off the input gold mirror onto the aqueous surface, and then reflected back up towards the output gold mirror, before being redirected towards a HgCdTe (MCT) detector. All spectra were obtained as a single beam measurement, with spectra taken on the bare aqueous surface used as the background spectrum. Spectra covered a range from 800 to 3000 cm^{-1} and were averaged over 5 min with a resolution of 4 cm^{-1}. Measurements were repeated at least three times to ensure reproducibility. Post-processing of spectra was performed in OriginPro 9.0, where the baseline was corrected by fitting a fourth-order polynomial in the region of interest. Final spectra shown are an average of at least three baseline-corrected spectra.

2.2.4 Surface Tension pH Titration Setup

For pH titration experiments, the tip of a buret containing 7 mL of 0.1 M HCl was immersed just below the surface of a 70 mL, pH 13 solution contained in a large (10 cm diameter) glass Petri dish. The solution was slowly stirred with a magnetic stir bar. A DPPA monolayer was then spread on the aqueous surface at a specific MMA and then titrated. A platinum Wilhelmy plate was used to measure the surface tension change over the course of the titration, while the pH was monitored (Accumet Basic AB 15 pH Meter, Fisher Scientific). Titrations were also repeated in triplicate. Surface-pK_a values were determined by fitting the experimental data with sigmoidal dose response curves in OriginPro 9.0 (OriginLab, Northampton, MA), with an estimated error of ±0.2. Experiments were performed at ambient temperature (21.0 ± 1.5 °C) and pressure.

2.2.5 Surface Tension Salt Titration Setup

For salt titration experiments, a Teflon petri dish (2.5 inch diameter, 1 inch height) with a septum opening on the side was custom built. 40 mL of solution was stirred in the petri dish with a magnetic stir bar. A DPPA monolayer was spread dropwise on a pH 3 aqueous surface at a specific condensed phase MMA, allowed 10 minutes to evaporate, and the surface tension measured by a platinum Wilhelmy plate. The concentrations of lipid spread were determined by the mean molecular area in the middle of the condensed phase, inferred from surface pressure-molecular area isotherm data. This corresponded to a mean molecular area (MMA) of ~45 Å^2 and surface pressure of ~15 mN/m for DPPA, DAG, and DAP, and ~21 Å^2 and ~18 mN/m for SA. Salt solutions were titrated by syringe injection from the side septum opening, and allowed 15 seconds of stirring, followed by 15 seconds of equilibration time before surface tension measurements. The surface tension of DPPA continues to decrease slightly and will not truly equilibrate even after several hours due to monolayer relaxation. However, this decrease is slow but linear. Previous experiments with DPPA have tested longer equilibration times up to several minutes, the data sets end up being parallel to each other. Thus we chose 15 seconds as a shorter time but keep it consistent throughout for all measurements. After each measurement, 30 seconds elapsed before the next syringe injection. (Measurements were taken with a minute between injections.)

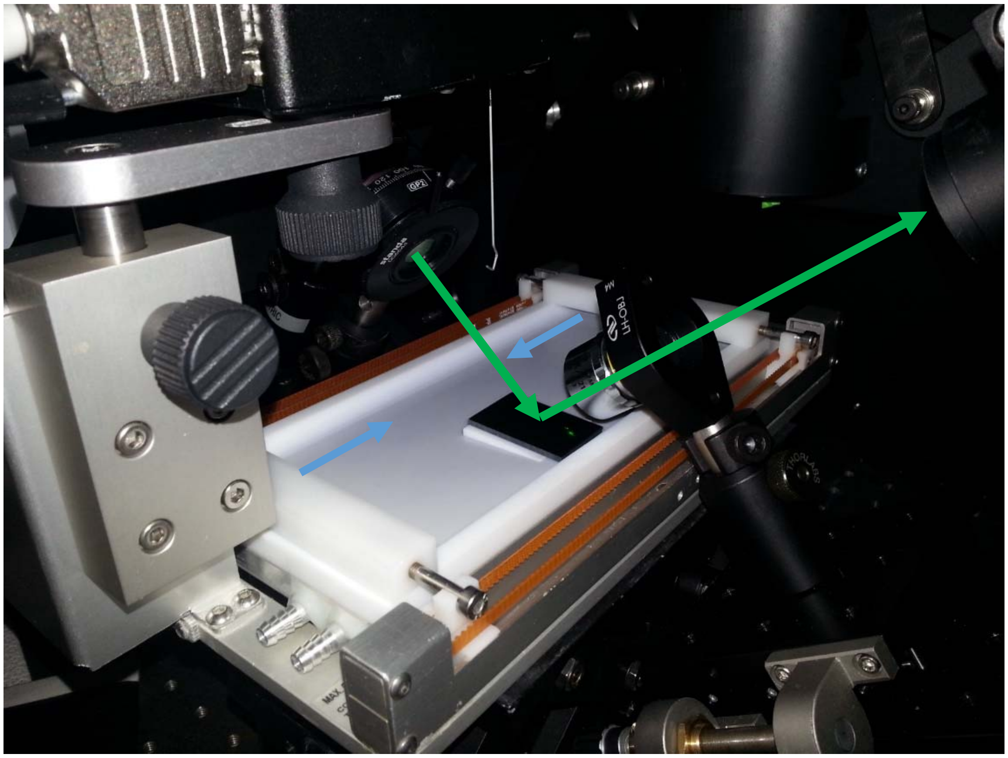

Figure 2.1 Langmuir Trough inside BAM setup.

Green arrow represent direction of BAM laser, blue arrows represent direction of trough barrier compression.

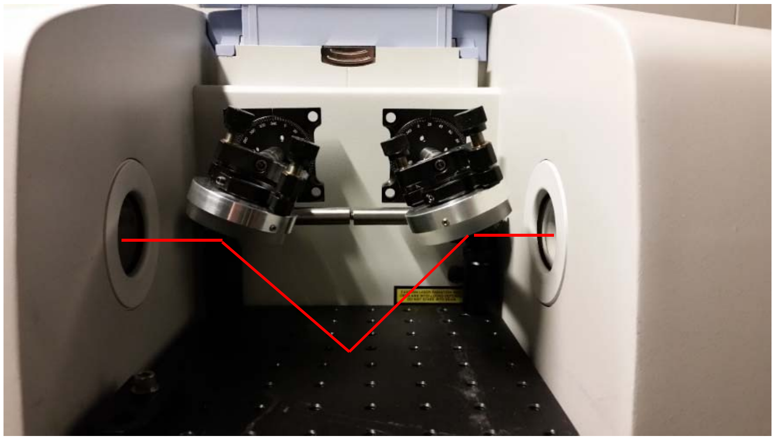

Figure 2.2 IRRAS Setup inside chamber of FTIR Spectrometer..
Red lines represent direction of IR beam.

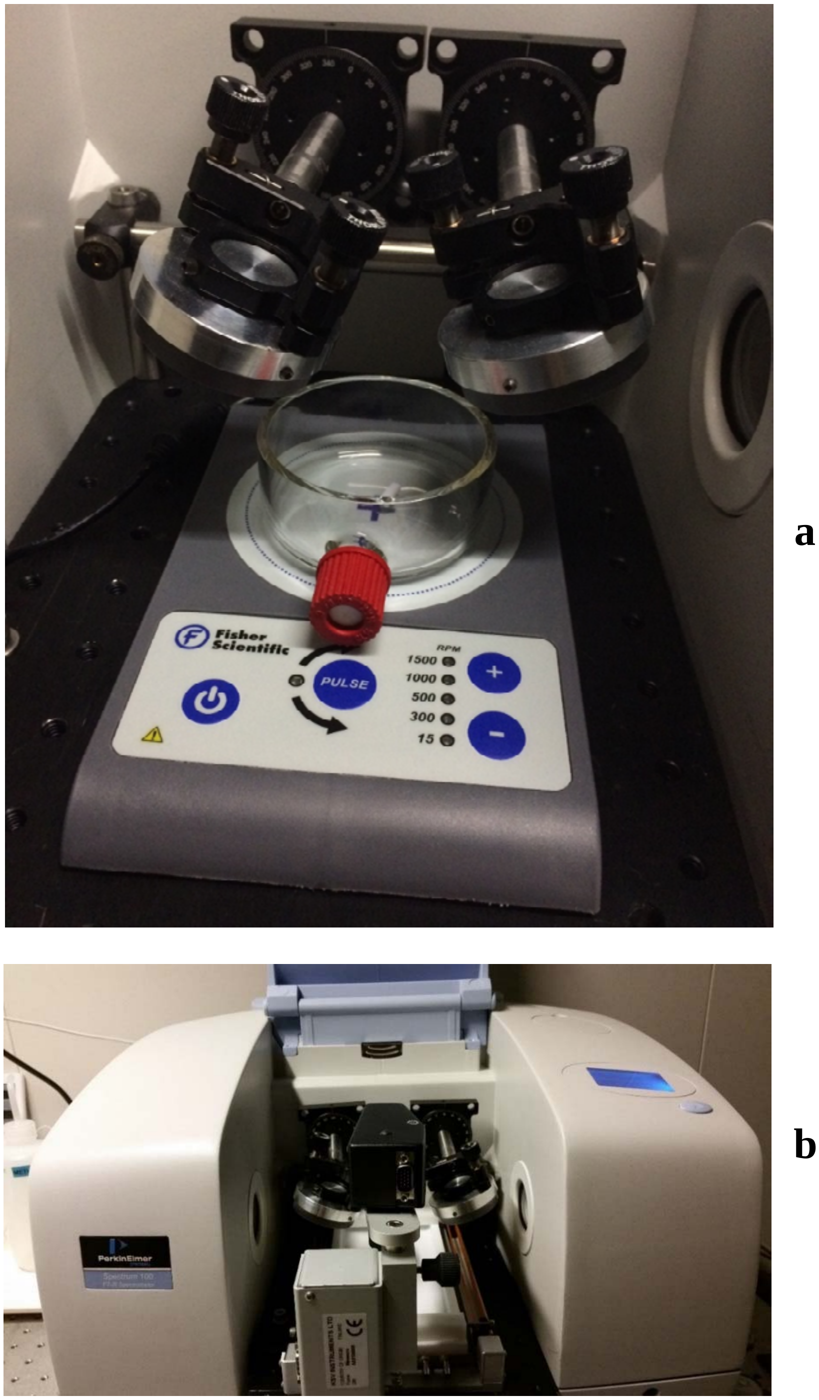

Figure 2.3 (a) Petri dish and (b) Langmuir trough with IRRAS setup.

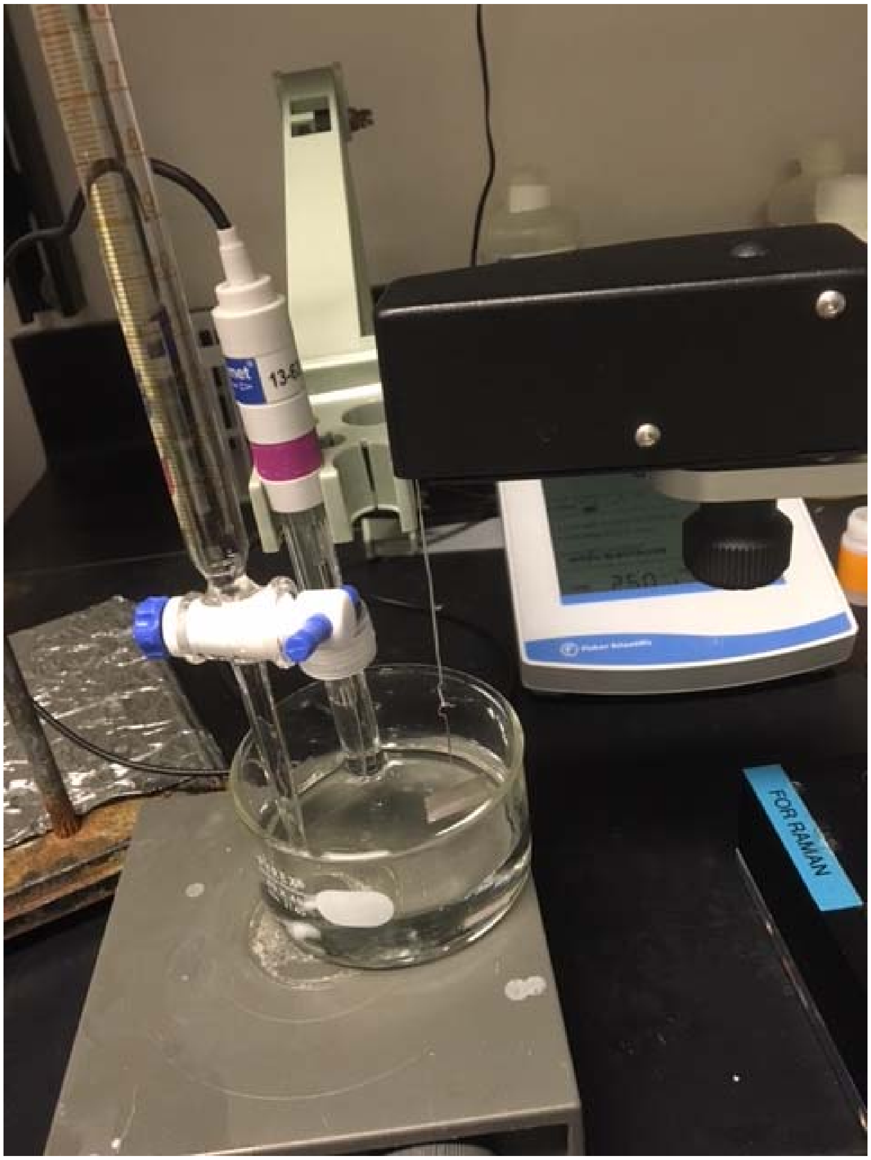

Figure 2.4 Surface tension pH titration setup.

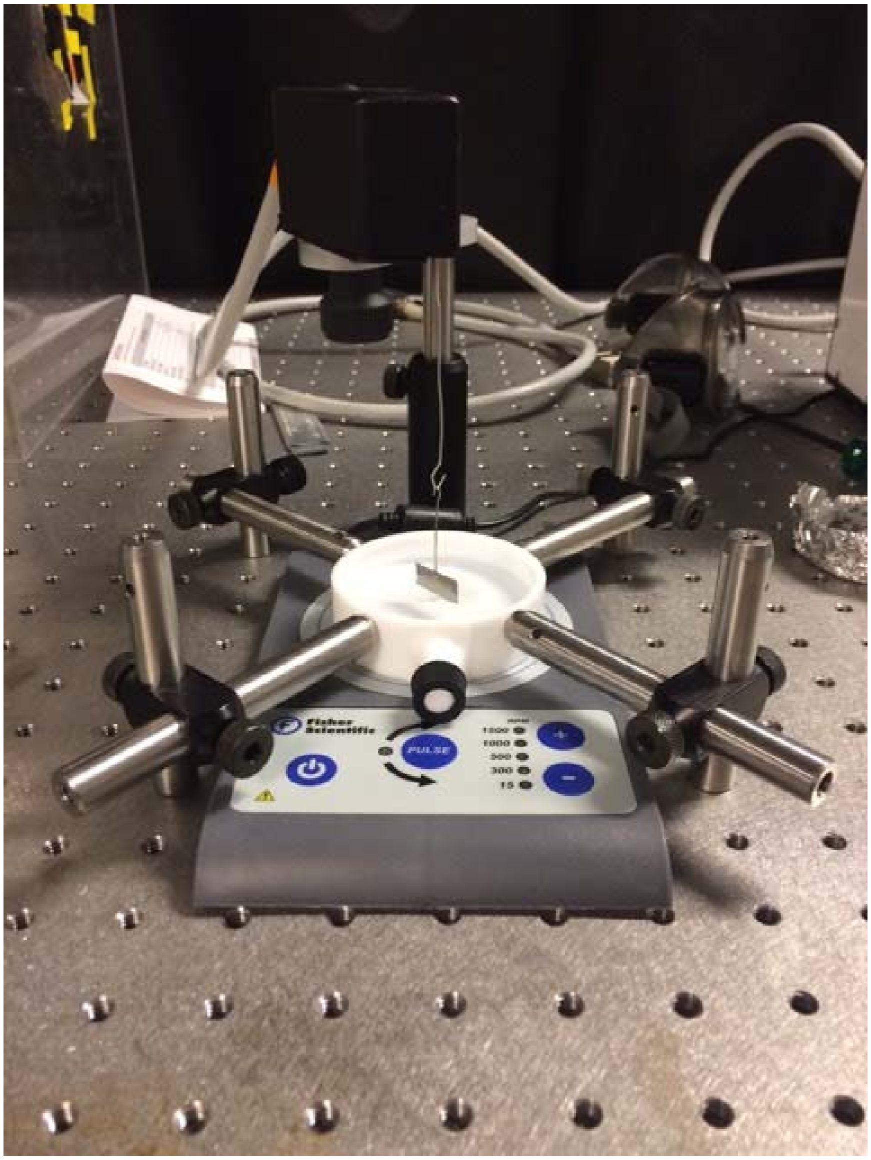

Figure 2.5 Surface tension salt titration setup.
Metal bars are for stabilization of petri dish while titrating in salts through septum.

Chapter 3. Trace Metal Binding to Surface Functional Groups

Reproduced in part with permission from Zhang, T; Fiamingo, M.E.; Allen, H.C. "Trace Metal Enrichment driven by Phosphate Functional Group Binding Selectivity" *JGR Oceans*, **2018**. Copyright American Geophysical Union.

3.1 Introduction

Studies have found a wide range of trace metal ions including Cd, Cr, Cu, Fe, Mn, Ni, Sr, and Zn to be enriched in both SSML and SSA, at higher relative enrichment factors than alkali and alkaline earth metal ions, although the latter still dominate in absolute concentration by several orders of magnitude.[9, 61-65] The enrichment of these trace metals is closely tied to biological activity, from microorganisms such as phytoplankton, bacteria, and viruses. These marine microorganisms not only release surface active organic molecules during biological activity but also when they breakdown and lyse, compounds such as transparent exopolymers, polysaccharides, fatty acids, sterols, alkanes and others.[43, 66-71] By binding trace metal ions, these surface organics enable surface metal enrichment, and ultimately, uptake into SSA. Although field studies have measured biological activity and metal enrichment of ocean surface waters, they are complicated by the geographical and temporal variation in the organic composition of SSML. Thus there has been less cohesive work on the physical underpinnings of trace metal binding to these organic compounds.[72-74] For example, formation constants for some trace metals with phosphate and carboxylate ligands are not well documented in the literature. In other cases, the literature focuses on inorganic complexation, thus there is a knowledge gap for delineating metal binding to SSML relevant lipids.

In this study, the interactions of several ocean surface enriched metals (Ca, Mg, Mn, Ni, Zn, Al, Fe) with organic surfactants are investigated using surface tension salt titration (STST). To understand how these ions selectively interact with different classes of organic compounds, we selected several very similar model lipids but with varying headgroups to represent these classes, and stearic acid to test the carboxylate headgroup (Fig. 3.1). A pH of 3 was used for all aqueous solutions to remove the variable of headgroup charge and to reduce ion precipitation effects for inter comparison purposes. By observing the impact of ions on the surface behavior of these surfactants, we seek to further understand the underpinnings of organic dependent trace metal enrichment in SSML and SSA.

3.2 Materials

1,2-Dipalmitoyl-sn-glycero-3-phosphate (DPPA) monosodium salt (>99%), 1,2-dipalmitoyl-sn-glycerol (DAG, >99%) , and stearic acid (SA, >99%) were purchased from Sigma-Aldrich (St. Louis, MO) and dissolved in 4:1 (v/v) chloroform-methanol (HPLC grade, Fisher Scientific, Waltham, MA) mixture. 1,2-dipalmitoyl-3-dimethylammonium-propane (DAP, >99%) was purchased from Avanti Polar Lipids (Alabaster, AL) and dissolved in chloroform. $CaCl_2$, $MgCl_2$, $MnCl_2$, $NiCl_2$, $ZnCl_2$, $AlCl_3$, and $FeCl_3$, salts were also purchased from Fisher Scientific (>99%). Aqueous solutions of pH 3 and 5.6 were obtained by addition of HCl (trace metal grade, Fisher Scientific, Accumet Basic AB 15 pH Meter, Fisher Scientific). All pH and salt solutions used ultrapure water with a resistivity of 18.2 MΩ·cm (Milli-Q® Advantage A10, MilliporeSigma, Burlington, MA). The salt solutions were prepared at pH 3, thus injection of pH 3 salt solution into pH 3 subphase rules out the change in pH due to salts themselves.

3.3 Results & Discussion

There are many different organic molecules with varying functional groups present in the SSML such as saccharides, phospholipids, and fatty acids. All of these organics present binding sites for metal cations, and can contribute to the selectivity of SSML cation enrichment. To investigate the differences in metal cation binding between phosphate ester and other functional groups, we selected the following lipids: 1,2-dipalmitoyl-sn-glycero-3-phosphate (DPPA), 1,2- dipalmitoyl-sn-glycerol (DAG), 1,2-dipalmitoyl-3-dimethylammonium-propane (DAP) and stearic acid (Fig 3.1).

DPPA has been well documented in our previous works as an ocean relevant organic surfactant with high surface activity and a simple phosphate headgroup.[18, 75] Here it remains our representative phosphate lipid model. In this study, it remains our representative phosphoric acid lipid model. To investigate metal cation interactions with saccharide OH groups, 1,2-dipalmitoyl-sn-glycerol (DAG) was chosen as it is a molecule similar to DPPA, but lacking the phosphate, leaving only the exposed OHs of the glycerol backbone. 1,2-dipalmitoyl-3-dimethylammonium-propane (DAP) was chosen as it is similar to a common phospholipid DPPC with a choline-like headgroup, but without a phosphate ester group DPPA, DAG, and DAP all possess two C16 alkyl chains, although their respective headgroups differ, allowing for strict comparison between cation binding. Stearic acid was chosen to model the carboxylic acid headgroup. While the dipalmitoyl lipids are firmly constrained to the interface due to their dual C_{16} alkyl tails, single tail fatty acids are more soluble, thus the C_{18} stearic acid was selected over C_{16} palmitic acid for its relative insolubility.

To compare the relative binding affinity of various cations to surfactant headgroups, the change in surface tension of the surfactant was monitored as salt solution was titrated in. As the metal cations bind to the surfactants, they alter the surface organization and the surface tension is expected to change. A larger change in the surface tension represents increased binding and higher binding affinity. Surface tension values in titration experiments were also background subtracted to account for the contribution of increased buoyancy to surface tension from the additional titrant volume, as well as the contribution of surface tension change due to relaxation of the monolayer over time, and are plotted as change in surface tension instead of absolute surface tension. Salts themselves also alter the surface tension of water, but this was minimal due to the low concentrations involved, so there was no need to background subtract the salt contribution to surface tension.[76]

Fig. 3.2 shows the STST measurements of a DPPA monolayer spread to the condensed phase MMA of 45 $Å^2$ (~15 mN/m surface pressure) on various salts at pH 3. All salts are observed to decrease the surface tension with the exception of zinc. While surprising, this behavior is consistent with surface pressure-area isotherm data discussed in Chapter 6. In addition, formation of white insoluble $Zn(OH)_2$ precipitate was observed beyond 0.03M, limiting measurements at higher concentrations.

Figs. 3 & 4 show the STST measurements of DAG and DAP with various salts also at pH 3 in their condensed phase (also ~15 mN/m for both). An observed increase in surface tension from the addition of Al^{3+} by 2 mN/m occurs for DAG compared to the larger 10mN/m change for DPPA. The other salts do not change the surface tension significantly (< 0.5 mN/m), leading to the conclusion that the interaction of the hydroxy headgroup on DAG with the aqueous salt solutions was weak or nonexistent. The sole sensitivity of Al^{3+} to OH is attributed to its speciation: at pH 3, Al^{3+} favors formation of polynuclear species, with oligomeric $Al_3(OH)_4{}^{5+}$ the dominant species. It is likely that the OH group of Al-OH ligands are able to exchange with one of the DAG OH moieties resulting in binding of Al^{3+} to DAG. However, this binding process occurs only at the highest observed concentration, portraying a much weaker binding interaction between the functional group of DAG and Al^{3+}.

DAP observed slightly larger changes in surface tension for each of the salt solutions, indicating a stronger binding activity compared to DAG, but still not as prominent than that of DPPA. Al^{3+} shows a slight increase in surface tension as well, ~1 mN/m, while Mg^{2+}, Mn^{2+} and Ni^{2+} show a slight decrease in surface tension of ~1 mN/m indicating weaker binding interactions are present. Although these changes in surface tension point to cation-headgroup interactions, their magnitudes are on an order of ~1mN/m with large uncertainties, thus it cannot be concluded whether or not there was a significant change in surface tension. While there is likely some interaction between lone pair of electrons on the nitrogen atom and metal cations, they are still quite weak compared to the phosphate ester interactions.

Fig. 3.5 shows the salt titration of stearic acid with different salts in the condensed phase (~18 mN/m). For Ca^{2+}, Mg^{2+}, Mn^{2+} and Ni^{2+}, the changes are also ~1mN/m, indicating weaker binding affinity compared to the phosphate (DPPA). However it is well known that Ca^{2+} and Mg^{2+} bind to the carboxylic acid headgroups of fatty acids, and previous work on Π-A isotherms of Ca^{2+} and Mg^{2+} on palmitic acid have shown only small expansion changes to the monolayer, which is consistent with the small changes in surface tension we observe in the titration.[77] Stearic acid shows dramatic surface tension increases for Fe^{3+}, Zn^{2+}, and Al^{3+} of which Fe^{3+} and Zn^{2+} reach the surface tension of pure water (72 mN/m). These metals are known to form metal-stearate soap complexes that are insoluble or sparingly soluble, hydrophobic, and are commonly used in industry in oils and paints. In addition, metal stearates have been known to crystallize into aggregates which would precipitate out.[78] We can conclude that Fe^{3+} and Zn^{2+} deplete stearic acid from the surface indicated by the approach to the Δ surface tension value of the aqueous solution without lipid coverage, Al^{3+} however still exhibits some activity, reaching a surface tension 8 mN/m less than that of water. Aluminum stearate has been used for over a century and is a well-known defoamer in industry for reducing surface tension of water based fluids.[79] The surfactant behavior of aluminum stearate would result in the small reduction in the surface tension of water. Even though Fe^{3+}, Al^{3+}, and Zn^{2+} display strong binding to stearic acid, the resulting metal-soap complex inevitably removes them from the surface. This has important implications for SSML enrichment, as binding of fatty acids to Fe^{3+} trace metals would result in SSML depletion of both fatty acid and metal.

With this study, we shed light on selective metal cation enrichment within the SSML. We strongly assert that it will be closely tied to organic composition, which in turn is closely tied to marine biological processes. From the magnitudes of the surface tension change from metal cations on various organic monolayers at pH 3, the phosphate ester headgroup has the highest affinity for metal cations, followed by the moieties of COOH, and $N(CH_2)_2$. For Al^{3+}, Fe^{3+}, and Zn^{3+}, enrichment at the SSML is likely therefore driven by phosphate ester moieties rather than fatty acid COOH moieties as the latter depletes from the surface upon metal cation binding. We further postulate that phospholipids which comprise the majority of cell membranes could selectively surface enrich ions, but as lipids naturally degrade into fatty acids, they deplete from the immediate surface, resulting in a time dependent composition of SSML. This mechanism could contribute to the variations in trace metal enrichment factors in SSML. For the divalent metal cations, the phosphate ester headgroups bind strongly resulting in surface enrichment, in the order of $Mg^{2+} > Ni^{2+} > Mn^{2+} \sim Ca^{2+}$. Carboxylic acid and dimethylamine headgroups also contribute to the surface enrichment of cations, with Ca^{2+} favored over Mg^{2+} for fatty acids, yet still not as strongly as phosphate ester headgroups. It is somewhat surprising that the dimethylamine headgroup exhibited binding to cations, which suggests that ammonium and ammine containing compounds may also contribute to trace metal enrichment. The deprotonated phosphate ester headgroup (and phosphate anion) remains the stronger Lewis base, and has a higher metal cation affinity, and is likely the dominant source of metal cation enrichment within the SSML.

3.4 Conclusion

The enrichment of trace metals in the sea surface microlayer is primarily driven by surface active organics, and although field measurements have reported polyanion enrichment alongside trace metals, there is an insufficient physical understanding of the mechanism behind trace metal enrichment. DPPA, DAG, DAP, and stearic acid were experimentally compared as representatives of phosphate, hydroxide, dimethylammonium and carboxylic acid functional groups found in the diverse soup of molecules in the SSML. We find that although dimethylammonium and carboxylic acid groups exhibit binding and affinity to trace metals, metal ion binding is still dominated by the strength of the phosphate interaction with trace metals. Al^{3+}, Fe^{3+} and Zn^{2+} are depleted from the aqueous surface upon binding to fatty acids.

Ultimately it is the phosphate headgroup of DPPA that displays the greatest surface tension change upon cation binding while still retaining the metal ions at the surface. Thus we have identified phosphate as the most significant headgroup responsible for trace metal enrichment at the SSML; we will focus on the mechanisms of metal binding to DPPA in subsequent chapters. Interestingly, the phosphate anion is also enriched in surface waters, and is known to be a strong metal binder.[18, 80-81] However, other contributions to the trace metal enrichment such as binding to SSML organics containing sulfate and nitrate groups do exist. Further research into the binding affinities of trace metals to these functional groups is needed to more fully understand trace metal enrichment in SSML and SSA.

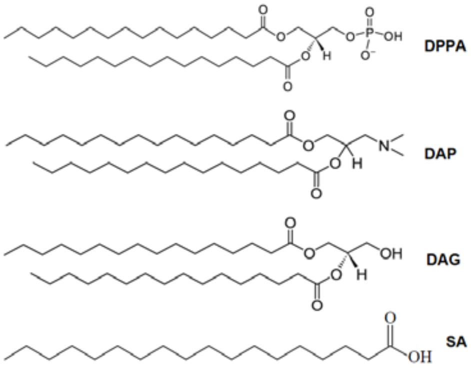

Figure 3.1 Structures of DPPA, DAP, DAG and SA.

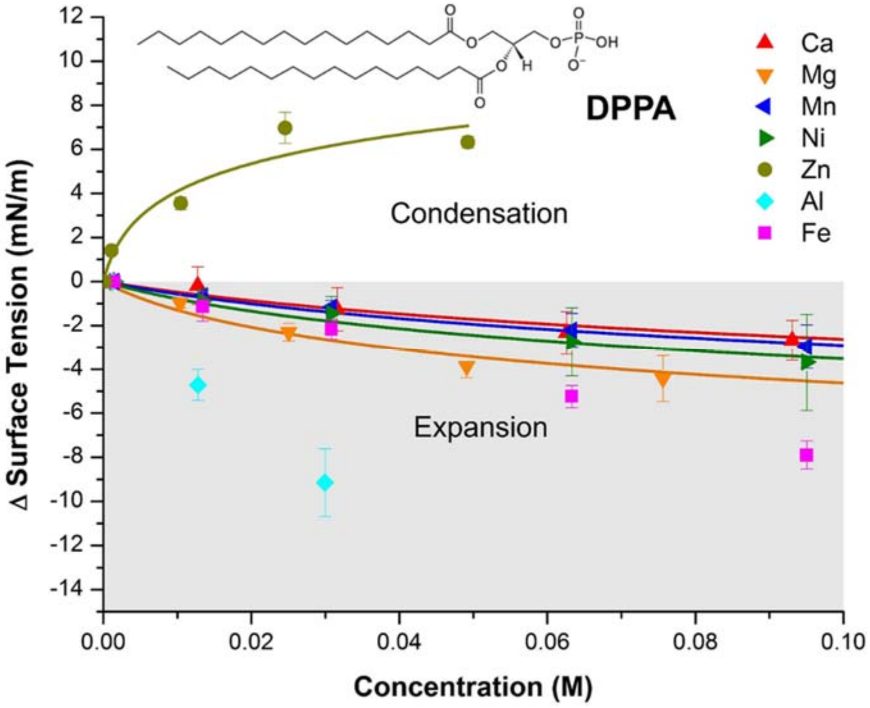

Figure 3.2 Surface tension changes of DPPA as a function of metal salt concentration on pH 3 solutions.

Solid lines are the Szyszkowski fit discussed in Chapter 6. White and gray areas correspond to condensation/expansion areas relative to on pure water in Π-A isotherms (Fig. 6). There is substantial surface tension change upon addition of trace metals.

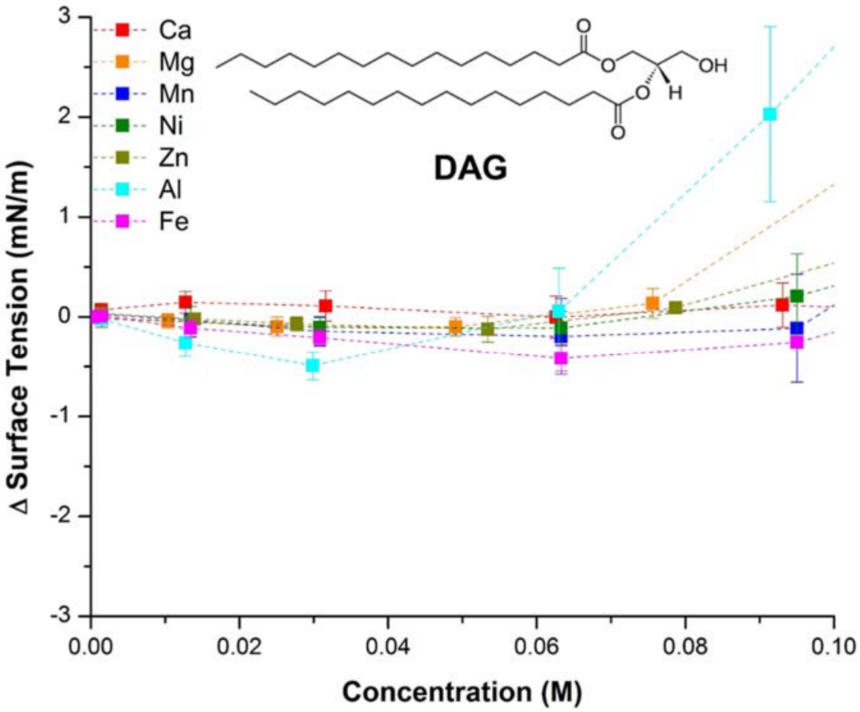

Figure 3.3 Surface tension changes of DAG as a function of metal concentration on pH 3 solutions. Dotted lines are for eye guide. There is no substantial surface tension change upon addition of trace metals compared to DPPA except for Al.

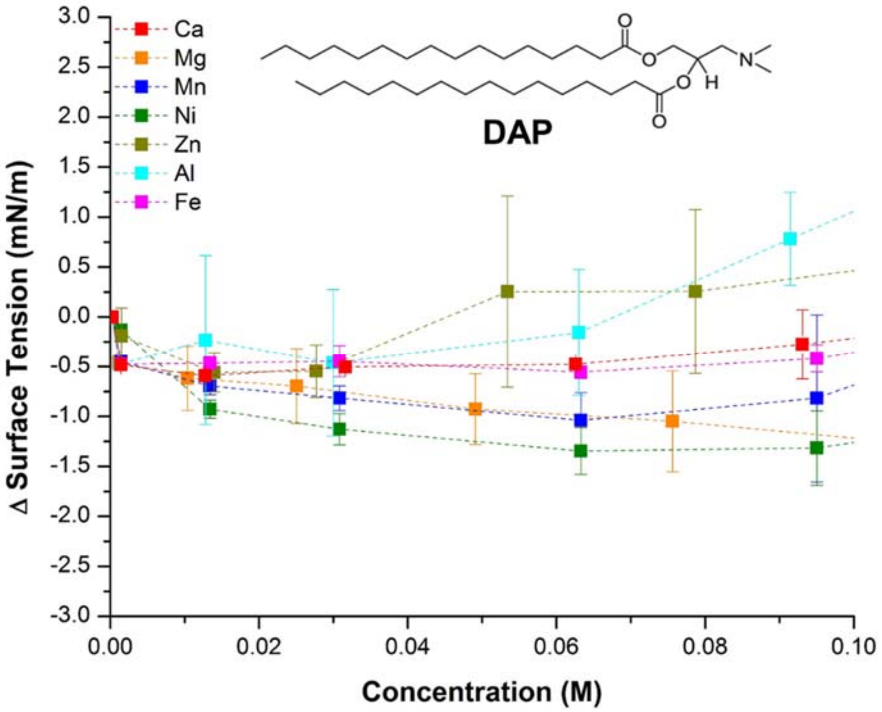

Figure 3.4 Surface tension changes of DAP as a function of metal concentration on pH 3 solutions. Dotted lines are for eye guide. There is no substantial surface tension change upon addition of trace metals compared to DPPA.

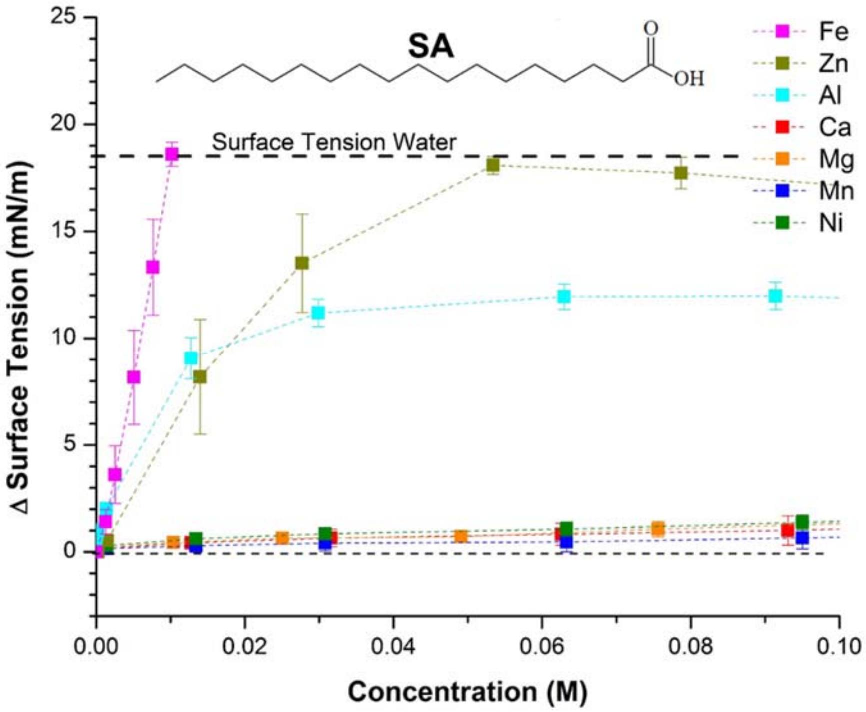

Figure 3.5 Surface tension changes of stearic acid as a function of metal concentration on pH 3 solutions. Dotted lines are for eye guide.
Horizontal dotted line represents a surface tension of 72 mN/m (~ that of pure water). There is no substantial surface tension change upon addition of most trace metals compared to DPPA. Binding to Fe, Zn, and Al results in a surface tension around that of pure water indicating depletion from the water surface.

Chapter 4. Effect of Common Ocean Cations on DPPA

Reproduced in part with permission from Zhang, T; Cathcart, M.G; Vidalis, A.S.; Allen, H.C. "Cation effects on phosphatidic acid monolayers at various pH conditions" *Chemistry and Physics of Lipids*, **2016**, 200, 24-31. Copyright Elsevier

4.1 Introduction

Phospholipids from the marine biota such as DPPA (Fig. 4.1) are important sources of saturated fatty acids found in the sea surface microlayer (SSML) and at the surface of marine aerosols.[38, 40-43] In particular, derivative saturated fatty acids with C_{16} (palmitic acid) and C_{18} (stearic acid) carbon alkyl chains are known to be the most abundant. These surface-active organic compounds ultimately form thin films that affect aerosol growth and volatility, radiative absorption and scattering, reactivity with atmospheric gases, and cloud condensation nuclei activity.[6, 22-27] In turn, the interfacial properties of these films are directly influenced by the pH and ionic composition of the aqueous phase.

In this work, we examine the effects of pH and marine-relevant cations (Na^+, K^+, Ca^{2+}, and Mg^{2+}) on DPPA's phase behavior, stability, and surface morphology using surface pressure-area isotherms and Brewster angle microscopy. Na^+, K^+, Ca^{2+}, and Mg^{2+} cations are the most abundant ions found in the ocean.[20] The investigation of these properties is particularly applicable to marine aerosol surfaces, where enrichment of specific cations may impact the surface morphology and organization of organic films.[13, 20]

4.2 Materials

4.2.1 Materials

1,2-Dipalmitoyl-*sn*-glycero-3-phosphate (DPPA) monosodium salt (>99%, lyophilized powder) was purchased from Avanti Polar Lipids (Alabaster, AL; M_w 670.873 g/mol). The average molecular weight (M_w) is 670.455 g/mol due to the variability in the Na^+ content. NaCl, KCl, $MgCl_2$, and $CaCl_2$ salts (>99%, ACS certified) were purchased from Fisher Scientific (Waltham, MA). Chloroform and methanol (HPLC grade) as well as trace metal grade HCl and NaOH were also from Fisher Scientific. Ultrapure water with a resistivity of 18.2 MΩ·cm and a measured pH of 5−6 (the water pH is slightly acidic due to dissolved atmospheric CO_2) was obtained from a Barnstead Nanopure filtration system (D4741, Thermolyne Corporation, Dubuque, IA) equipped with additional organic removing cartridges (D5026 Type I ORGANIC-free Cartridge Kit; Pretreat Feed).

4.2.2 Preparation of lipid and salt solutions

DPPA stock solutions were prepared by dissolution in a 7:3 (v/v) chloroform:methanol mixture. All aqueous salt solutions were prepared at 0.6 M by dissolution in pure water. Salts and salt solutions were pretreated according to previously reported procedures to minimize the impact of organic contamination [82]. NaCl and KCl salts were baked at 650 °C, whereas $MgCl_2$ and $CaCl_2$ solutions were filtered at least thrice using activated carbon filters (Whatman Carbon-Cap 75, Fisher Scientific) to remove organic contaminants. A separate set of carbon filters was used for each salt to avoid any ion cross-contamination. The concentration of these purified stock solutions was determined by Mohr's chloride titration method [83]. Each solution was prepared by serial dilutions of the purified stock solutions. The pH of the prepared solutions was adjusted by adding the required amounts of stock concentrated HCl and 10 M NaOH.

4.3 Results & Discussion

4.3.1 pH effects on DPPA monolayers

The Π–*A* compression isotherms of DPPA on pure water at different pHs are shown in Fig. 4.2. The region before lift-off as shown in the DPPA isotherm at pH 5.6 corresponds to the gaseous (G)-liquid-condensed (LC) coexistence phase of DPPA. Lift-off into a tilted-liquid condensed (TC) phase occurs at approximately 47.5 Å^2/molecule. (For isotherms at pH ≤ 10, the mean molecular area (MMA) at lift-off is determined by prolonging the tangent of the slope of the TC transition down to Π = 0 mN/m.) With a high phase transition temperature of 67 °C, DPPA does not exhibit a distinct liquid-expanded (LE) phase like DPPC, which indicates the presence of attractive van der Waals forces between the alkyl chains and hydrogen bonding between phosphate headgroups causing DPPA to exist in a highly ordered phase at room temperature.[84-87] DPPA has also been shown to form hexagonal packing suggestive of hydrogen bonding interactions.[31, 88-89] A transition from the TC phase to the untilted-LC (UC) phase is indicated by a kink in the isotherm at about 43.5 Å^2/molecule and 20 mN/m. At about 42 Å^2/molecule and 53 mN/m, the monolayer reaches collapse. The limiting area of the DPPA isotherm at pH 5.6 corresponds approximately to the area of two compact alkyl chains (2×20 Å^2) and is in relatively good agreement with values published in the literature, even though there is a notable variability depending on the experimental conditions (see Appendix A).

Depending on the pH but also on the lipid packing density, the phosphate moiety bears a charge that varies between 0 and -2*e*, where *e* is the elementary electronic charge. As pH increases, the DPPA monolayer progressively deprotonates and goes from neutral to increasingly negatively charged. However, a negatively charged monolayer attracts excess protons (H^+) to the lipid/aqueous interface similar to how a negatively charged surface attracts counter-ions for an electrical double-layer.[90] The concentration of protons at the surface ($[H^+]_s$) being higher than in the bulk causes the pH in the local environment of the phosphate group to be less than the bulk pH.[91] This decrease in surface pH can be quite significant depending on the lipid system and degree of ionization; for instance, it has been reported to be as much as 4 pH units lower for stearic acid monolayers.[90] Even a compression of the monolayer can result in a decrease of surface pH due to the higher charge density of the increasingly closely packed monolayer. Effectively, this means the surface pK_a of the monolayer is increased, and thus the bulk pH must then be higher to observe deprotonation. To examine the effect of the different DPPA species (charged and neutral), isotherms were obtained in a pH range (from 1.7 to 13.0) extending beyond the apparent surface pK_a values, which have been previously reported to be $pK_{a1,s} \approx 3.2\text{-}3.8$ and $pK_{a2,s} \approx 7.9\text{-}8.5$ in aqueous dispersions and monolayers.[92-93]

No significant changes in the monolayer MMA are observed below pH 10 (see inset of Fig. 4.2). This contradicts previous observations made by Miñones et al., that observed a small condensing effect upon lowering the pH from 6 to 3, but agrees with Luckham et al., who reported that DPPA isotherms at pH 1 and 5.6 are almost superimposable (Luckham et al., 1991).[94] This suggests that DPPA exists predominantly as a neutral (0) species at pH <~10. This is supported by a monolayer pH titration study by Patil et al. that observed a pK_a at only 8.7.[93] However, while a deprotonated phosphate headgroup has more repulsive electrostatic interactions than its neutral form, it also has more available attractive hydrogen(H)-bonding sites to bond with neighboring headgroups.[89] These two opposing effects could cancel each other, effectively leading to identical isotherms. As isotherms give a macroscopic picture and not molecular level information, differentiating the two species may not be possible. However, the appearance of further expanded isotherms at higher pHs indicate that there is significant electrostatic repulsion beyond the condensing effect of increased H-bonding, such that two species do not have identical isotherm behavior. The most likely explanation is that when both species exist, isotherms may not distinguish the two due to the hydrogen bonding, but when the (-1) species starts to dominate over the (0) species as the pH increases, electrostatic repulsion becomes stronger and monolayer expansion is observed.

At pH 10.3 there is a noticeable difference in the isotherm attributed to the emergence and dominance of singly deprotonated (-1) DPPA species. The lift-off area expands from 47.5 to 51.5 Å^2/molecule and the UC phase disappears (Fig. 4.2). The surface pressure as well as the collapse pressure increase due to the stronger electrostatic repulsion between singly protonated DPPA molecules. At pH 13, an even greater expansion is observed. Excess repulsion from the increased negative charges results in the immediate onset of a condensed phase, with disappearance of any unique phase behavior leading up to the first of two collapse phases. The first collapse onset begins around 53 mN/m just as seen in the isotherms at lower pH, while the second collapse starts around 64 mN/m. The presence of two collapse pressures is indicative of immiscibility of two different components.[95] This behavior can be explained by emergence of the (-2) species at pH 13. While the (-1) species experiences more repulsion than the (0) neutral species and is further expanded, both are still capable of hydrogen bonding and thus remain miscible and retain a common collapse pressure.[89] However, the (-2) species does not hydrogen bond well and is immiscible with the (0) and (-1) species, resulting in a unique collapse pressure. Therefore, the deprotonation of DPPA occurs at much higher pHs (10.3, 13) than expected from reported pK_a values (3.5, 8.3), an increase in pK_a of about 5-7. This phenomena of large pK_a shifts for charged monolayers has also been reported for other species such as fatty acids, and L-phenylalanine.[96-100]

4.3.2 Cation effects on DPPA monolayers

Fig. 4.3 shows compression isotherms of DPPA monolayers on a series of 0.6 M chloride salt solutions at pH 5.6. All salts are seen to expand the monolayer, inducing the onset of the condensed phases much earlier and at larger MMAs than pure water. Thus at any given fixed MMA, the salt isotherms reveal higher surface pressures, whereas at any given fixed surface pressure, they show larger MMAs. By inspection, the expansion of the DPPA monolayer is cation-specific and follows the order $Na^+ > K^+ \approx Mg^{2+} > Ca^{2+}$, with respective lift-off areas of 51.5, 50.5, 50.5, and 48.5 Å^2/molecule. This ordering appears to follow the trend of surface charge density. Due to the small and exposed phosphate headgroup of DPPA, many factors must be considered such as ion size, hydration, and surface charge density which all contribute to the ability of cations to complex with and disrupt the monolayer. The ionization state of the phosphate headgroup is also altered via pH to compare the relative binding affinities of each cation for DPPA.

4.3.2.1 Monovalent cation interactions with DPPA monolayers

A comparison of cation-headgroup interactions at the various ionization states of DPPA is first made between the monovalent cations. The effect of Cl^- co-ions can be neglected as studies have shown that chloride does not display an affinity for lipid headgroups.[101] Fig. 4.4 shows the Π–A isotherms of DPPA monolayers on 0.6 M NaCl and KCl solutions at pH 2.5, 5.6 and 10.1. One immediately observes unique isotherms for each pH, which greatly contrasts with those on pure water that are identical at pH 2.5 and 5.6. This is evidence of the presence of different DPPA species induced by the cation complexation. Thus, indicated here, in the presence of Na^+ and K^+, the DPPA monolayer is populated predominantly by neutral (0) species at pH 2.5, singly protonated (-1) species at pH 5.6, and fully deprotonated (-2) species at pH 10.2.

The isotherm of DPPA on NaCl at pH 2.5 shows only a minor expansion of the monolayer compared to that on neat water at pH 5.6. The lift-off area is increased by ~1 Å^2/molecule while the phase transition area and surface pressure remain the same. The isotherm of DPPA on KCl at nearly the same pH shows an even smaller expansion of ~0.5 Å^2/molecule. These very small area changes suggest that when the pH of the solution is low, H^+ inhibits cation-induced deprotonation. However, Na^+ and K^+ can still complex with the DPPA headgroup at very low pHs, albeit weakly. Although DPPA is predominantly neutral at pH 2.5, there could be a small fraction of the singly protonated (-1) species induced by cation complexation that contributes to the small expansion of the monolayer.

At pH 5.6, the isotherm of DPPA on salts show similar expansion behavior compared to that on water at pH 10.3, providing further evidence that DPPA is (-1) from cation-induced deprotonation. At pH 10.1, the isotherm on monovalent salts show more ordering of the condensed phase compared to that of water at pH 13.0, but are still similar as they share the same protonation state (-2) as well as disappearance of the TC-UC phase transition.

The speciation of DPPA with Na^+ and K^+ fits well with the apparent surface pK_a values reported in the literature. This can be explained by the fact that not only H^+ but also metal cations are attracted to negatively charged phosphate headgroups. The cations shield the phosphate charge as well as displacing H^+ at the surface, thus effectively decreasing the local $[H^+]_s$ concentration.[91, 102] This has an effect of restoring the surface pH to a value more closely resembling that of the bulk. This is also in line with the "electrostatic/hydrogen-bond switch mechanism" of phosphatidic acid in that the H-bonding and protonation state of DPPA are affected by local ions or charged groups and consistent with observations made by Vaknin and co-workers.[35, 91] Similar results were also reported from sum frequency vibrational spectroscopy studies for palmitic acid by Allen and co-workers showing that cations including Na^+ and K^+ deprotonate the carboxylic acid headgroup at pH 5.6 where the headgroup is normally protonated on pure water.[100, 103-105]

The relative binding affinity of Na^+ vs. K^+ is inferred from the differences in the compression isotherms for each ionization state. Na^+ and K^+ have the same charge and similar hydration radii (2.18 and 2.12 Å, respectively) and thus one might expect the monolayer to experience similar expansion.[106] However when comparing Na^+ and K^+, Na^+

is consistently further expanded by ~1 Å^2/molecule at all pHs (Fig. 4.5). This difference suggests K^+ interacts more weakly with the phosphate headgroup than Na^+ and, in turn, is unable to induce deprotonation as effectively. The collapse pressures of DPPA with Na^+ are also noticeably higher than that on water for the same protonation state, while the collapse pressures with K^+ by contrast display no increase. Na^+ complexation with the headgroup has a stabilizing effect on the monolayers allowing for higher surface pressures before collapse. This is also supported by nucleation structures observed in BAM images discussed later in this paper. Mixed equimolar solutions of Na^+ and K^+ also reveal isotherms identical to those of Na^+ (data not shown). This all indicates that Na^+ outcompetes K^+, forms a more stabile complex with DPPA, and thus has a higher binding affinity for the DPPA headgroup.

One possible explanation for the higher affinity of Na^+ over K^+ is found in the empirical law of "matching water affinities" proposed by Collins, which states that ions of similar sizes form inner-sphere ion pairs due to their similar absolute free energies of hydration.[107] Na^+ has a higher surface charge density than K^+ and is a better match with phosphate, allowing easier deprotonation and subsequent binding. MD simulations have also observed weaker binding of K^+ than Na^+ to the phosphate [101]; it is clear that Na^+ ions are attracted to the headgroup region.[31]

An alternative explanation involves interaction of Na^+ with the carbonyl groups of the DPPA alkyl chains. MD simulations have also shown a greater preference of Na^+ for the carbonyl moieties than K^+.[108-111] If Na^+ can penetrate into the headgroup region and interact with the carbonyl moiety of DPPA, steric effects may be responsible for the greater expansion of the DPPA monolayer compared to K^+. Indeed both salt isotherms converge at higher surface pressures, which is due to squeezing out of some ions from the DPPA monolayer. This does not preclude the absence of Na^+ complexation with the carbonyl groups, but it is very weak as Na^+ ions are eventually expelled from the headgroup region. This agrees with MD simulations that show little impact on lipid conformations in the condensed phase due to the low degrees of freedom.[112] However, All of the Na^+ ions are not squeezed out and a portion remain complexed with the headgroup as seen by its impact on the collapse pressure. This suggests that direct complexation with phosphate may be a factor.

4.3.2.2 Divalent cation interactions with DPPA monolayers

There is great interest in the effect of divalent cations for both biological and atmospheric studies and their increased binding affinity compared to monovalents.[113] Divalent cations inherently have higher binding affinities relative to H^+ and monovalent cations due to their higher surface charge densities. The effects of divalent ions on other lipids have been well documented in many other studies; however, no studies have shown the impact of Mg^{2+} vs. Ca^{2+} with pH effects for DPPA.

Ca^{2+} and Mg^{2+} are observed to affect the protonation of DPPA, similar to Na^+ and K^+. At pH 10, the DPPA monolayer is predominantly singly protonated (-1) on pure water, but is fully deprotonated and bound by divalent cations. At pH 5.6, DPPA is mostly neutral on pure water but becomes singly protonated in the presence of cations. However, at a lower pH of 2.2, the DPPA isotherm on $CaCl_2$ remains the same as that of pH 5.6 (Fig. 4.6), which indicates that Ca^{2+} still binds to DPPA. DPPA is likely strongly bound in the presence of Ca^{2+}, existing as a 1:2 or 1:1 complex. This is further supported by expansion areas: when increasing the pH from 5.6 to 9.2, the expansion of DPPA area in the TC phase doubles from 1 to 2 $Å^2$/molecule. This expansion could reflect a change in the binding ratio from a 1:2 to 1:1 Ca^{2+}:DPPA complexation. A similar change in the complexation ratio in this pH range was also reported by Wang et al. for Ca^{2+} on dimyristoylphosphatidic acid (DMPA), an analogue of DPPA with 14 carbon alkyl chains.[91] Mg^{2+} also causes similar behavior, expanding the monolayer from 3 to 6 $Å^2$/molecule from pH 5.6 to 9.2. As only divalent and not monovalent cations display area doubling, this is attributed to their ability to complex neighboring DPPA molecules. Charge bridging by divalent cations can offset electrostatic repulsions and stabilize the monolayer. This explains why isotherms on divalent metal chloride solutions are more condensed than those on water for the same DPPA protonation state. Without the presence of cations at pH 5.6, DPPA would remain entirely protonated. However, adding Ca^{2+} or Mg^{2+} deprotonates the phosphate headgroup, causing the monolayer to expand; but cation lipid bridging prevents the monolayer from expanding as much as it would without ions.

In contrast to $CaCl_2$, DPPA isotherms on $MgCl_2$ at pH 2.2 are slightly less expanded compared to pH 5.6 (Fig. 4.6). While this could indicate the presence of all three DPPA species, it is unlikely that there would be any neutral DPPA species without any bound Mg^{2+}, particularly as an isotherm expansion is observed. It is more likely that there is a lower fraction of Mg^{2+} bound to the monolayer, resulting in a lower degree of deprotonation and thus a reduced expansion compared to pH 5.6. Therefore, Ca^{2+} displays stronger interactions with the phosphate headgroup compared to Mg^{2+}. Ca^{2+} has also been found to bind strongly with phosphatidic acid even at low micromolar concentrations.[114] However, a larger expansion of the monolayer is observed for Mg^{2+} than Ca^{2+} at all pHs. This can be reconciled and explained by Collins' law of matching water affinities. Ca^{2+} should have a higher binding affinity to phosphate than Mg^{2+} by forming a tight inner-sphere complex with phosphate. Mg^{2+} has more size mismatch with phosphate, being a small, hard cation, and holding its solvation shell more strongly than Ca^{2+}.[106] Thus, Mg^{2+} likely forms an outer-sphere solvent-separated complex with the phosphate headgroup. As Ca^{2+} forms tight inner-sphere complexes, it loses some of its hydration shell, which brings the bridging DPPA molecules closer together. Yet, the isotherm differences between Mg^{2+} and Ca^{2+} cannot be accounted for based only on ionic and hydrated radii differences. Such a small DPPA monolayer expansion below Ca^{2+} cross-sectional area is surprising and suggests that DPPA-ion interactions have little to do with steric effects.

4.3.3 Morphology of DPPA monolayers on water and salt solutions

Fig. 4.7 shows the BAM images of DPPA monolayers on water before and after the onset of the condensed phase at pH 5.6. DPPA starts in the G-LC coexistence phase as evidenced by the large bright areas of condensed lipid islands separated by dark lipid-poor regions. The monolayer quickly forms a homogeneous layer that remains stable even beyond the point of collapse. This is in contrast with an earlier study that reported small bright spots attributed to nucleation and collapse structures with long white striated streaks.[94] However, with NaCl, $CaCl_2$, and $MgCl_2$ solutions, these striated crystalline collapse structures are also observed (Fig. 4.8), indicating that cations are binding DPPA in a way to act as nucleation sites, instead of simply folding it into multilayered structures.

These nucleation sites may also act to stabilize the monolayer explaining the higher collapse pressures. Interestingly, these striated collapse structures are not observed for DPPA on KCl solutions as the images are indistinguishable from that on pure water (Fig. 4.8b). This indicates that K^+ does not nucleate crystalline aggregates, but instead forms less stabile amorphous structures. K^+ does not affect the collapse surface pressure compared to Na^+, Ca^{2+}, and Mg^{2+} (Fig. 4.3), except at high pH. This is further evidence of the relatively weak binding affinity of K^+. On the other hand, Na^+, Ca^{2+}, and Mg^{2+}, have higher collapse pressures correlated with the presence of the crystalline striations in the BAM images (Fig 4.8c-e).

4.4 Conclusion

DPPA molecules spread on neat water at $pH < 10$ are mainly comprised of neutral species and form closely packed monolayers. A change in the protonation state increases monolayer repulsion from the negative charges, resulting in weakening of the tight packing. However, we observe that DPPA monolayers require pHs higher than expected to deprotonate due to the negatively charged monolayers attracting H^+ to the surface. Cations reverse this increased pK_a trend by deprotonating the headgroup and shielding the charges. Divalent cations are also able to further mitigate monolayer disruption by bridging neighboring DPPA molecules. Based on the isotherm expansion, the following order of binding affinity can be deduced: $Ca^{2+} > Mg^{2+} > Na^+ > K^+$. This trend agrees well with that predicted from the law of matching water affinities, further supporting the empirically derived rule.

The unique surface behavior of DPPA is attributed to its small phosphate headgroup size and sterically open structure. As the headgroup is unencumbered by large moieties such as those found in other glycerophospholipids, the monolayer is able to pack tightly which inhibits steric insertion from ions. Thus it is electrostatics that primarily affects the protonation state and ultimately governs its monolayer behavior. DPPA headgroup interactions with cations and the resulting impact on the monolayer is extremely sensitive to environmental conditions of pH and relative abundance of ions. The extent of these interactions and their effect on DPPA surface speciation and surface pK_a will be investigated by surface-sensitive spectroscopy and discussed in the next chapter

DPPA-salt systems were chosen as proxies to further understand the surface properties of marine aerosols. DPPA monolayers on salt solutions serve as a model system of the organic layer on marine aerosols; it enables examination of surface processes such as film condensation and expansion, changes in lipid domain morphology (including refractive index changes), and cation-phosphate complexation, all of which have the potential to influence the evaporative and radiative properties, as well as the surface reactivity of marine aerosols. It is expected that charge speciation of the organic layer induced by pH and ionic composition of the aqueous core will impact marine aerosol processing and ultimately have direct and indirect effects on climate changes. Thus a better understanding of marine aerosol surface properties can benefit and help improve existing atmospheric simulations and climate modeling.

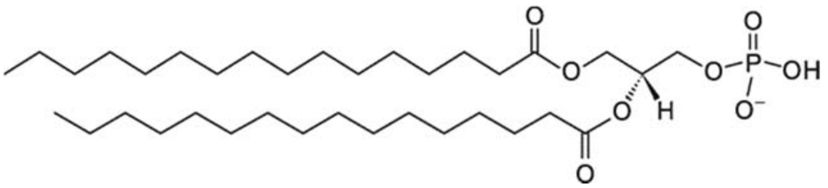

Figure 4.1 Chemical structure of (singly protonated) DPPA.

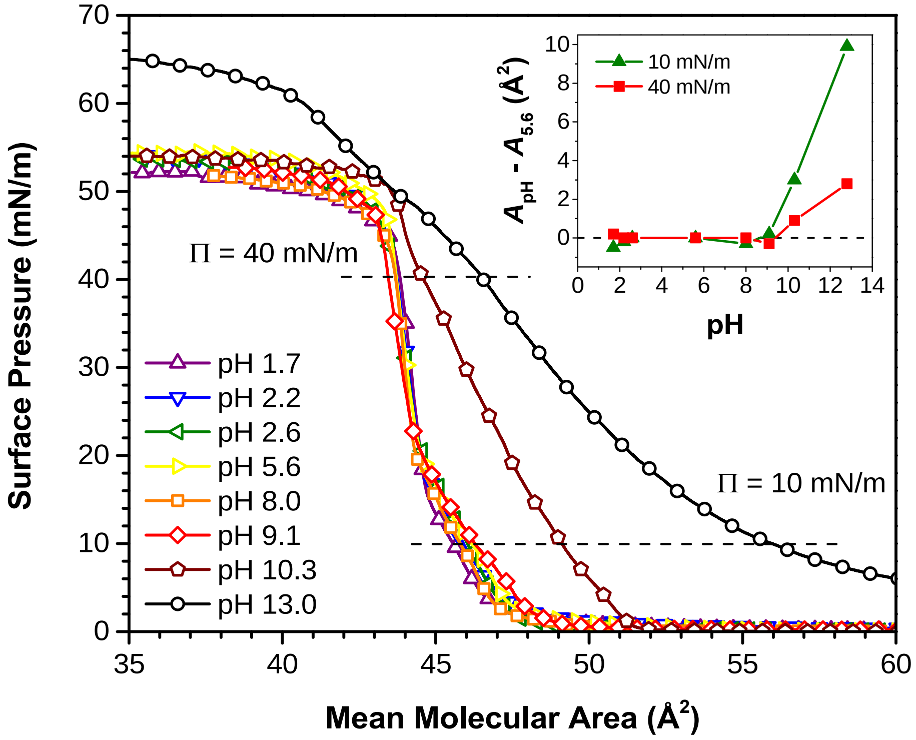

Figure 4.2 Compression isotherms of DPPA monolayers on water at various pH. Inset: Expansion of mean molecular area relative to water at pH 5.6 in the TC (10 mN/m) and UC (40 mN/m) phases.

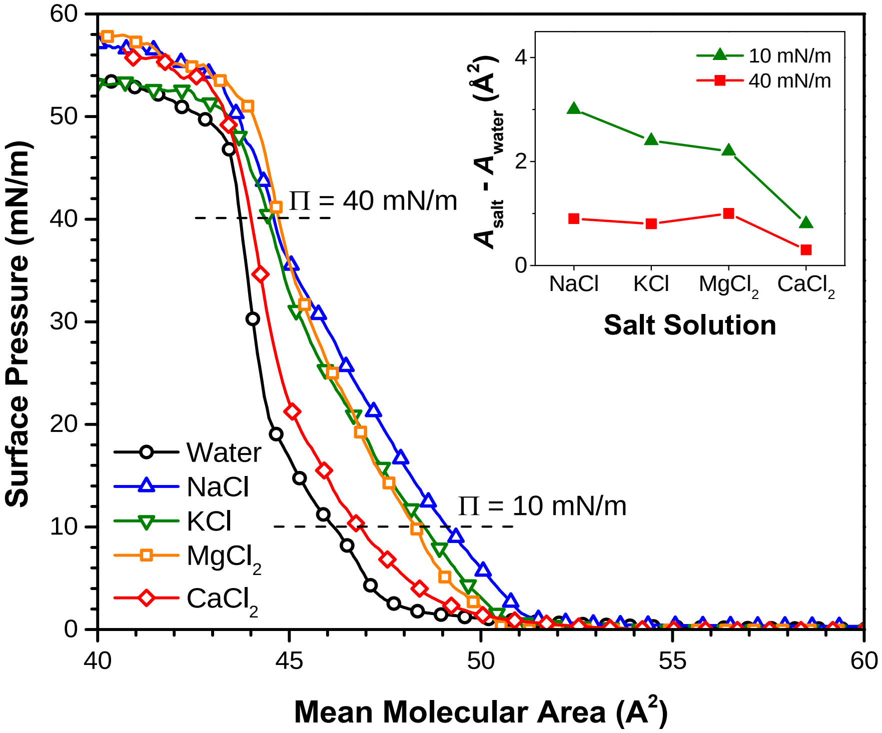

Figure 4.3 Compression isotherms of DPPA monolayers at pH 5.6 on different 0.6 M chloride salts aqueous solutions.

The isotherm on water is also shown for comparison. Inset: Expansion of mean molecular area relative to water at pH 5.6 in the TC (10 mN/m) and UC (40 mN/m) phases.

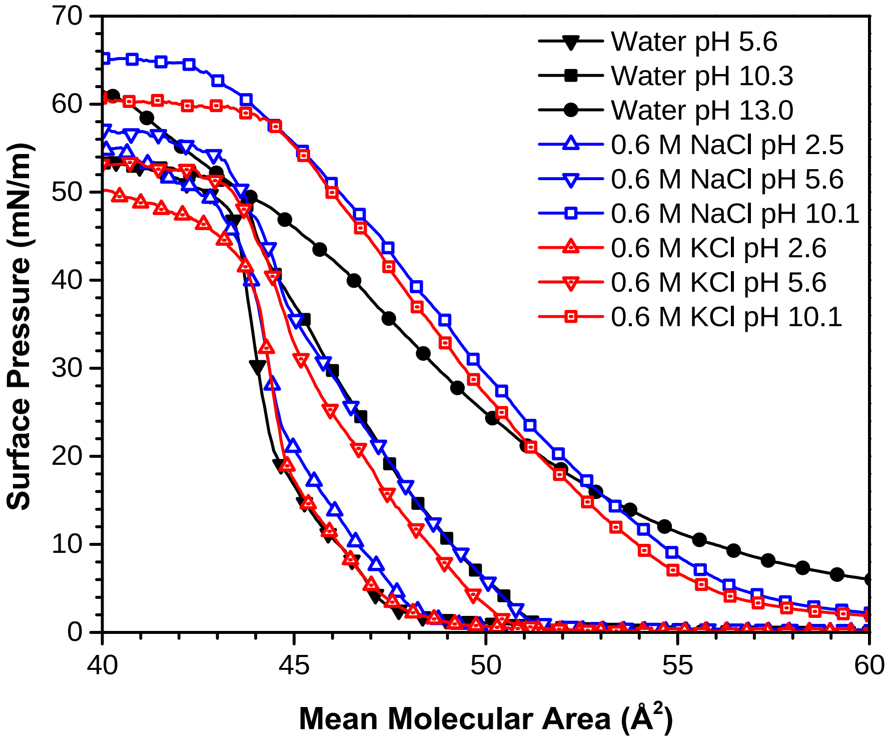

Figure 4.4 Compression isotherms of DPPA monolayers on 0.6 M monovalent (Na^+, K^+) chloride salt solutions at various pHs.

The isotherms on water are also shown for comparison. The DPPA isotherm on water at pH 2.6 is not shown as it is superimposable to the one at pH 5.6.

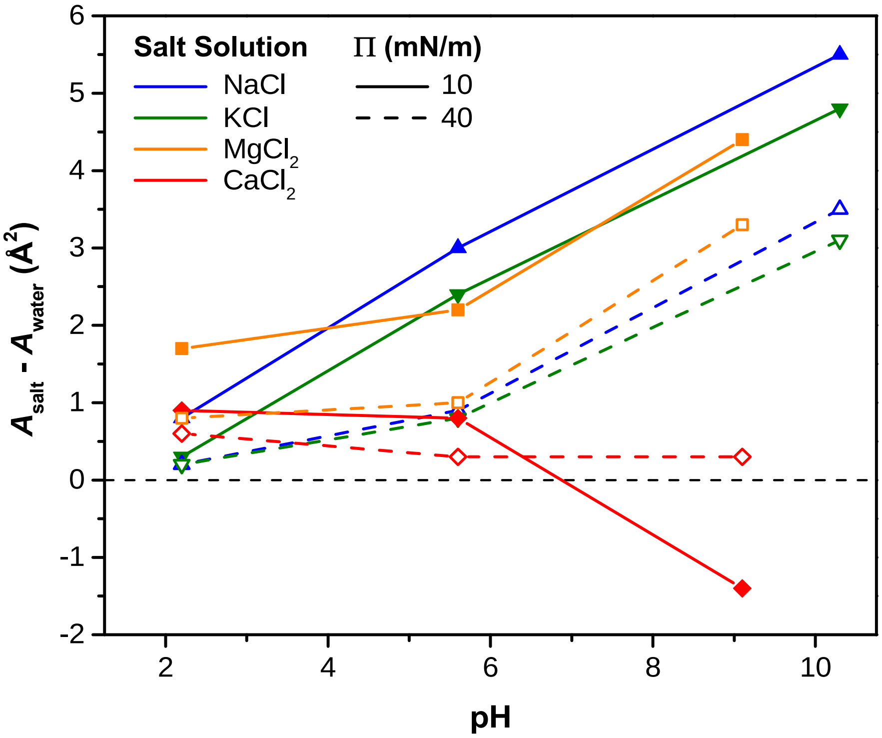

Figure 4.5 Mean molecular area expansion of DPPA monolayers on 0.6 M salt chloride solutions relative to water at various pH in the TC (10 mN/m) and UC (40 mN/m) phases.

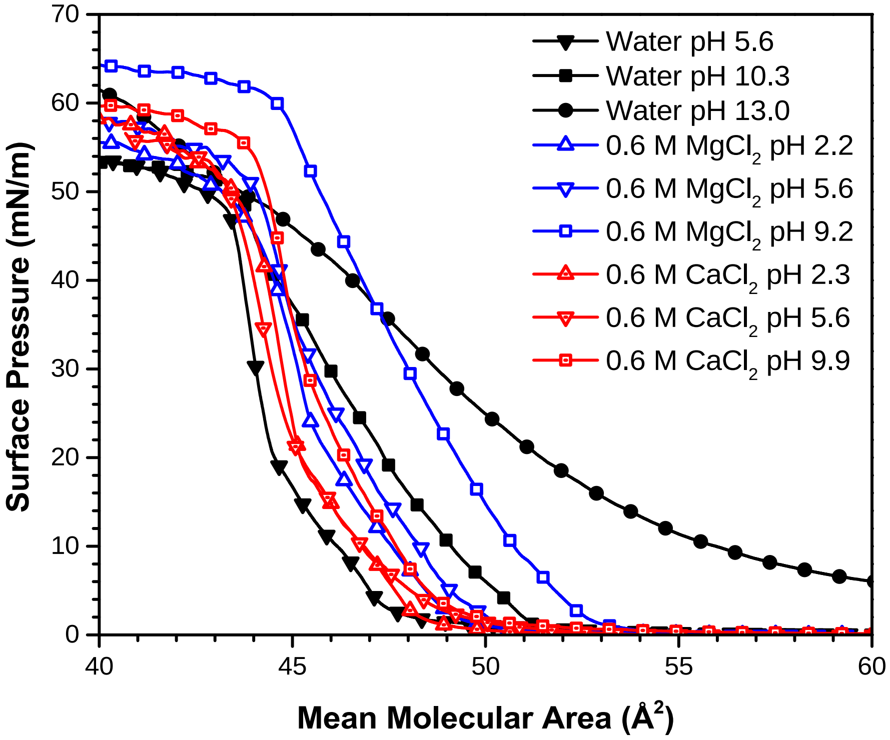

Figure 4.6 Compression isotherms of DPPA monolayers on 0.6 M divalent (Mg^{2+}, Ca^{2+}) chloride salt solutions at various pHs.

The isotherms on water are also shown for comparison. The DPPA isotherm on water at pH 2.6 is not shown as it is superimposable to the one at pH 5.6.

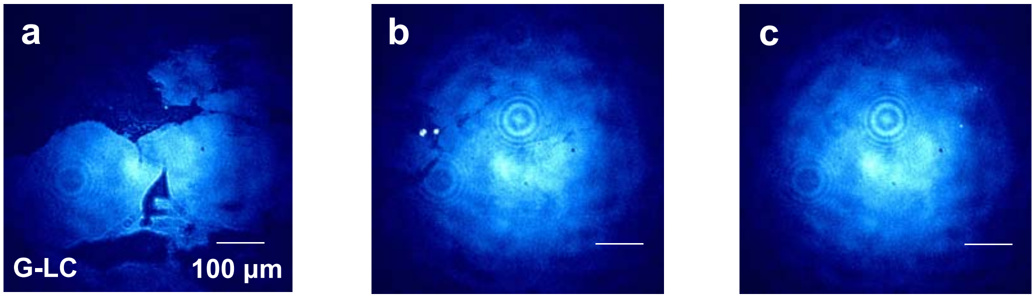

Figure 4.7 BAM images of a DPPA monolayer on water (pH 5.6) (a) in the G-LC phase (50 MMA), (b) at the onset of the TC phase (38 MMA), and (c) in the UC phase just prior to collapse (<34 MMA). Scale bar is 100 μm.
Circular interference patterns are due to dust particles.

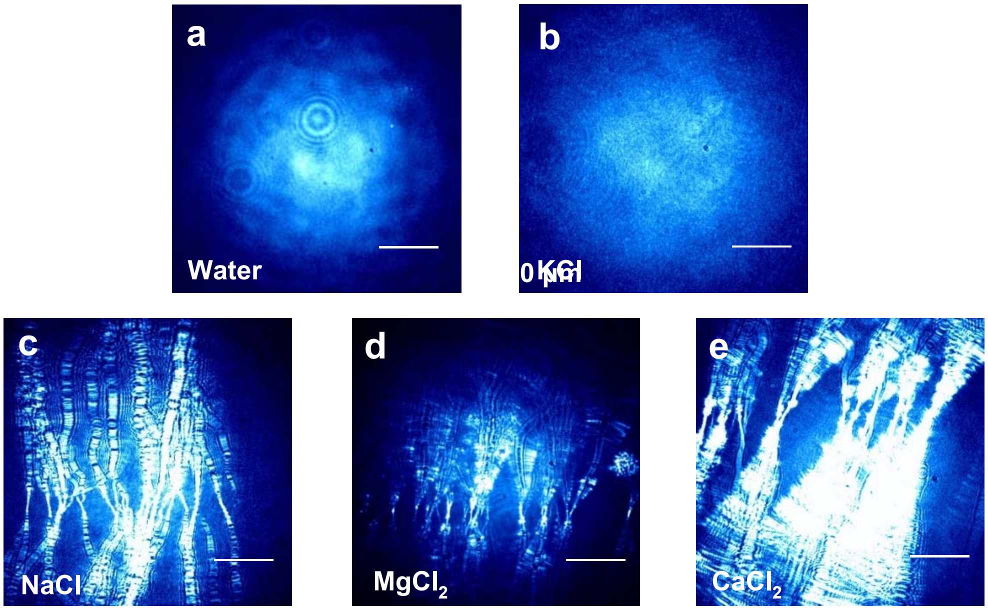

Figure 4.8 BAM images of DPPA monolayers in the collapse phase at pH 5.6 for (a) water, (b) NaCl, (c) KCl, (d) $MgCl_2$, and (e) $CaCl_2$ salt solutions. Scale bar is 100 μm.

Chapter 5. Effect of pH and Salt on surface pK_a of DPPA

Reprinted (adapted) with permission from (Zhang, T; Brantley, S.B.; Verreault, D.; Allen, H.C. "Effect of pH and Salt on Surface-pKa of Phosphatidic Acid Monolayers" Langmuir, 2018, 34 (1), 530–539.) Copyright (2018) American Chemical Society.

5.1 Introduction

The protonation state of an organic surfactant has a major impact on its monolayer behavior, surface organization and morphology.[115-118] Often, bulk pK_a values are used to determine speciation for surfactants, but it has been shown that the pH and pK_a of an organic surfactant can be very different at the surface compared to the bulk.[119-122] However, the actual surface speciation of a surfactant is not readily apparent and there needs to be a way to accurately account for the difference between bulk and surface-pK_a. While this has implications for all fields that deal with interfaces such as biological membranes and colloidal chemistry, one particular field of interest is aerosol chemistry, where surfactant speciation state directly affects aerosol properties.

Elucidating the surface speciation of organic surfactants commonly found on sea spray aerosols remains a non-trivial task even for relatively simple model systems. First, the bulk pH of sea spray aerosols can vary over a large range (from -0.51 to 9).[123-124] Secondly, the surface-pK_a can shift by a significant amount; for instance, it is known that palmitic and stearic acid, two fatty acids commonly occurring in marine aerosols, are protonated up to 4 pH units higher at the surface (surface-pK_a > 8) than in the bulk of aqueous solution due to two-dimensional ordering and ionic strength effects.[97-98] Significant pK_a shifts have also been reported for other types of organics adsorbed at aqueous surfaces.[96, 125] Adding to the complexity, salts as those found in seawater have also been reported to affect surface pH and pK_a.[116, 125-126] Thus, to fully understand the impact of an organic surfactant on sea spray aerosols, one must account for both pH and salt effects (0.1 M Na^+ in this study) on surface speciation.

In this work, dipalmitoylphosphatidic acid (DPPA) was selected as a relevant organic surfactant model to determine the impact of pH and salts on its protonation state. DPPA has a lone phosphate headgroup that makes it suitable for studying phosphate acid speciation within the interface. While we examined the general impacts of pH and specific cation effects on DPPA monolayer stability and protonation in Chapter 4, the surface speciation was not fully investigated. We had placed the surface-pK_{a2} somewhere in the range of 10-13, which we look to more accurately determine in this chapter. Using compression isotherms, surface tension pH titration, and surface-sensitive vibrational spectroscopy together with computer simulations, we go into further detail investigating the change in surface speciation of DPPA with pH, as well as with the addition of NaCl (0.1 M Na^+ in this study), the most abundant salt in seawater.[20] We experimentally determine the surface-pK_{a2} values under the different conditions between the three techniques and compare it with calculated pK_{a2} values using the Gouy-Chapman (GC) model to evaluate whether the surface pK_a can be accurately predicted.

5.2 Materials

1,2-Dipalmitoyl-*sn*-glycero-3-phosphate (DPPA) monosodium salt (>99%, lyophilized powder) was purchased from Sigma-Aldrich (St. Louis, MO) and used without further purification. DPPA solutions were prepared by dissolution in a 4:1 (v/v) chloroform-methanol (HPLC grade, Fisher Scientific, Waltham, MA) mixture. pH-adjusted aqueous solutions were obtained by addition or dilution of stock pH 1 and 13 solutions prepared from NaOH (99%, Mallinckrodt,St. Louis, MO) and HCl (trace metal grade, Fisher Scientific). NaCl (>99%, ACS certified, Fisher Scientific) was added to a set of pH solutions as a background electrolyte. All pH and salt solutions used ultrapure water with a resistivity of 18.2 MΩ·cm (Barnstead Nanopure Filtration System, model D4741, Barnstead-Thermolyne Corporation, Dubuque, IA) and a measured pH of 5–6. All references to pH in this paper refer to bulk pH unless specified as surface pH.

5.3 Results & Discussion

5.3.1 DPPA Speciation on Water and NaCl Solutions through Surface Tension pH Titration and Molecular Area Expansion

To measure the surface-pK_{a2} of DPPA, DPPA monolayers were examined using surface tension pH titration. This method has been successfully applied in our prior work, and also by Kanicky and Shaw, to determine the pK_as of various fatty acid monolayers from the neutralization endpoint.[98, 122] Following this method, HCl or NaOH is titrated into the subphase of a DPPA monolayer and the effect of changing pH on the surface tension is monitored. The surface tension is replotted as surface pressure for ease of viewing, as surface pressure is simply defined as the difference between measured surface tension of the solution and the surface tension of water, and corrected for the extra surface tension contribution from the added titrant volume.

Fig. 5.2 shows the surface tension pH titration curves plotted as surface pressure obtained by titrating from pH 13 to pH 5 DPPA monolayers at different lipid molecular areas. As the starting pH 13 solution was pH-adjusted with NaOH, the initial Na^+ concentration was already set to 0.1 M, which makes this technique more suited to determine the surface-pK_{a2} of DPPA on NaCl solutions than on pure water. The Na^+ concentration also remains fairly constant throughout the titration, as the titrant adds less than 10% to the total volume. Following Fig. 5.2 from low to high pH, it can be seen that in the most condensed phase (44 Å^2/molecule) the surface pressure starts to rise around pH 5.5 and increases monotonically with the pH. In addition, the onset of the surface pressure increase shifts to higher pHs with increasing MMA. These results are consistent with the surface pressure-area isotherms presented later, as the singly deprotonated and fully deprotonated DPPA species, which are increasingly present at higher pHs, are subject to stronger repulsive interactions from neighboring molecules, especially at small MMAs. Eventually the surface pressure reaches a maximum at pH > 12 for all MMAs.

The titration data was fit with a sigmoidal dosage response curve where the injection of HCl and resulting change in pH are treated as the dose and the surface pressure change as the response. This fit enables extraction of the 50% response value which corresponds here to the surface-pK_a. The fitted midpoint of the titration curve for the highly condensed DPPA monolayer (44 Å^2/molecule) gives a surface-pK_{a2} value of 10.5. The surface-pK_{a2} value decreases for DPPA at higher MMAs in the less condensed phases. For example, at 60 Å^2/molecule, where DPPA is in the gaseous phase at pH 5.6, the surface-pK_{a2} has dropped from 10.5 to 9.2. At larger MMAs, the monolayer is not as tightly packed and the DPPA molecules are much further apart, thereby reducing the surface charge density and resulting in less proton affinity and a surface-pK_{a2} value closer to that of the bulk. Taken together, these results clearly show that the DPPA surface-pK_{a2} is dependent on the coverage and, in turn, on the surface charge density of the monolayer. Moreover, these values are still greater than literature values of ~7.9-8.5 reported for vesicles, aqueous dispersions, and mixed monolayers of DPPA.[91-93, 127-128] We attribute this discrepancy between previously reported pK_a values to the sensitivity of DPPA to its local environment. For a DPPA monolayer such as in our study, the lipid is constrained to a 2D phase allowing for strong lateral interactions (e.g., chain-chain, headgroup-headgroup, etc.). However, the addition of zwitterionic DPPC in mixed monolayers would reduce the surface charge density and, in turn the difference between bulk and surface-pK_a. We have also shown that packing also affects surface-pK_{a2}; DPPA has outsized acyl chains relative to its phosphate headgroup and thus aqueous dispersions and micelles would have different packing and surface charge densities in bulk solution compared to that of a pure monolayer. Therefore, although our surface-pK_{a2} values differ from previously reported values, we maintain that there is no fundamental disagreement. These previous measurements of 7.9-8.5 are more reflective of bulk pK_as whereas our measurements are surface-pK_as.

The compression isotherms of DPPA monolayers on pure water and on strongly basic aqueous solutions, with and without NaCl, were also measured (Fig. 5.3). In pure water, it can be seen that DPPA isotherms progressively expand to larger MMAs with increasing pH. As previously reported, this monolayer expansion is induced by the change in the protonation state of DPPA with pH.[18] Another feature that appears at higher pHs is the occurrence of both expanded and condensed monolayer phases. Typically, there are strong attractive forces between headgroups and between alkyl chains of neighboring DPPA molecules such that a liquid-expanded (LE) phase is never observed in DPPA isotherms at low and neutral pHs, only liquid-condensed (LC) phases. However, as the DPPA headgroups become progressively negatively charged with increasing pH, the DPPA molecules are pushed further and further apart such that both LE and LE-LC coexistence phases are observed. As reported in our previous work, the fact that the LE-LC coexistence phase (seen as a plateau in the isotherm) is found only at pH > 11 is taken as evidence that a highly charged DPPA species, most likely the fully deprotonated species, is present in a significant amount.[18]

Further analysis of the isotherm molecular area expansion in the tilted-LC phase (30 mN/m; see the dotted horizontal line in Fig. 5.3a) relative to water shows that the onset of the expansion occurs somewhere between pH 9 and 10. The DPPA monolayer further expands with increasing pH, except over a very small pH range (~11.3–11.5) which appears as a kink with a flatter slope in Fig. 5.3c. For a condensed monolayer, at pH 10, the singly deprotonated DPPA species is predominant and yet due to the smaller sized headgroup relative to the tails, the monolayer is observed to expand; then, the further increase in pH leads to the occurrence of the fully deprotonated species. Between pH 11.3 and 11.5, the two negatively charged species may enhance hydrogen bonding which would temporarily counter the area expansion. This would suggest that the surface-pK_{a2} of the

DPPA phosphate headgroup can be found in that pH range. However, as the fully deprotonated species become predominant at even higher pHs, DPPA molecules are repelled even more strongly, causing another sharp increase in molecular area.

To account for the potential binding effect of Na^+ ions at highly basic pHs, compression isotherms were also measured for NaCl solutions with at least a constant 0.1 M Na^+ background concentration to match the Na^+ concentration of the pH 13 solution (Fig. 5.3b). (Compression isotherms on NaCl are identical from 0.05-1.2 M, reported in earlier work.[18]) An expansion in the isotherms was also observed on pH-adjusted NaCl solutions, far more than that on pure water at the same pH. As discussed previously, the presence of Na^+ cations in the aqueous subphase causes an expansion of the monolayer due to their insertion in the DPPA headgroup and interaction with the phosphate moiety.[18] As with pure water, the same expansion trend of DPPA with increasing pH is obtained on NaCl solutions, however, with one notable difference: the small kink previously found around pH 11.5 has now transformed into a quasi-plateau region and has shifted to lower pHs, between pH 10 and 11. This shift, which can be interpreted as a reduction of the surface-pK_{a2} of the condensed DPPA monolayer from 11.5 to 10.5, is consistent with our surface titration results. We attribute this to the charge screening of the monolayer by Na^+, which reduces the local surface H^+ concentration that otherwise exists near the negatively charged headgroups. This also serves to reduce the surface charge density, bringing the surface-pK_a closer to reported literature values.

5.3.2 Theoretical Peak Assignments of DPPA Phosphate Modes at Low and High Basic pHs

To more directly observe DPPA species present at lower and higher basic pHs, the protonation state of the phosphate headgroup was examined by looking at the phosphate modes with IRRAS. While surface-pK_{a2} values are determined from surface tension pH titrations and compression isotherms, these measurements remain macroscopic. In contrast, surface spectroscopic techniques such as IRRAS and vibrational sum frequency generation (VSFG) spectroscopy allows direct probing of the phosphate protonation state. Using these methods the protonation state of various chemical groups has been studied including carboxylic/carboxylates, phenol/phenolates, amines, and phosphate groups of other glycerophospholipids such as dipalmitoylphosphatidylcholine (DPPC) and dipalmitoylphosphatidylglycerol (DPPG), but so far not of phosphatidic acids.[100, 116, 119-120, 129-130] Spectral data of DMPA, a close analog of DPPA, has been reported previously, yet not always consistently, such that the peak assignment of the phosphate modes (PO_2^-, PO_3^{2-}) of DPPA remains ambiguous.[131] Adding to that, there is a paucity of theoretical data on the vibrational modes of DPPA. Therefore, a careful assignment and evaluation of the transition moment strength of each band associated with the different phosphate protonation states was first completed through DFT calculations.

The calculated IR spectra of the two DPPA charged species are shown in Fig. 5.4. The calculated IR spectrum of the fully deprotonated DPPA species has a characteristic doublet with peaks that appear at 1069 cm^{-1} and 1108 cm^{-1}. These features arise from the asymmetric PO_3^{2-}stretching ($\upsilon_{as}(PO_3^{2-})$) mode. If the PO_3^{2-} group was in a perfectly symmetric environment, the two PO_3^{2-} asymmetric stretch vibrations would be degenerate. However, these peaks are split because of the asymmetry of the fully deprotonated DPPA species with respect to its phosphate group. Because of the two-dimensional ordering and interactions between the DPPA molecules at the air-aqueous interface, this asymmetry is likely present in the phosphate headgroup region. The other prominent peak at 905 cm^{-1} in the calculated spectrum comes from the symmetric PO_3^{2-} stretching ($\upsilon_\mathrm{s}(\mathrm{PO}_3^{2-})$) mode. In contrast, the calculated spectrum of the singly deprotonated DPPA species has only two peaks from PO_2^- stretches: one at 1285 cm^{-1} and another at 1058 cm^{-1} corresponding to the asymmetric ($\upsilon_\mathrm{as}(\mathrm{PO}_2^-)$) and symmetric ($\upsilon_\mathrm{s}(\mathrm{PO}_2^-)$) stretches, respectively. The smaller intensity peaks in the latter spectrum generally do not involve phosphate vibrations, but instead motions of the C-O bond in the DPPA backbone.

5.3.3 DPPA Speciation on Water and NaCl through Phosphate Vibrational Modes Intensities

Fig. 5.5 shows the IRRAS spectra in the phosphate stretching region (950–1250 cm^{-1}) of DPPA monolayers on water and NaCl solutions with increasing pH. Due to the steric freedom and varied hydrogen bonding network of the phosphate headgroup, there is a large continuum of phosphate modes that overlaps with those of the DPPA backbone, such as the C-O-P stretch at 1108 cm^{-1}, and C-O-C asymmetric and symmetric stretches of the carbonyl esters at 1170 cm^{-1} and 1070 cm^{-1}, respectively.[116, 131] Because of this overlap, the discussion will focus hereafter only on the main phosphate modes. By comparing the relative peak positions and spectral features between the calculated and experimental spectra, four phosphate modes can be identified: the $\upsilon_\mathrm{as}(\mathrm{PO}_2^-)$ and $\upsilon_\mathrm{s}(\mathrm{PO}_2^-)$ modes of the singly deprotonated DPPA species, and the $\upsilon_{\mathrm{as}}(\mathrm{PO}_3^{2-})$ and $\upsilon_{\mathrm{s}}(\mathrm{PO}_3^{2-})$ modes from the fully deprotonated DPPA species. The broad peak observed in the IRRAS spectra at 1168 cm^{-1} is readily assigned to the $\upsilon_{\mathrm{as}}(\mathrm{PO}_2^-)$ mode, which lies in the range reported by Pézolet et al. for DMPA.[131] The peak position of this mode contrasts with the asymmetric (PO_2^-) modes of other phospholipids which are typically observed around 1250 cm^{-1}. This shift is attributed to various functional groups such as cholines and ethanolamines attached to the phosphate of other phospholipids but absent with DPPA. The next broad and more intense peak exhibits a doublet feature at 1095 cm^{-1} and 1108 cm^{-1} similar to the ones observed for $\upsilon_{\mathrm{as}}(\mathrm{PO}_3^{2-})$ in the calculated spectra and therefore can be assigned to this mode. The next expected peak would be the $\upsilon_{\mathrm{s}}(\mathrm{PO}_2^-)$, which lies close to the $\upsilon_{\mathrm{as}}(\mathrm{PO}_3^{2-})$ in the calculated spectra. Such a peak is also found in the IRRAS spectra at 1068 cm^{-1}. Although it is fairly weak, it disappears in response to increasing pH (see discussion below), thus confirming it as a mode associated with the singly deprotonated DPPA species. It is also expected that the $\upsilon_{\mathrm{s}}(\mathrm{PO}_2^-)$ peak has the weakest intensity, as transition moment is greater for asymmetric modes. The final major peak at 981 cm^{-1} is assigned to the remaining $\upsilon_{\mathrm{s}}(\mathrm{PO}_3^{2-})$ mode.

At pH 11 and below, the $\upsilon_{\mathrm{as}}(\mathrm{PO}_2^-)$ and $\upsilon_{\mathrm{s}}(\mathrm{PO}_2^-)$ modes are present, but not the $\upsilon_{\mathrm{as}}(\mathrm{PO}_3^{2-})$ and $\upsilon_{\mathrm{s}}(\mathrm{PO}_3^{2-})$ modes. Starting at pH 11.3, a dramatic increase in intensity of the $\upsilon_{\mathrm{as}}(\mathrm{PO}_3^{2-})$ and $\upsilon_{\mathrm{s}}(\mathrm{PO}_3^{2-})$ modes can be seen. Interestingly, the 1095 cm^{-1} peak of the $\upsilon_{\mathrm{as}}(\mathrm{PO}_3^{2-})$ doublet is more intense than the other peak at 1108 cm^{-1}, which can be attributed to the asymmetry of the phosphate group. As the mode increases in intensity and width, the two peaks merge into one broad peak with a small shoulder. Conversely, the $\upsilon_{\mathrm{as}}(\mathrm{PO}_2^-)$ and $\upsilon_{\mathrm{s}}(\mathrm{PO}_2^-)$ peaks decrease in intensity. This trend continues until pH 12, whereupon no further increase in peak intensity of the PO_3^{2-} modes is observed. These results further support the assignment of singly deprotonated and fully deprotonated phosphate headgroups, respectively, to lower and higher basic pHs. It is also clear that between pH 11 and 12, the fully deprotonated DPPA species becomes predominant and that the surface-pK_{a2} of DPPA is located in this range.

From a visual inspection of the spectra in Fig. 5.5a, the peak of the $\upsilon_{as}(PO_3^{2-})$ mode reaches about half its maximal intensity at pH 11.5. To get a more quantitative estimate of the DPPA surface-pK_{a2} value from the spectral data, the peak area of the $\upsilon_{as}(PO_3^{2-})$ mode was plotted as function of increasing pH and the midpoint determined by fitting the data to a sigmoidal curve, similar to the treatment of the surface tension pH titration data (Fig. 5.5c). The fitted midpoint gave a surface-pK_{a2} of 11.5, a value consistent with the other experimental results from surface tension pH titration and compression isotherms.

Another notable feature of the spectra is that although the $\upsilon_{as}(PO_2^{-})$ mode shrinks dramatically, it is still present at pH 12, while the $\upsilon_{s}(PO_2^{-})$ completely disappears at pH 11.3. It is possible that other overlapping DPPA modes could also be contributing to the remaining intensity of the $\upsilon_{as}(PO_2^{-})$ peak at pH 12 and above such as the CO-O-C asymmetric stretch. A small red shift of the $\upsilon_{as}(PO_3^{2-})$ mode from 1095 cm^{-1} to 1092 cm^{-1} with increasing pH was also observed. This could be due either to the $\upsilon_{as}(PO_3^{2-})$ mode itself having a different hydrogen bonding environment or to the interactions of Na^+ ions with the phosphate headgroup. For example, at pH 11, the Na^+ concentration is 0.001 M due to the use of NaOH to adjust the pH. Finally, it is worth mentioning that there are no peaks that could be assigned to the fully protonated DPPA species although they should be present and predominant at pH 2. Because the fully protonated and singly deprotonated species have the same symmetry, and that mode intensities decrease with decreasing charge, it was not possible to differentiate these two phosphate modes and determine the surface-pK_{a1} value with IRRAS. However, the surface-pK_{a2} can be clearly determined with spectroscopy as the singly deprotonated and fully deprotonated species have different spectral signatures.

5.3.4 DPPA Speciation on NaCl solutions with Constant Ionic Strength through Phosphate Vibrational Modes Intensities

IRRAS spectra in the phosphate stretching region of DPPA monolayers were also taken on NaCl solutions with a constant 0.1 M Na^+ background concentration to account for Na^+ effects on surface-pK_a (Fig. 5.5b). From the comparison with the spectra on water, Fig. 5.5b immediately shows that the vibrational modes associated with the fully deprotonated species emerge about one pH unit lower (at pH 10.5 instead of 11.5) on NaCl solutions, also consistent with surface tension pH titrations and compression isotherms that revealed that the presence of Na^+ decreases DPPA's surface-pK_{a2}.

One can also note that at pH 10 with a 0.1 M Na^+ background, the peak position of the $\upsilon_{as}(PO_3^{2-})$ mode has not shifted from 1095 cm^{-1}. Yet, when the peak intensity of the $\upsilon_{as}(PO_3^{2-})$ mode increases, it also follows the same ~3 cm^{-1} shift which is likely due to the mode itself, and not from Na^+ interactions. In fact, this also indicates that Na^+ ions are not interacting strongly to the phosphate headgroup, but rather complexed through longer range electrostatic interactions, and are also not responsible for the increase in intensity by changing the phosphate transition moment strength.[132]

5.3.5 DPPA Speciation on Water and NaCl Solutions using Gouy-Chapman Model

As shown by Vaknin and coworkers who previously calculated the species fractions of dimyristoylphosphatidic acid (DMPA), a shorter chain analog of DPPA, in the presence of Ca^{2+},[91] the Gouy-Chapman (GC) model can be used here to predict the DPPA monolayer speciation on water and NaCl solutions at different pHs. In order to determine the DPPA species fractions at a given bulk pH, one assumes a model DPPA (L) monolayer spread on an aqueous solution of fixed pH containing both hydronium (H^+) ions and sodium (Na^+) counter-cations. It is further assumed that these ions bind competitively with DPPA headgroups and that metal cations form 1:1 complexes. Under these conditions, the equilibrium protonation (proton binding) and complexation (metal binding) reactions are given by

$$\mathrm{LH_2^0} \rightleftarrows \mathrm{LH^-} + \mathrm{H}^+_{(aq)} \tag{2a}$$
$$\mathrm{LH^-} \rightleftarrows \mathrm{L^{2-}} + \mathrm{H}^+_{(aq)} \tag{2b}$$
$$\mathrm{LNaH^0} \rightleftarrows \mathrm{LH^-} + \mathrm{Na}^+_{(aq)} \tag{2c}$$
$$\mathrm{LNa^-} \rightleftarrows \mathrm{L^{2-}} + \mathrm{Na}^+_{(aq)} \tag{2d}$$

where $\mathrm{LH_2^0}$ denotes the fully protonated DPPA species, whereas $\mathrm{LH^-}$ and $\mathrm{L^{2-}}$ refer to the singly deprotonated and fully deprotonated species, respectively. $\mathrm{LNaH^0}$ and $\mathrm{LNa^-}$ represent the Na^+-lipid complexed species.

Taking into account the Boltzmann distribution of ions near the interface, the different DPPA species fraction in a monolayer spread on a NaCl (1:1 salt) solutions can be expressed as function of the equilibrium dissociation (K_{a1}, K_{a2}) and metal binding (K_{m1}, K_{m2}) constants as well as bulk pH such as (see Appendix C)

$$f_{\mathrm{L}^{2-}} = 10^{(2\mathrm{pH}_b - \mathrm{p}K_{a1} - \mathrm{p}K_{a2})} e^{2F\psi_0/RT} D^{-1} \tag{3a}$$

$$f_{\mathrm{LH}^-} = 10^{(\mathrm{pH}_b - \mathrm{p}K_{a1})} e^{F\psi_0/RT} D^{-1} \tag{3b}$$

$$f_{\mathrm{LH}_2^0} = D^{-1} \tag{3c}$$

$$f_{\mathrm{LNa}^-} = 10^{(2\mathrm{pH}_b - \mathrm{p}K_{a1} - \mathrm{p}K_{a2})} 10^{-(\mathrm{pNa}_b + \mathrm{p}K_{m2})} e^{F\psi_0/RT} D^{-1} \tag{3d}$$

$$f_{\mathrm{LNaH}^0} = 10^{(\mathrm{pH}_b - \mathrm{p}K_{a1})} 10^{-(\mathrm{pNa}_b + \mathrm{p}K_{m1})} D^{-1} \tag{3e}$$

with

$$\begin{aligned} D = 1 &+ 10^{(\mathrm{pH}_b - \mathrm{p}K_{a1})} \left(e^{F\psi_0/RT} + 10^{-(\mathrm{pNa}_b + \mathrm{p}K_{m1})} \right) \\ &+ 10^{(2\mathrm{pH}_b - \mathrm{p}K_{a1} - \mathrm{p}K_{a2})} \left(e^{2F\psi_0/RT} + 10^{-(\mathrm{pNa}_b + \mathrm{p}K_{m2})} e^{F\psi_0/RT} \right) \end{aligned} \tag{4}$$

where pH_b and pNa_b relate to the bulk H^+ and Na^+ ion concentrations, respectively. F represents the Faraday constant, R the ideal gas constant, ψ_0 the surface potential, and T the absolute temperature.

The surface charge density of a DPPA monolayer spread on a 1:1 salt solution (e.g., NaCl) is given by (see Appendix C)

$$\begin{aligned} \sigma(\psi_0) = \sigma_0 \Big[&\left(10^{(\mathrm{pH}_b - \mathrm{p}K_{a1})} + 10^{(2\mathrm{pH}_b - \mathrm{p}K_{a1} - \mathrm{p}K_{a2})} 10^{-(\mathrm{pNa}_b + \mathrm{p}K_{m2})} \right) e^{F\psi_0/RT} \\ &+ 10^{(2\mathrm{pH}_b - \mathrm{p}K_{a1} - \mathrm{p}K_{a2})} e^{2F\psi_0/RT} \Big] D^{-1} \end{aligned} \tag{5}$$

where $\sigma_0 = -2e/A_L$ is the maximal surface charge density of the fully dissociated (and non-complexed) DPPA headgroups, whereas e and A_L are the electronic charge and lipid MMA, respectively. The maximal surface charge density can be experimentally determined at each pH from the MMA of the compression isotherms found in Fig. 5.3. To solve Eq. 5 for the surface potential, the GC model is invoked where the surface charge density of a charged surface in contact with water or 1:1 salt solutions is given by

$$\sigma(\psi_0) = \sqrt{2\varepsilon_0 \varepsilon_r RT C_b \left(e^{-F\psi_0/RT} + e^{F\psi_0/RT} - 2 \right)} \tag{6}$$

where ε_0 and ε_r are the vacuum permittivity and relative permittivity of the aqueous phase (water or NaCl solution), and C_b the total bulk ion concentration.[133] Eqs. 5 and 6 can be simultaneously solved numerically to get the surface potential as function of the bulk pH, from which the DPPA species fractions (Eqs. 3a-e) can then be calculated (Table 5.1).

Fig. 5.6 shows the speciation curves of DPPA monolayers on water and NaCl solutions (see inset) as predicted by the GC model. For DPPA monolayers on water, the crossing point of the LH^- and L^{2-} species fractions points to a surface-pK_{a2} of 11.8, a value which lies in close agreement with the range determined experimentally from the compression isotherms. In the case of 0.1 M NaCl solutions, the surface-pK_{a2} appears to be around 11.0, a value slightly higher than those estimated from the isotherm data. The small discrepancy could be due to two factors, that the GC model remains usually valid for salt concentrations up to 0.1 M and for charged surfaces with surface charge density not exceeding ~0.35 C/m^2, and the errors in the surface potential (ψ_0) from the experimentally determined maximal surface charge density (σ_0).[116] In addition, the assumption that the DPPA phosphate headgroups can be considered as smeared charges is most appropriate when the Debye screening length is much larger than the headgroup size.[134] At 0.1 M NaCl, the screening length (~1 nm) starts approaching the headgroup size which could be a factor causing the observed discrepancy. However, theory does still fit and explain the experimental data well, which indicates that the pK_a differences between bulk and interface is primarily explained by surface charge density. A negatively charged surface, especially one that is closely packed such as that observed in a full monolayer has a more acidic interfacial pH than that of the bulk. However, addition of Na^+ screens the negatively charged phosphate headgroups to some degree, reducing the surface charge density and in turn, surface acidity and the surface-pK_a. Although only Na^+ was tested, it is reasonable to think that other ocean-relevant cations such as K^+, Ca^{2+}, and Mg^{2+} would also have an impact on a DPPA monolayer's surface-pK_{a2} value. As it has been shown that these cations display different binding affinities to the DPPA, we hypothesize that more strongly bound ions such as Ca^{2+} and Mg^{2+} would screen more effectively the negatively charged phosphate headgroups and decrease the surface-pK_{a2} closer to bulk values compared to weakly bound ones like K^+.[18] It also has been reported that there is a size-dependent organic and salt composition for organic-coated sea spray aerosols. Thus, following our results, we would expect that even aerosols with similar organic composition would display different hygroscopicities as their size, ion abundances and pHs vary, due to their resulting differences in surface-pK_a values and surface speciation.[17]

5.4 Conclusion

The surface speciation of monolayers and coatings made of organic surfactants is often characterized in terms of acid dissociation constants found for bulk systems (e.g., aqueous dispersions). However, in the case of monolayers, the choice of such constants can lead to incorrect estimations of the actual proportion of species fractions at a given pH. In this study, using three independent methods, compression isotherms, surface tension pH titration, and IRRAS, the surface-pK_{a2} value of a condensed DPPA monolayer was found to be 11.5±0.2 (summarized in Table 5.2), much higher than previously reported values of 7.9-8.5.[91-93, 127-128] However, as 0.1 M NaCl is added, the surface-pK_{a2} value decreased to

10.5. We also found that surface-pK_{a2} was dependent on surface coverage, from 11.5 for a full condensed phase monolayer, to 9.2 in the 2D gaseous phase. In addition, these results are consistent with predicted values from GC theory with associated assumptions for surface potential based on surface charge density.

Surface-pK_{a2} is shown to be greatly affected by surfactant surface packing as well as ion interactions. These effects ultimately lead back to surface charge density as the key driving force behind the differences between bulk and surface-pK_a values. Thus when estimating speciation for surfactants, one must account for ion concentrations as well as surface packing density to accurately predict their surface behavior. By incorporating these parameters into more accurate surface-pK_a estimates for surfactants, aerosol models can be improved to better understand their impact on climate.

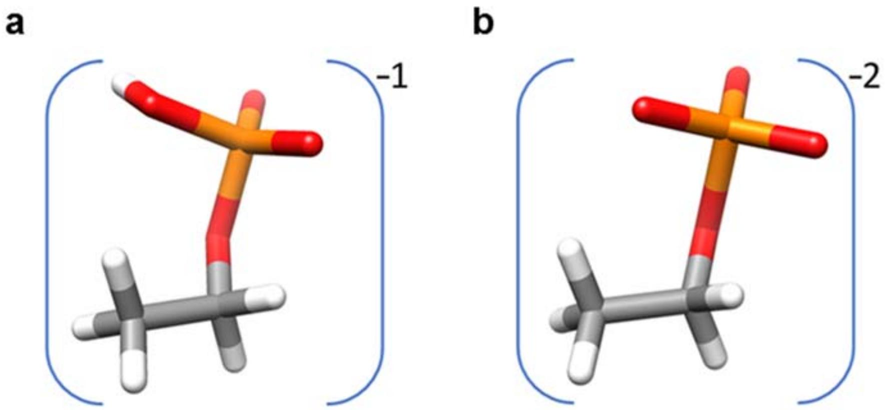

Figure 5.1 Optimized structures of truncated models of the DPPA molecule with protonation states of the phosphate headgroup corresponding to (a) low pH conditions where the headgroup is singly deprotonated ($(-PO_3H^-)$) and (b) high pH conditions where the headgroup is fully deprotonated ($(-PO_3^{2-})$).

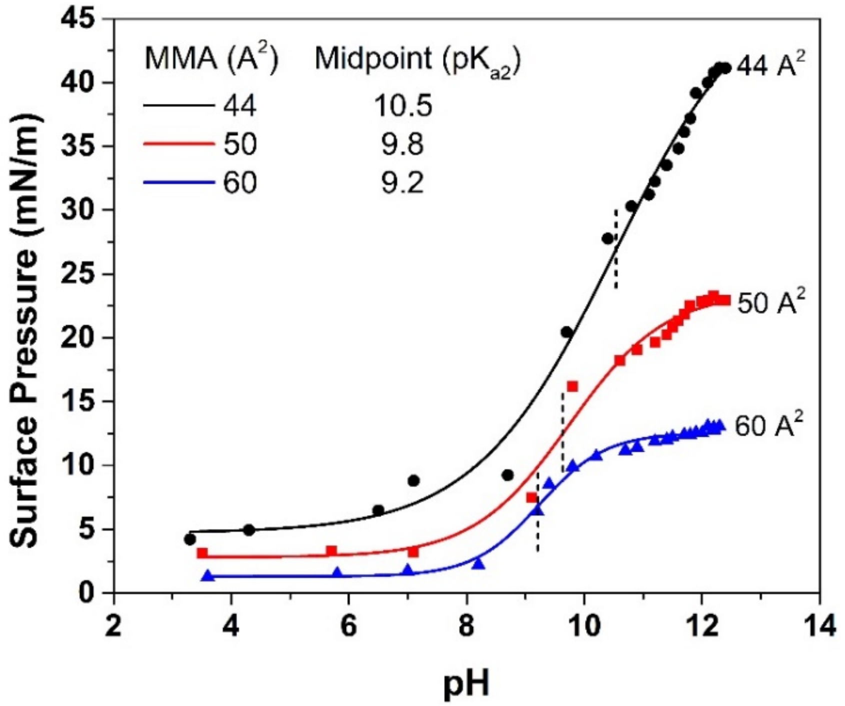

Figure 5.2 Surface pressure pH titration curves of DPPA monolayers on water at different MMAs.

A sigmoidal fit (curve) of the experimental data (symbol) was used to determine the surface-pK_a value at the titration midpoint.

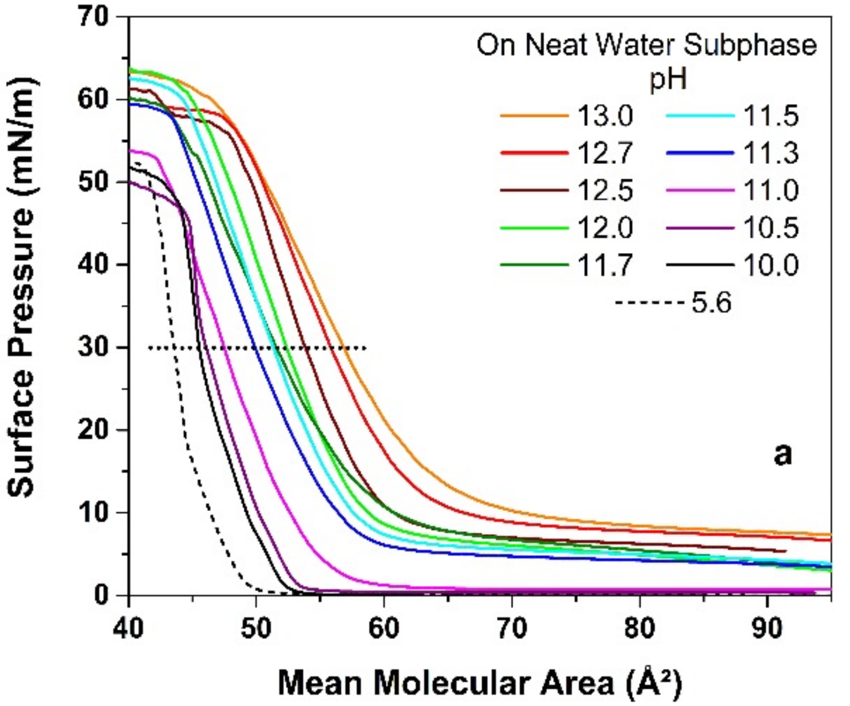

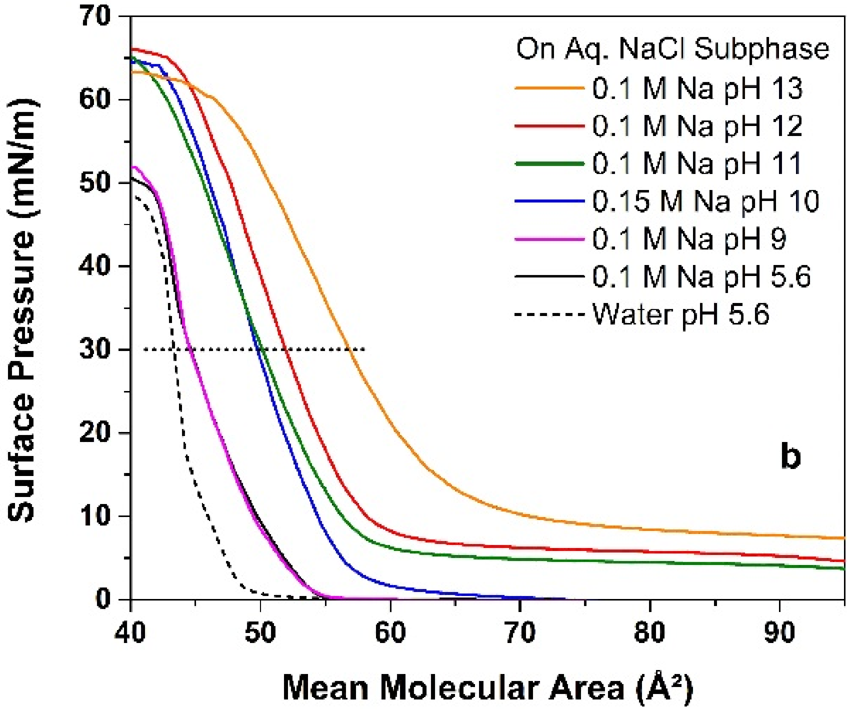

Figure 5.3 Surface pressure-area isotherms of DPPA monolayers on (a) water at various pHs, and on (b) NaCl solutions at various pHs and concentrations.

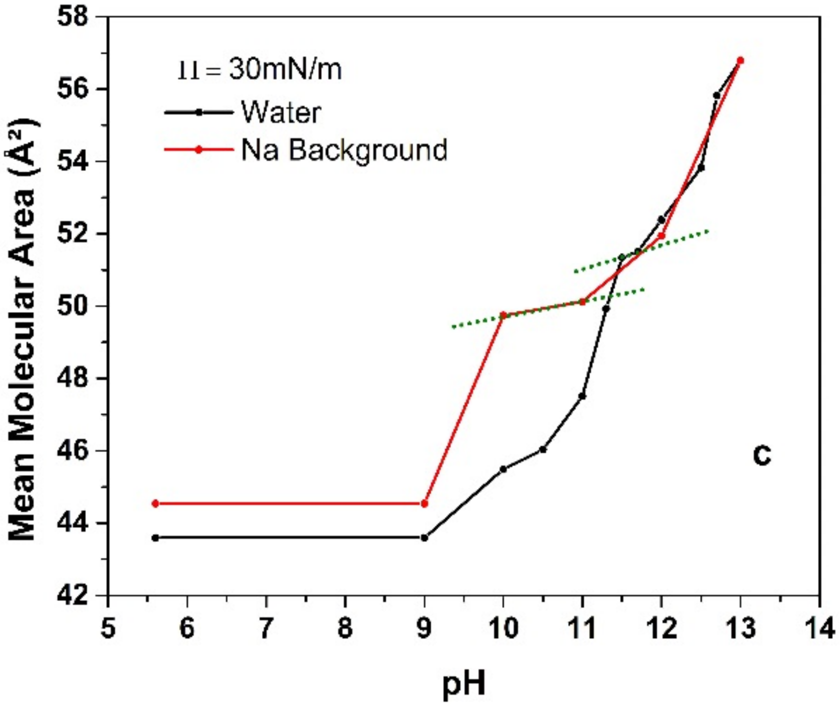

Figure 5.4 Surface pressure-area isotherms of DPPA monolayers on (c) Mean molecular area expansion in the LC phase (30 mN/m; black dotted lines in a, b) for water and NaCl solutions.

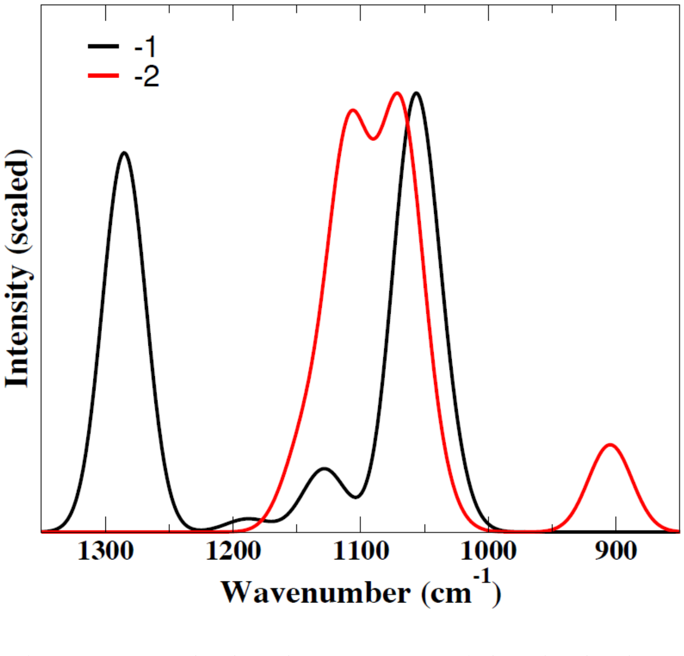

Figure 5.5 Calculated IR spectra of the singly deprotonated (black) and fully protonated (red) truncated DPPA molecules in the range between 800 and 1400 cm^{-1} that includes the phosphate stretching region (950–1250 cm^{-1}) vibrational modes.

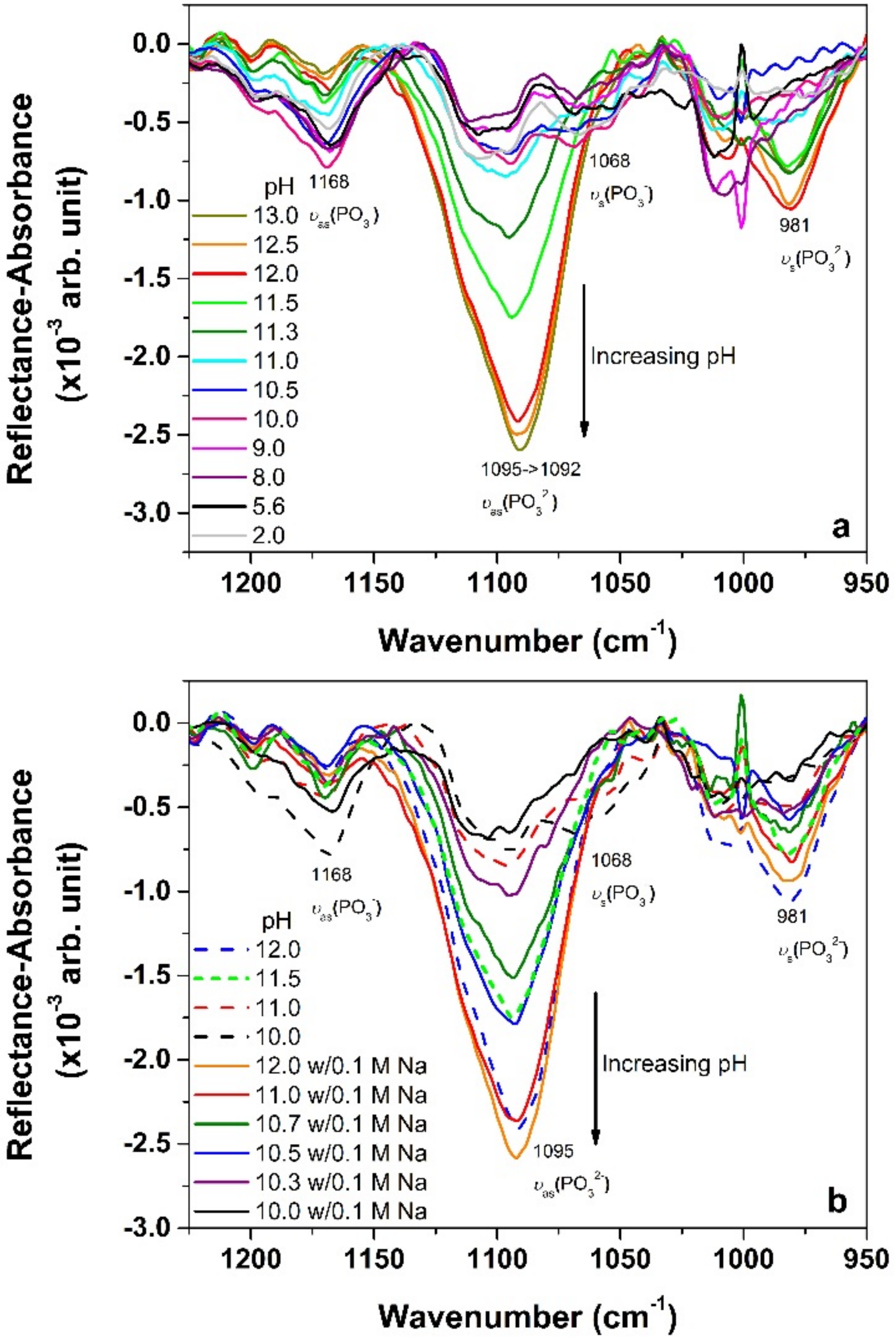

Figure 5.6 IRRAS spectra in the phosphate stretching region of DPPA monolayers at different pHs (a) on water (b) on 0.1 M NaCl.

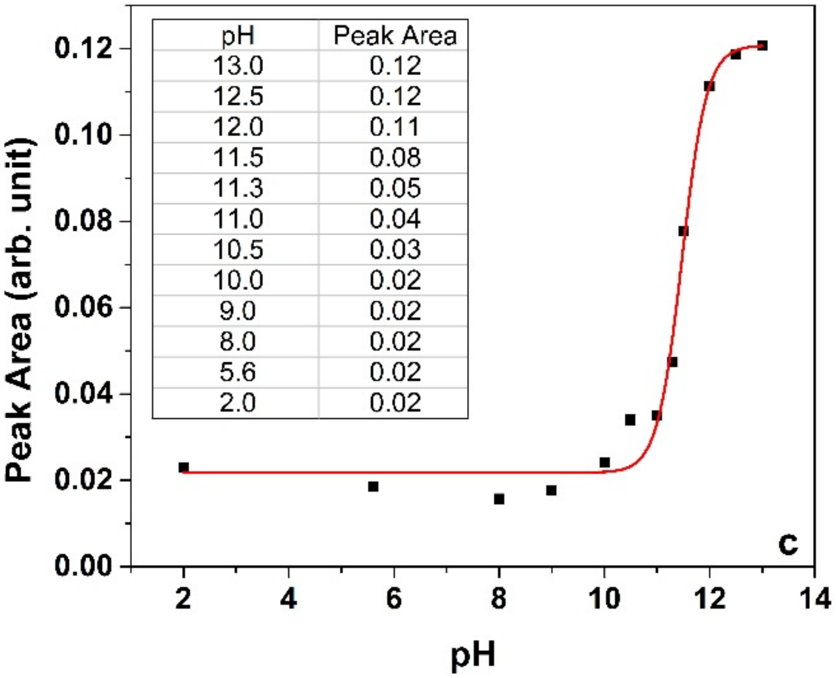

pH	Peak Area
13.0	0.12
12.5	0.12
12.0	0.11
11.5	0.08
11.3	0.05
11.0	0.04
10.5	0.03
10.0	0.02
9.0	0.02
8.0	0.02
5.6	0.02
2.0	0.02

Figure 5.7 IRRAS spectra in the phosphate stretching region of DPPA monolayers at different pHs (c) Peak area of the $\upsilon_{as}(PO_3^{2-})$ mode from the IRRAS spectra of DPPA monolayers on water at different pHs.

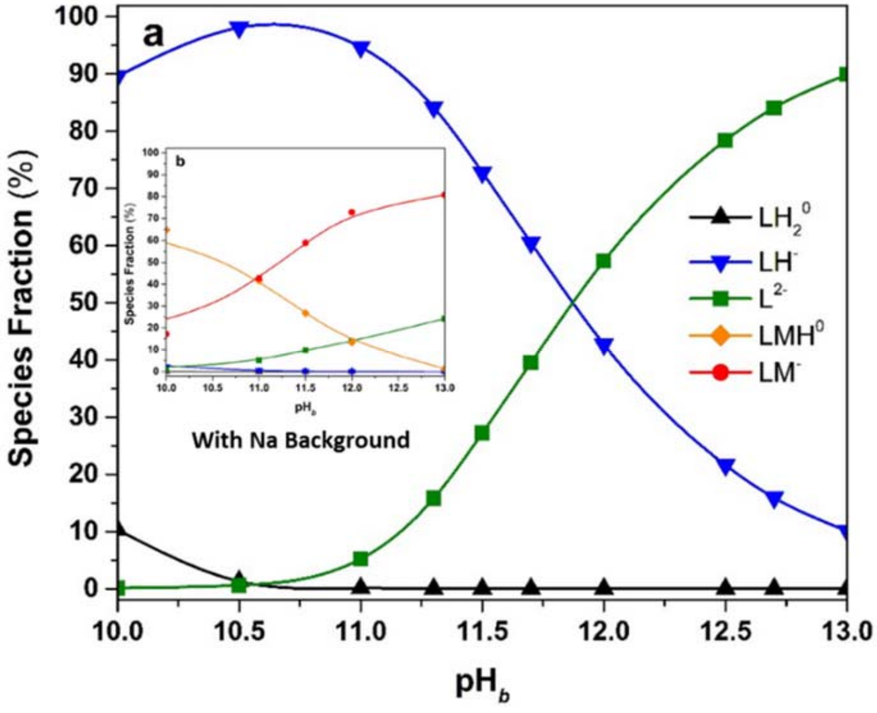

Figure 5.8 DPPA species fractions as predicted by the Gouy-Chapman model.

The predicted DPPA species fractions for NaCl solutions at constant ionic strength are shown in the inset. Curves are used here only as an eye guide.

Table 5.1 Predicted species fraction (%) for DPPA monolayers on water and 0.1 M NaCl aqueous solutions at different pHs and MMAs.[a]

pH_b	MMA (Å^2)		Species Fraction (%)[b]							
	Water	0.1 M NaCl	Water			0.1 M NaCl				
			L^{2-}	LH^-	LH_2^0	L^{2-}	LH^-	LH_2^0	LM^-	LMH^0
5.6	43.59	45.83	0.0	1.8	98.2	0.0	15.7	0.8	0.0	83.5
10.0	45.59	49.74	0.1	89.6	10.3	0.7	2.2	0.0	17.2	64.7
10.5	46.03	–	0.6	98.1	1.3	–	–	–	–	–
11.0	47.51	50.12	5.2	94.7	0.1	5.2	0.5	0.0	42.7	41.6
11.3	49.93	–	15.8	84.2	0.0	–	–	–	–	–
11.5	51.34	–	27.2	72.8	0.0	9.8	0.2	0.0	58.9	26.7
11.7	51.51	–	39.5	60.5	0.0	–	–	–	–	–
12.0	52.38	51.94	57.3	42.7	0.0	13.8	0.1	0.0	72.8	13.4
12.5	53.83	–	78.4	21.6	0.0	–	–	–	–	–
12.7	55.82	–	84.1	15.9	0.0	–	–	–	–	–
13.0	56.79	56.79	89.9	10.1	0.0	24.2	0.0	0.0	80.7	1.3

[a] For the calculations, the following parameters were used: $T = 295.15$ K, $\varepsilon_{r,w} = 79.46$ [135], $\varepsilon_{r,\mathrm{NaCl}\ 0.1\ \mathrm{M}} = 79.45$ [136], $pK_{a1} = 3.0$, $pK_{a2} = 7.1$ [91], $pK_{m1} = -0.44$ and $pK_{m2} = +1.00$ [137]; [b] Values smaller than 0.05 were set to zero.

Table 5.2 Summary of the surface-pK_{a2} values of condensed DPPA monolayers determined experimentally and from the GC model.

Method	**pK_{a2}**	
	Water	0.1 M NaCl
Surface tension pH titration	-	10.3-10.7
Compression isotherms	11.3-5	10-11
IRRAS	11.5	10.5
GC model	11.7	10.7

Chapter 6. Effect of Trace Metal Ocean Cations on DPPA

Reproduced in part with permission from Zhang, T; Fiamingo, M.E.; Allen, H.C. "Trace Metal Enrichment driven by Phosphate Functional Group Binding Selectivity" *JGR Oceans*, **2018**. Copyright American Geophysical Union.

6.1 Introduction

Trace metals have been found to be selectively enriched in the sea surface microlayer (SSML) due to association with organics, but the underlying cause of this selectivity has not been as well studied. The phosphate headgroup was observed to exhibit the strongest trace metal binding and greatest impact on surface metal enrichment. By applying the Langmuir- Szyszkowski model to the surface tension salt titration of DPPA, the cation surface affinities for phosphatidic acid were determined, with $Al^{3+} > Fe^{3+} \sim> Zn^{2+} > Mg^{2+} > Ni^{2+} > Mn^{2+} \sim Ca^{2+}$, an order not predicted from bulk properties such as solid formation constants of metal-phosphonates. Thus cation binding to surface active organic molecules with phosphate ester head groups is indicated to be a significant source of trace metal enrichment within the SSML. In this study, the interactions of several ocean surface enriched metals (Ca, Mg, Mn, Ni, Zn, Al, Fe) with DPPA are investigated using Brewster angle microscopy (BAM), surface tension salt titration (STST), and infrared reflection absorption spectroscopy (IRRAS). We focus on the phosphate headgroup, quantifying its metal cation surface binding affinity through changes in surface tension of DPPA.

6.2 Materials

1,2-Dipalmitoyl-sn-glycero-3-phosphate (DPPA) monosodium salt (>99%), 1,2-dipalmitoyl-sn-glycerol (DAG, >99%) , and stearic acid (SA, >99%) were purchased from Sigma-Aldrich (St. Louis, MO) and dissolved in 4:1 (v/v) chloroform-methanol (HPLC grade, Fisher Scientific, Waltham, MA) mixture. $CaCl_2$, $MgCl_2$, $MnCl_2$, $NiCl_2$, $ZnCl_2$, $AlCl_3$, and $FeCl_3$, salts were also purchased from Fisher Scientific (>99%). Aqueous solutions of pH 3 and 5.6 were obtained by addition of HCl (trace metal grade, Fisher Scientific, Accumet Basic AB 15 pH Meter, Fisher Scientific). All pH and salt solutions used ultrapure water with a resistivity of 18.2 MΩ·cm (Milli-Q® Advantage A10, MilliporeSigma, Burlington, MA).

6.3 Results & Discussion

6.3.1 Surface Pressure – Area Isotherms & Brewster Angle Microscopy

To further explore binding differences between metal cations to the phosphate ester headgroup of DPPA, compression π-A isotherms of DPPA along with BAM on various salt solutions were first performed as a general indicator of cation affinity. Fig 6.2 shows the π-A isotherms of DPPA on various salt solutions at pH 5.6. The π-A isotherm of DPPA has been discussed earlier in this thesis, exhibiting a tilted-condensed (TC) and untilted-condensed (UC) phase, and a collapse pressure of 55 mN/m.[18, 93, 138] The salts can be grouped into three categories. The first category contains Ca^{2+}, Mg^{2+}, Ni^{2+}, and Mn^{2+} and display similar behavior, in which the DPPA monolayer is expanded, a single broad liquid-condensed (LC) phase is present, and a higher monolayer collapse pressure is observed. As discussed in an earlier chapter, Mg^{2+} displays a higher binding affinity to phosphate than Ca^{2+} due to the larger expansion and impact on the monolayer. Mn^{2+} and Ni^{2+} display similar trends, with the Mn^{2+} isotherm almost identical to that of Ca^{2+}, and Ni^{2+} slightly more expanded than Mg^{2+}. From qualitative analysis of the isotherms, one orders the metal ion affinity to DPPA solely on the basis of monolayer expansion as $Ni^{2+} > Mg^{2+} > Ca^{2+} \sim Mn^{2+}$.

The second category of salt contains only $ZnCl_2$, which condenses and orders the monolayer to a large extent. This trend explains the unique decrease in surface tension observed in the Zn^{2+} surface tension titration of DPPA (Fig. 6.2). While Zn^{2+} is known to exhibit condensing effects on other phospholipids such as DPPC, these other lipids have larger headgroup radii relative to alkyl tails.[139] However, the alkyl tails in the case of DPPA have a larger radii than the lone phosphate headgroup and thus are the limiting size factor in how tightly the monolayer can pack. Zn^{2+} is observed to completely eliminate the TC phase, so that the alkyl chains of DPPA are oriented as vertically as they can be, and packed as tightly as DPPA allows. This indicates a strong binding effect of Zn^{2+} on DPPA, and thus Zn^{2+} is ordered ahead of the other ions Ni^{2+}, Mg^{2+}, Ca^{2+} and Mn^{2+}.

The third category of salts contains the trivalent ions Al and Fe. On the basis of charge alone, we expect a higher binding affinity than the divalent ions; the isotherms with Al and Fe salts show a very early binding effect even when the lipid is more dispersed at larger MMAs. In addition, the isotherm slopes are smaller, and extend over very large MMAs, suggesting that the tails are fairly disordered. Also, a lower collapse pressure of

<50 mN/m is observed indicating the monolayer is not as stable compared to that of on neat water or in an aqueous divalent salt solution.

To further investigate the monolayer behavior and the effect of binding, Brewster angle microscope images were obtained simultaneously during π-A isotherm compression. Fig. 6.3 shows the BAM images of DPPA on aq. $MnCl_2$, $NiCl_2$, $ZnCl_2$, $AlCl_3$, and $FeCl_3$ solutions during the condensed and collapsed monolayer phases (row a and row b, respectively). BAM images of DPPA on water, $CaCl_2$ and $MgCl_2$ are found in the previous chapter.[18] $MnCl_2$, $NiCl_2$, and $ZnCl_2$ all show similar images to those reported on $CaCl_2$ and $MgCl_2$. DPPA on aq. divalent salt solutions exhibits a very homogenous monolayer in the condensed phase, and forms white striated strands upon monolayer collapse. (DPPA on water displays a homogenous film for all phases.) DPPA on aq. $ZnCl_2$ in particular exhibits a dense almost mat-like bundle of collapse fibers with fewer water gaps than other salts, an indication of zinc's high ability to bind and condense DPPA homogeneously. In contrast to the divalent salts, trivalent cations of $FeCl_3$ and $AlCl_3$ have noticeably different BAM images. DPPA under the influence of $FeCl_3$ and $AlCl_3$ no longer exhibit a full coverage monolayer, but instead aggregate into island-like domains, which also remain when the monolayer has collapsed. Although $AlCl_3$ causes a small amount of striated collapse structures, there continues to be the presence of large island domains as well as dark regions which are water rich areas. We assert that $AlCl_3$ and $FeCl_3$ bind to DPPA strongly, greatly disrupting the monolayer relative to the divalent salts.

6.3.2 Surface Tension Salt Titrations

To quantify the surface binding affinity of various ions to DPPA, we employ a unique approach: treating the ions as surfactants and fitting the STST data in Fig. 6.1 to the Langmuir-Szyszkowski equation. This model describes the relationship between surface tension and concentration of the surface active species

$$\gamma = \gamma_0 - \mathit{\Gamma} RT \ln(1 + KC) \tag{6.1}$$

where γ is the surface tension of the solution, γ_0 the surface tension of water, $\mathit{\Gamma}$ the surface excess, R the gas constant, T the temperature, K the surface adsorption constant, and C the concentration.[140-141]

Although the Langmuir-Szyszkowski model has been well studied and documented for single component non-ionic organics, by making several assumptions we can treat the metal ions as behaving similarly. First we view the condensed phase DPPA monolayer as a solid surface. Although DPPA itself is a surfactant, its double 16-carbon alkyl tails strongly constrains it to the interface. DPPA has been shown to be highly surface active at all ionization states from (0) to (-2), with no change in solubility observed as its ionization state changes unlike single chain fatty acids that display increased solubility as they become more negatively charged.[122] As shown in chapter 2, BAM images of DPPA in the condensed phase (>0 mN/m surface pressure) revealed a homogenous film covering the water surface [18]. In addition, DPPA is very stable at the air-water interface. Thus, we treat the DPPA monolayer as a solid phosphoric acid-water interface. Second, although cations are not surfactants by definition, they act as pseudo-surfactants by binding to a phosphate ester headgroup-water interface. While the DPPA monolayer displays lower surface tension than that of water, the surface tension is altered by the presence of ion binding as observed both in the isotherm (Fig. 6.2) and STST (Fig. 6.1) measurements. By changing the surface tension of the DPPA surface, the metal ions meet the definition of a surfactant, although they are still labeled "pseudo-surfactants" as they are not inherently surfactants. Third, the Langmuir-Szyszkowski equation is designed for nonionic surfactants as it does not account for electrical double layer (EDL) effects. At our working pH of 3, DPPA is fully protonated and the monolayer is neutral. To bind to DPPA, a cation must displace a hydrogen, but the negative charges on the phosphate ester headgroup are still neutralized by cations resulting in a net neutral monolayerFinally, we assume that the "pseudo-surfactant" behavior of cations is similar enough amongst each other to constitute a homological series, as the only thing changing is the cation.[141] Thus we treat Γ as a constant for all metal cations (Γ=2 for our fit).

In addition, to accurately discuss metal ion binding, the issue of speciation must be accounted for. We use the program ChemEQL (EAWAG, Dübendorf, Switzerland) to calculate the thermodynamic equilibrium concentrations of various salt species at different pH. At pH 3, not only is the DPPA monolayer charge neutral, but most of the salts Ca^{2+}, Mg^{2+}, Mn^{2+}, Ni^{2+} exist primarily as their free (aquo) ion form in solution. However, Zn^{2+}, Al(III), and Fe(III) have a significant fraction of complexed species (Fig. 6.5). For Zn, up to pH 8, there is a ~20% fraction of $ZnCl^+$ species, but the dominant species in solution is still the free ion Zn^{2+}. Al and Fe solutions are even more fractionated with multiple competing hydroxide complexes, with $Al(OH)_3$ being the dominant species for Al, and no clear dominating species for Fe at pH of 3.

The surface tension changes of the divalents fit well to the Langmuir-Szyszkowski model, with calculated K and fit values listed in Table 6.1. As mentioned earlier, white insoluble $Zn(OH)_2$ precipitate forms beyond 0.03M, limiting fitting to the lower concentrations, and increasing the fit error. From the fit, the order of binding affinity to surface phosphate is $Zn^{2+} > Mg^{2+} > Ni^{2+} > Mn^{2+} \sim Ca^{2+}$. While we have observed stronger binding affinity of Mg^{2+} over Ca^{2+} in previous work, it is surprising that Ni^{2+} and Mn^{2+} have lower fitted adsorption constants. In other phosphate studies in bulk solution such as phosphonic acids and phosphonates, the typical order observed was $Zn^{2+} > Mn^{2+} > Ni^{2+} > Mg^{2+} > Ca^{2+}$.[142-145] The order is also very different when comparing K_{sp} value for solid metal-phosphates, with the order $Ca^{2+} > Zn^{2+} > Ni^{2+} > Mn^{2+} > Mg^{2+}$. Clearly the metal cation affinities for bulk phosphates differ from that of surface phosphate ester headgroups and we theorize that this trend is closely dependent on the water and hydrogen bonding structure around the phosphate ester - ion interactions. DPPA monolayers form a strongly hydrogen bonded network and the phosphate headgroups are well hydrated.[18] Of our selected divalent ions, Ca^{2+} and Mn^{2+} have smaller hydrated radii and less water molecules in their hydration shell (7 and 9 respectively), whereas Mg^{2+}, Ni^{2+}, and Zn^{2+} have larger hydrated radii with ~10 water molecules in their shell (Table 6.2).[146] Metal ion binding with surface phosphate ester headgroups appears to be water mediated and favors cations with larger hydration sheaths. In addition, Zn^{2+} has an abnormally high fit K value. Despite the formation of insoluble hydroxy species impeding the fit, the high value suggests that there is another mechanism at play, separate from the phosphate ester - water interactions.

To further explore the differences between metal cations, we turn to IRRAS studies, discussed below.

In contrast to the divalent cations, the trivalent ions Fe^{3+} and Al^{3+} do not fit to the Szyszkowski model. The Szyszkowski model assumes a complete homogenous phosphate headgroup surface; in the BAM images (Fig. 6.3), the divalent metal ions reveal that they meet that requirement, whereas Al^{3+} and Fe^{3+} do not. The presence of water rich regions in the BAM images for Al^{3+} and Fe^{3+} means there is no longer a fully covered surface as the trivalent ions induce large aggregate formation, thus explaining the poor fit. This difference in binding mechanism between trivalent and divalent metal ions is also different enough to constitute our prior assumption invalid, thus Γ is no longer constant for Al^{3+} and Fe^{3+} cations. In addition, as observed from speciation plots, the free metal ion is not the dominant species for Al^{3+} and Fe^{3+}, with different competing surface adsorption constants complicating the fit. However, even though we cannot quantitatively compare surface adsorption constants between divalent and trivalent ions, it is still quite clear that trivalent metal ions have higher binding affinity than divalent metal ions.

6.3.3 Infrared Reflection Absorption Spectra of DPPA with Metal Ions

To further investigate the molecular mechanism of metal cation binding differences to DPPA, IRRAS spectra were taken of DPPA on various salt solutions in the condensed phase (30mN/m). Fig. 6.4 shows the IRRAS spectra of DPPA in the PO stretch region. The IRRAS spectrum of DPPA has been discussed in chapter 2, with a υ_{as}-PO_2^- mode at 1168 cm^{-1} and a υ_{as}-PO_3^{2-} doublet mode at 1108 and 1095 cm^{-1}. The 1095 cm^{-1} peak of the doublet results from a phosphate oxygen orienting closer to the surface and interacting with the lipid backbone, breaking the expected C_3 symmetry. The υ_{as}-PO_3^{2-} doublet is sensitive to deprotonation, increasing in intensity, and merging into a single large peak centered at 1095 when the monolayer is fully deprotonated.[75] Metal ion binding to the DPPA phosphate ester headgroup might be expected to display similar spectral behavior, but does not. For Ca^{2+}, Mg^{2+}, and Ni^{2+}, the υ_{as}-PO_3^{2-} mode remains a low intensity doublet, with no spectral shift. Although it is clear from surface tension data that there is interaction between the metal ions and the phosphate ester headgroup, the lack of a blue shift implies no dehydration of the phosphate ester, and thus a significant hydration sheathe is expected to be present between the two.[116, 147] Mn^{2+} behaves only slightly different, with the 1108 cm^{-1} peak far more intense than the 1095 cm^{-1} peak. This implies a different binding coordination geometry as the Mn^{2+} is likely interacting more with the phosphate oxygens. While the reason is unclear, it has been well documented in the literature that Mn^{2+} interacts with all 3 phosphate groups of adenosine triphosphate (ATP) compared to Mg^{2+} which only interacts with 2 phosphate groups.[148] Mn^{2+} is described in these biological systems as a cooperative binder; the difference in coordinating with more phosphate headgroups could explain the different interaction of Mn with regard to the 1095 cm^{-1} P-O stretch. However, the overall intensities of all four ions (Ca^{2+}, Mg^{2+}, Mn^{2+}, Ni^{2+}) remain low as the 1095 cm^{-1} peaks are not larger than the intensity of their respective υ_{as}-PO_3^- peaks. This strongly suggests that the metal ions are binding via solvent shared mechanisms, with the phosphate headgroups retaining its hydration and hydrogen bonding network.

In contrast, Zn^{3+}, Al^{3+}, and Fe^{3+} ions show significant spectral differences compared to Ca^{2+}, Mg^{2+}, Mn^{2+}, and Ni^{2+} ions. For Zn^{2+}, the υ_{as}-PO_3^{2-} is blue shifted and forms a single peak centered at 1113 cm^{-1}, with a dramatic increase in intensity. This blue shift is indicative of phosphate dehydration, and when coupled with surface tension data showing strong zinc binding, points to covalent interactions between Zn^{2+} and phosphate. Although Zn^{2+} binding to proteins has been well studied in biochemical systems, much less is discussed in literature with regards to Zn^{2+} binding such as to ligands or inorganic anions including phosphate.[149] It is known that Zn^{2+} has a much higher affinity for ligands than alkaline earth metals like Ca^{2+} and Mg^{2+}, this affinity also extends to water complexation. Whereas the other divalent metal ions bind water electrostatically, Zn^{2+} interactions with water are significantly covalent in nature, as evidenced by its high heat of Zn^{2+} ion solvation.[150] This is also consistent with the high Szyszkowski K value compared to the other divalent metal ions. In addition, due to its full d-shell and consequential lack of ligand field stabilization, Zn^{2+} is flexible in adapting to many coordination states.[149] Compared to the other ions, Zn^{2+} can form tetrahedral complexes, which could allow it to sit neatly in one of the tetrahedral pockets of the phosphate group. It is also known that alongside HS^- and sulfate, phosphate is one the strongest inorganic anions for buffering Zn^{2+} ions in cells.[149] We conclude that even though Zn^{2+} covalently bonds with water ligands, the phosphate ester ligand is more favorable for binding, and therefore there is a phosphate – water exchange process with Zn^{2+} resulting in stronger inner-sphere covalent binding between Zn and DPPA.

Al also exhibits a blue shift to 1113 cm^{-1}, pointing to strong covalent interactions between the phosphate ester headgroup and Al^{3+}, analogous to Zn^{2+}. Aluminum is well known to be a strong phosphate binder; it has been used as a phosphate binding agent for reducing intestinal phosphate absorption.[151] It has been reported that phosphate ions undergo ligand exchange with –OH to form strong inner-sphere complexes with aluminum hydroxide.[152] We can conclude a similar case occurring here, that $Al(OH)_3$ is undergoing ligand exchange with the phosphate headgroup to form inner-sphere complexes, or binding directly in the case of the free Al^{3+} ion.

The IRRAS spectra of DPPA on aq. $FeCl_3$ solution is unique as the υ_{as}-PO_3^{2-} peak shows a strong increase in intensity, but the peak is still centered at 1095 cm^{-1}, indicating primarily deprotonation.[75] However, the peak is also broad and still contains shoulders including the 1108 cm^{-1} doublet, and significant covalent contributions at 1113 cm^{-1}. It is surprising that covalent 1113 cm^{-1} peaks are not the dominant ones in the Fe^{3+} spectra even though iron compounds such as hematite (Fe_2O_3) and goethite ($FeO(OH)$) have been studied to bind phosphate via strong inner-sphere complexation at low pHs.[153] However, according to the Fe^{3+} speciation plot, at pH 3 multiple species such as $Fe_3(OH)_4^{4+}$, $FeCl^{2+}$, Fe^{3+}, and $FeOH^{2+}$ are all present and competing to bind to the phosphate headgroup. It is known that Fe-phosphate complexation is quite complex, with a wide range of affinities and labilities that is also pH dependent for each individual species. We can hypothesize that weaker or ionic binding from the iron hydroxide and chlorides are contributing to the broad range of non-covalently bound phosphate peaks. Even though Fe^{3+} shows strong binding, it is difficult to analyze with all the species present as each binds with the phosphate differently. However, it is still clear that Al^{3+} displays a higher phosphate affinity than Fe^{3+}. Because Fe^{3+} displays a range of binding motifs both covalent and noncovalent, it is possible that some Fe^{3+} species have a lower affinity for phosphate at pH 3 relative to Zn^{2+}.

Finally, we note that the C=O mode at 1740 cm^{-1} and the CH_2 scissoring mode at 1468 cm^{-1} do not display any changes from pure water upon metal ion binding; thus no dehydration of the C=O moiety, and no change in the hexagonal packing structure (Fig. 6.6).[53] We attribute this to the packing of DPPA rigid intramolecular network, making the C=O less accessible to metal ion binding.

6.4 Conclusion

The enrichment of trace metals in the sea surface microlayer is primarily driven by surface active organics, particularly organic phosphates, and although field measurements have reported phosphate enrichment alongside trace metals, there is an insufficient physical understanding of the mechanism behind trace metal enrichment. In this study, we have quantified surface adsorption constants of trace metals to a phosphate headgroup-lipid monolayer as a way of comparing binding constants to the SSML phosphate. We found that trivalent cations have a higher binding affinity than the divalent cations in the order of $Al^{3+} > Fe^{3+} \sim>\sim Zn^{2+} > Mg^{2+} > Ni^{2+} > Mn^{2+} \sim Ca^{2+}$, with Fe^{3+} being variable due to its complex dependence on speciation and pH sensitivity. Unsurprisingly the trivalent metal cations also organized the surface morphology of the DPPA monolayer differently than divalent metal cations. Thus the driving forces of metal cation binding to surface phosphate are in strength order: cation charge ($3^+ > 2^+$), followed by the ability to form strong inner-sphere complexes (inner-sphere > outer-sphere), and finally increasing hydration sphere size for weakly bound cations that interact mainly through electrostatics (10 waters in shell > 6 waters in shell).

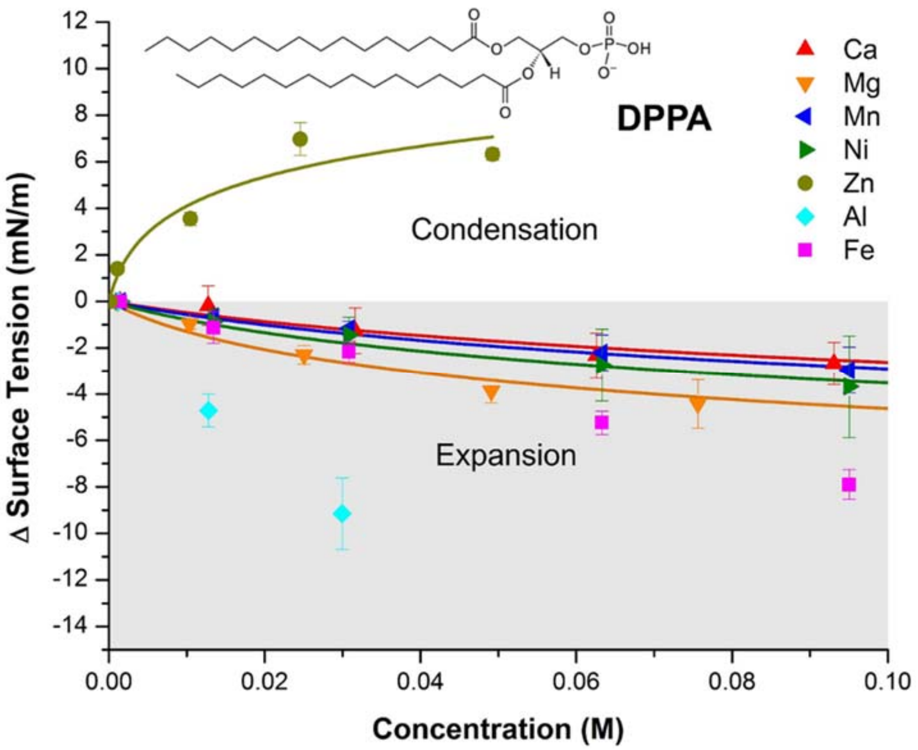

Figure 6.1. Surface tension changes of DPPA as a function of metal salt concentration on pH 3 solutions.
Solid lines are the Szyszkowski fit with the parameters given in Table 1. White and gray areas correspond to condensation/expansion areas relative to on pure water in Π-A isotherms (Fig. 6).

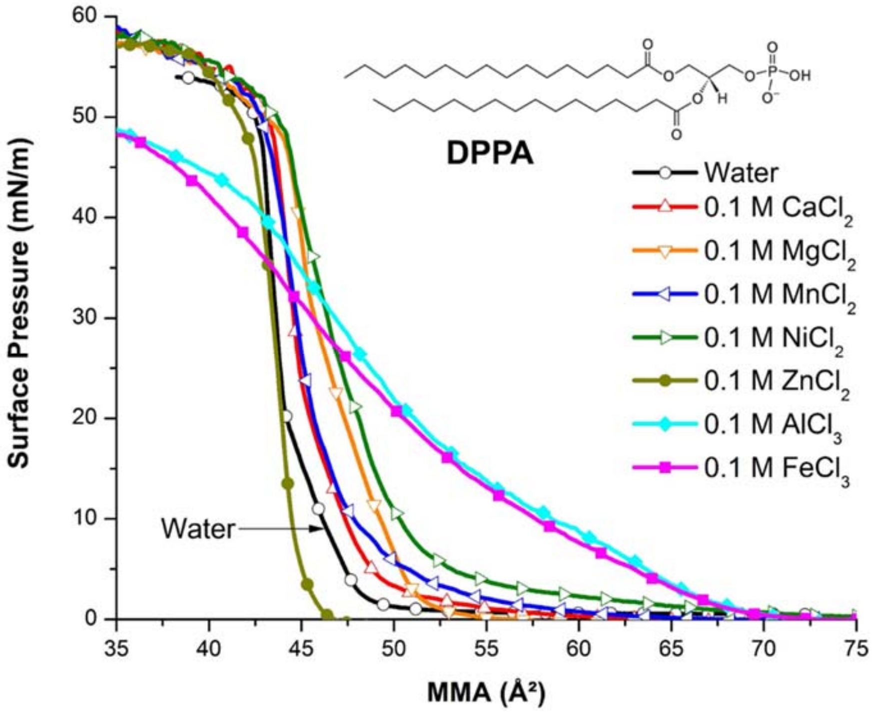

Figure 6.2 Figure 0.2Π-A isotherm of DPPA on water and various 0.1 M salt solutions.

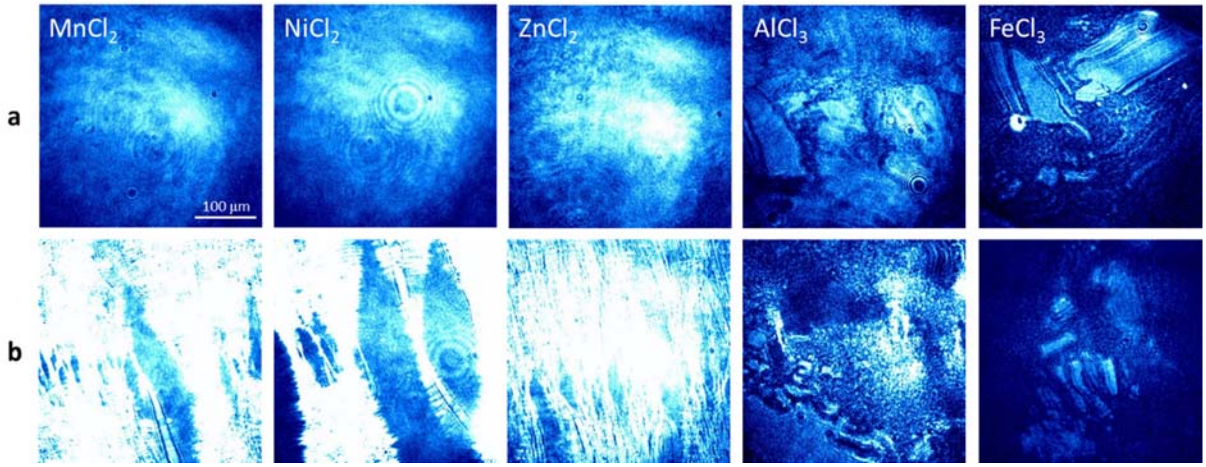

Figure 6.3 BAM images of DPPA on various salts in the condensed phase (row a) and collapsed phase (row b). Dark areas represent water rich regions. Bright areas represent lipid rich regions.

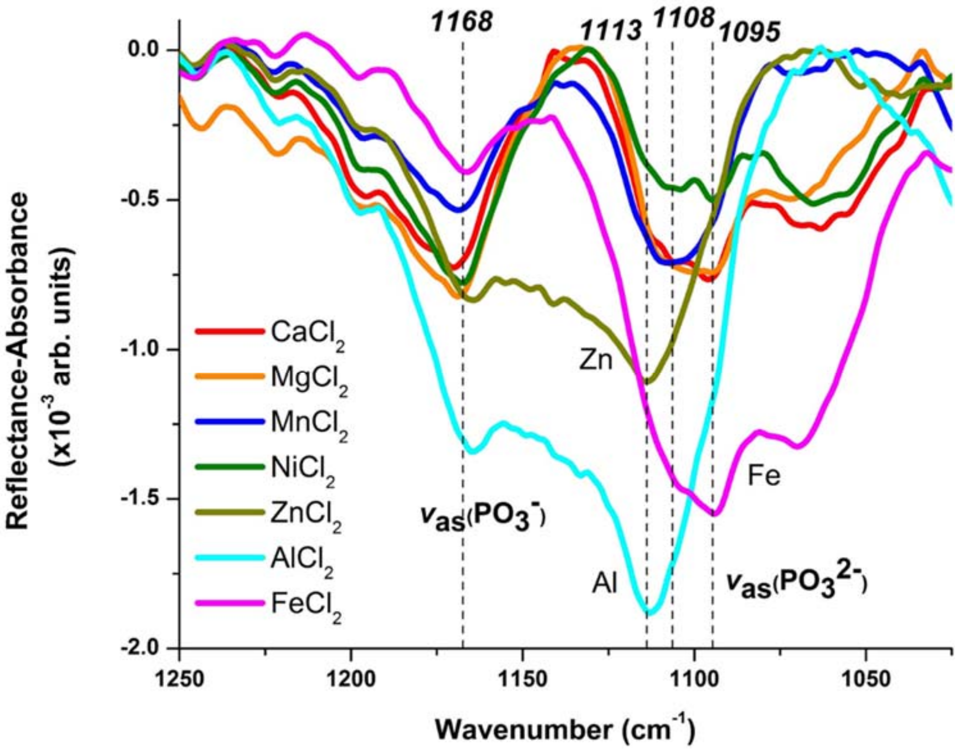

Figure 6.4 IRRAS spectra in the phosphate region of DPPA on various 0.1 M salt solutions. The υ_{as}-PO_3^{2-} peak positions are cation selective for Fe, Al, and Zn at1095, 1108, and 1113 cm^{-1}, respectively.

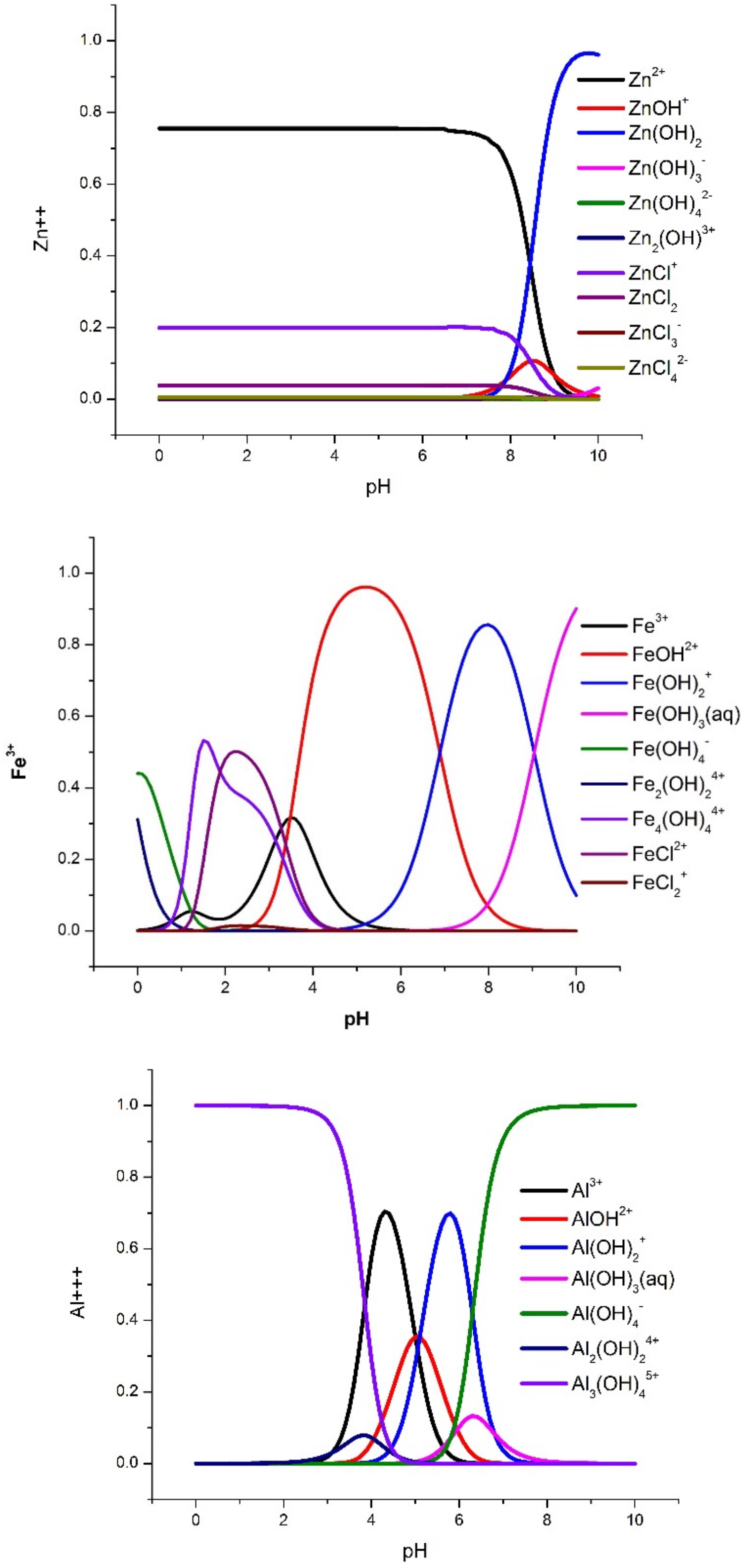

Figure 6.5 Speciation plots of 0.1 M $ZnCl_2$, $AlCl_3$, and $FeCl_3$ solutions.

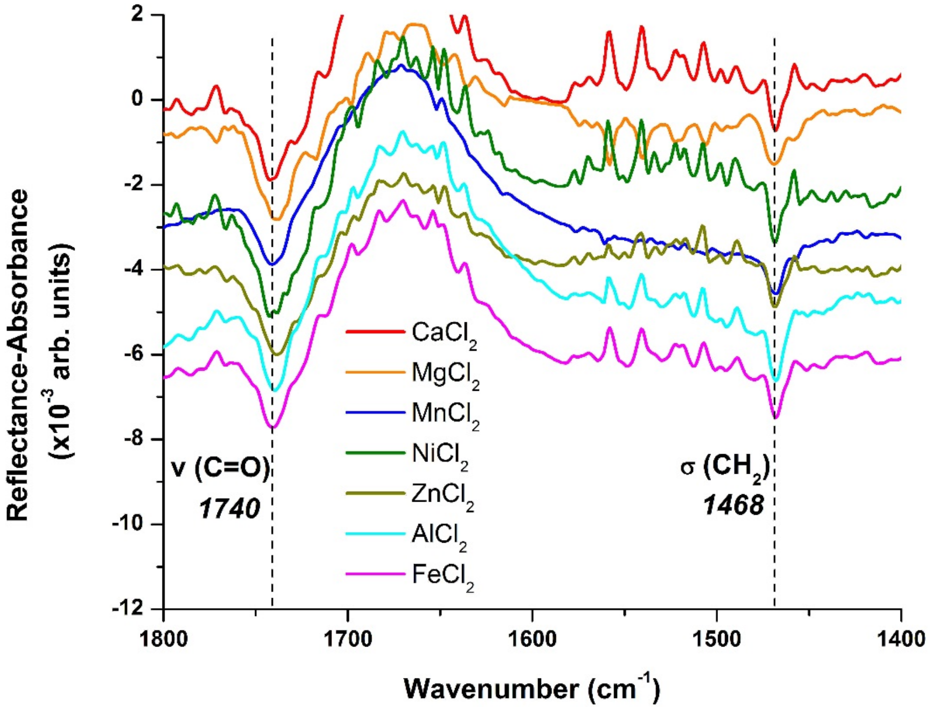

Figure 6.6 IRRAS unprocessed spectra in the C=O and CH_2 scissoring region of DPPA on various 0.1 M salt solutions. Spectra are offset for easy comparison. There is no shift in either peak for any of the salts.

Table 6.1 Calculated K surface adsorption constants for divalent ions.

Ion	**K**	**R^2**
Ca^{2+}	$2.7 \times 10^1 \pm 2.9 \times 10^1$	.95
Mg^{2+}	$9.1 \times 10^1 \pm 9.6 \times 10^1$	.96
Mn^{2+}	$3.2 \times 10^1 \pm 1.6 \times 10^1$	.99
Ni^{2+}	$4.8 \times 10^1 \pm 3.4 \times 10^1$	.98
Zn^{2+}	$6.8 \times 10^2 \pm 1.6 \times 10^2$	.93

Table 6.2 Hydration radii for various metal ions.[42]

Ion	Hydrated Radii	Hydration Shell Size
Ca^{2+}	271	7.2
Mg^{2+}	299	10
Mn^{2+}	286	8.7
Ni^{2+}	302	10.4
Zn^{2+}	295	9.6

Chapter 7. Conclusions & Implications

The work presented in this thesis was motivated by a growing interest in studying the real world complexity of sea spray aerosols (SSA) in the lab through molecular investigations of atmospheric relevant interfaces. DPPA and several other lipids were investigated as models system to explore the impact organics and ions have on SSA. Surface tensiometry was utilized as a direct way of studying the phase behavior and surface organization of these lipids. Through changes in surface tension from monolayer compression and titration, both cation binding and speciation changes to lipids were able to be elucidated. This was further supported by visual imaging via Brewster angle microscopy (BAM), which allowed direct observation of the monolayer characteristics and surface morphology. Finally, infrared reflection-absorption spectroscopy (IRRAS) was utilized to probe the workings of speciation change and ion binding on a molecular level.

For trace metals in the ocean, enrichment at the ocean surface, and subsequent uptake into SSA is thought to be driven by binding to organics. For the studied ocean metal ions Ca^{2+}, Mg^{2+}, Mn^{2+}, Ni^{2+}, Zn^{2+}, Al^{3+}, Fe^{3+} preferential binding for the phosphate headgroup of DPPA was observed over the other functional groups -OH, -COOH, and –$N(CH_3)_2$. This finding suggests that trace metal enrichment is driven primarily by phospholipids, through interactions with their phosphate moieties.

With phosphate binding established as a strong driving force for surface enrichment of metals, the most abundant ocean ions Na^+, K^+, Ca^{2+}, and Mg^{2+} were found to alter the surface behavior differently. K^+ was found to only weakly interact with DPPA, having almost no impact on DPPA monolayers, whereas Na^+, Ca^{2+}, and Mg^{2+} highly ordered and stabilized the monolayers, in the strength $Ca^{2+} > Mg^{2+} > Na^{+}$. The ability of cations to stabilize organic films on the surface of SSA affects aerosol properties such as their ability to reflect light (refractive index), and ability to exchange gas and uptake water (hygroscopicity).[154-155] In the case of the DPPA which forms homogenous monolayers, stabilization of the monolayer would likely inhibit both gas exchange and water uptake. However, DPPA is not the only organic present in SSA, and is only one of several model lipid systems, thus further study of ion interactions with various organics is necessary to understand their full impact.

It was also observed that cation binding was influenced by pH, and more directly, speciation of DPPA. However, the speciation of DPPA was found to be altered at an interface, with DPPA staying protonated at higher pHs than expected. While the first pK_{a1} of DPPA was unable to be elucidated due to the insensitivity of our techniques and the similar behavior of the fully protonated and partially protonated species, the second pK_{a2} was found to be increased by 3 pH units from 8.5 to 11.5 for a condensed monolayer. This was further altered by surface coverage and salts. This has implications for speciation of organics in SSA, as SSA vary in both organic and ion composition depending on particle size, and also vary in size and pH as they uptake both water and gases such as NO_x and SO_x in the atmosphere.[156-161] Thus ongoing and further study is necessary to understand the real world complex of aerosol climate effects in the laboratory.

Finally, the specific issue of ion binding affinity to DPPA was addressed, making for a comprehensive but not yet complete understanding of DPPA interactions in this thesis. The affinity of trace metals to bind to the surface headgroup of DPPA was determined, with the following order of binding strength: $Al^{3+} > Fe^{3+} \sim> Zn^{2+} > Mg^{2+} > Ni^{2+} > Mn^{2+} \sim Ca^{2+}$. This order is different from that observed for bulk binding constants for some inorganic phosphates, as well as other ocean relevant phospholipids.[139] This result shows that the fundamental underpinnings of trace metal enrichment is complex in the real world, and to understand it, further study with more ions and more model systems must be done in the laboratory.

References

1. de Leeuw, G.; Andreas, E. L.; Anguelova, M. D.; Fairall, C. W.; Lewis, E. R.; O'Dowd, C.; Schulz, M.; Schwartz, S. E., Production flux of sea spray aerosol. *Rev. Geophys.* **2011,** *49*.

2. Lohmann, U.; Feichter, J., Global indirect aerosol effects: A review. *Atmos. Chem. Phys.* **2005,** *5*, 715-737.

3. Boucher, O.; Randall, D.; Artaxo, P.; Bretherton, C.; Feingold, G.; Forster, P.; Kerminen, V. M.; Kondo, Y.; Liao, H.; Lohmann, U.; Rasch, P.; Satheesh, S. K.; Sherwood, S.; Stevens, B.; Zhang, Q., Clouds and Aerosols. In *Climate Change 2013: The Physical Science Basis. Contribution of Working Group I to the Fifth Assessment Report of the Intergovernmental Panel on Climate Change*, Stocker, T. F.; Qin, D.; Plattner, G.-K.; Tignor, M.; Allen, S. K.; Boschung, J.; Nauels, A.; Xia, Y.; Bex, V.; Midgley, P. M., Eds. Cambridge University Press: Cambridge, United Kingdom and New York, NY, USA, 2013, 10.1017/CBO9781107415324.016pp 571–658.

4. Carslaw, K. S.; Boucher, O.; Spracklen, D. V.; Mann, G. W.; Rae, J. G. L.; Woodward, S.; Kulmala, M., A review of natural aerosol interactions and feedbacks within the Earth system. *Atmos. Chem. Phys.* **2010,** *10* (4), 1701-1737.

5. Rosenfeld, D.; Sherwood, S.; Wood, R.; Donner, L., Climate effects of aerosol-cloud interactions. *Science* **2014,** *343* (6169), 379-380.

6. Beaver, M. R.; Freedman, M. A.; Hasenkopf, C. A.; Tolbert, M. A., Cooling enhancement of aerosol particles due to surfactant precipitation. *J. Phys. Chem. A* **2010,** *114* (26), 7070-7076.

7. Kanakidou, M.; Seinfeld, J. H.; Pandis, S. N.; Barnes, I.; Dentener, F. J.; Facchini, M. C.; Van Dingenen, R.; Ervens, B.; Nenes, A.; Nielsen, C. J.; Swietlicki, E.; Putaud, J. P.; Balkanski, Y.; Fuzzi, S.; Horth, J.; Moortgat, G. K.; Winterhalter, R.; Myhre, C. E. L.; Tsigaridis, K.; Vignati, E.; Stephanou, E. G.; Wilson, J., Organic aerosol and global climate modelling: a review. *Atmos. Chem. Phys.* **2005,** *5*, 1053-1123.

8. Cochran, R. E.; Jayarathne, T.; Stone, E. A.; Grassian, V. H., Selectivity across the interface: A test of surface activity in the composition of organic-enriched aerosols from bubble bursting. *J. Phys. Chem. Lett.* **2016,** *7* (9), 1692-1696.

9. Jayarathne, T.; Sultana, C. M.; Lee, C.; Malfatti, F.; Cox, J. L.; Pendergraft, M. A.; Moore, K. A.; Azam, F.; Tivanski, A. V.; Cappa, C. D.; Bertram, T. H.; Grassian, V. H.; Prather, K. A.; Stone, E. A., Enrichment of saccharides and divalent cations in sea spray aerosol during two phytoplankton blooms. *Environ. Sci. Technol.* **2016,** *50* (21), 11511-11520.

10. Patterson, J. P.; Collins, D. B.; Michaud, J. M.; Axson, J. L.; Sultana, C. M.; Moser, T.; Dommer, A. C.; Conner, J.; Grassian, V. H.; Stokes, M. D.; Deane, G. B.; Evans, J. E.; Burkart, M. D.; Prather, K. A.; Gianneschi, N. C., Sea spray aerosol structure and composition using cryogenic transmission electron microscopy. *Acs Central Sci* **2016,** *2* (1), 40-47.

11. Wang, X. F.; Deane, G. B.; Moore, K. A.; Ryder, O. S.; Stokes, M. D.; Beall, C. M.; Collins, D. B.; Santander, M. V.; Burrows, S. M.; Sultana, C. M.; Prather, K. A., The

role of jet and film drops in controlling the mixing state of submicron sea spray aerosol particles. *Proc. Natl. Acad. Sci USA* **2017,** *114* (27), 6978-6983.

12. Prather, K. A.; Bertram, T. H.; Grassian, V. H.; Deane, G. B.; Stokes, M. D.; DeMott, P. J.; Aluwihare, L. I.; Palenik, B. P.; Azam, F.; Seinfeld, J. H.; Moffet, R. C.; Molina, M. J.; Cappa, C. D.; Geiger, F. M.; Roberts, G. C.; Russell, L. M.; Ault, A. P.; Baltrusaitis, J.; Collins, D. B.; Corrigan, C. E.; Cuadra-Rodriguez, L. A.; Ebben, C. J.; Forestieri, S. D.; Guasco, T. L.; Hersey, S. P.; Kim, M. J.; Lambert, W. F.; Modini, R. L.; Mui, W.; Pedler, B. E.; Ruppel, M. J.; Ryder, O. S.; Schoepp, N. G.; Sullivan, R. C.; Zhao, D. F., Bringing the ocean into the laboratory to probe the chemical complexity of sea spray aerosol. *Proc. Natl. Acad. Sci USA* **2013,** *110* (19), 7550-7555.

13. Ault, A. P.; Moffet, R. C.; Baltrusaitis, J.; Collins, D. B.; Ruppel, M. J.; Cuadra-Rodriguez, L. A.; Zhao, D. F.; Guasco, T. L.; Ebben, C. J.; Geiger, F. M.; Bertram, T. H.; Prather, K. A.; Grassian, V. H., Size-dependent changes in sea spray aerosol composition and properties with different seawater conditions. *Environ. Sci. Technol.* **2013,** *47* (11), 5603-5612.

14. O'Dowd, C. D.; De Leeuw, G., Marine aerosol production: A review of the current knowledge. *Philos. T. R. Soc. A* **2007,** *365* (1856), 1753-1774.

15. Ovadnevaite, J.; O'Dowd, C.; Dall'Osto, M.; Ceburnis, D.; Worsnop, D. R.; Berresheim, H., Detecting high contributions of primary organic matter to marine aerosol: A case study. *Geophys. Res. Lett.* **2011,** *38*.

16. O'Dowd, C. D.; Facchini, M. C.; Cavalli, F.; Ceburnis, D.; Mircea, M.; Decesari, S.; Fuzzi, S.; Yoon, Y. J.; Putaud, J. P., Biogenically driven organic contribution to marine aerosol. *Nature* **2004,** *431* (7009), 676-680.

17. Losey, D. J.; Parker, R. G.; Freedman, M. A., pH dependence of liquid-liquid phase separation in organic aerosol. *J. Phys. Chem. Lett.* **2016,** *7* (19), 3861-3865.

18. Zhang, T.; Cathcart, M. G.; Vidalis, A. S.; Allen, H. C., Cation effects on phosphatidic acid monolayers at various pH conditions. *Chem. Phys. Lipids* **2016,** *200*, 24-31.

19. Li, S.; Du, L.; Tsona, N. T.; Wang, W., The interaction of trace heavy metal with lipid monolayer in the sea surface microlayer. *Chemosphere* **2018,** *196*, 323-330.

20. Millero, F. J.; Feistel, R.; Wright, D. G.; McDougall, T. J., The composition of standard seawater and the definition of the reference-composition salinity scale. *Deep-Sea Res. Pt 1* **2008,** *55* (1), 50-72.

21. Elliott, S.; Burrows, S. M.; Deal, C.; Liu, X.; Long, M.; Ogunro, O.; Russell, L. M.; Wingenter, O., Prospects for simulating macromolecular surfactant chemistry at the ocean-atmosphere boundary. *Environ. Res. Lett.* **2014,** *9* (6).

22. Burrows, S. M.; Ogunro, O.; Frossard, A. A.; Russell, L. M.; Rasch, P. J.; Elliott, S. M., A physically based framework for modeling the organic fractionation of sea spray aerosol from bubble film Langmuir equilibria. *Atmos. Chem. Phys.* **2014,** *14* (24), 13601-13629.

23. Reeser, D. I.; Kwamena, N. O. A.; Donaldson, D. J., Effect of organic coatings on gas-phase nitrogen dioxide production from aqueous nitrate photolysis. *J. Phys. Chem. C* **2013,** *117* (43), 22260-22267.

24. Andrews, E.; Larson, S. M., Effect of surfactant layers on the size changes of aerosol particles as a function of relative humidity. *Environ. Sci. Technol.* **1993,** *27* (5), 857-865.

25. Clifford, D.; Bartels-Rausch, T.; Donaldson, D. J., Suppression of aqueous surface hydrolysis by monolayers of short chain organic amphiphiles. *Phys. Chem. Chem. Phys.* **2007,** *9* (11), 1362-1369.

26. Glass, S. V.; Park, S. C.; Nathanson, G. M., Evaporation of water and uptake of HCl and HBr through hexanol films at the surface of supercooled sulfuric acid. *J. Phys. Chem. A* **2006,** *110* (24), 7593-7601.

27. Moroi, Y.; Rusdi, M.; Kubo, I., Difference in surface properties between insoluble monolayer and adsorbed film from kinetics of water evaporation and BAM image. *J. Phys. Chem. B* **2004,** *108* (20), 6351-6358.

28. Ciobanu, V. G.; Marcolli, C.; Krieger, U. K.; Weers, U.; Peter, T., Liquid-liquid phase separation in mixed organic/inorganic aerosol particles. *J. Phys. Chem. A* **2009,** *113* (41), 10966-10978.

29. Choi, M. Y.; Chan, C. K., The effects of organic species on the hygroscopic behaviors of inorganic aerosols. *Environ. Sci. Technol.* **2002,** *36* (11), 2422-2428.

30. Bertram, A. K.; Martin, S. T.; Hanna, S. J.; Smith, M. L.; Bodsworth, A.; Chen, Q.; Kuwata, M.; Liu, A.; You, Y.; Zorn, S. R., Predicting the relative humidities of liquid-liquid phase separation, efflorescence, and deliquescence of mixed particles of ammonium sulfate, organic material, and water using the organic-to-sulfate mass ratio of the particle and the oxygen-to-carbon elemental ratio of the organic component. *Atmos. Chem. Phys.* **2011,** *11* (21), 10995-11006.

31. Lin, W.; Clark, A. J.; Paesani, F., Effects of surface pressure on the properties of langmuir monolayers and interfacial water at the air-water interface. *Langmuir* **2015,** *31* (7), 2147-2156.

32. Munnik, T., *Lipid Signaling in Plants*. Springer: Heidelberg ; New York, 2010, p xviii, 330 p.

33. Eaton, J. M.; Takkellapati, S.; Lawrence, R. T.; McQueeney, K. E.; Boroda, S.; Mullins, G. R.; Sherwood, S. G.; Finck, B. N.; Villen, J.; Harris, T. E., Lipin 2 binds phosphatidic acid by the electrostatic hydrogen bond switch mechanism independent of phosphorylation. *J. Biol. Chem.* **2014,** *289* (26), 18055-18066.

34. Kooijman, E. E.; Chupin, V.; de Kruijff, B.; Burger, K. N. J., Modulation of membrane curvature by phosphatidic acid and lysophosphatidic acid. *Traffic* **2003,** *4* (3), 162-174.

35. Kooijman, E. E.; Testerink, C., Phosphatidic acid: an electrostatic/hydrogen-bond switch? *Plant Cell Monogr.* **2010,** *16*, 203-222.

36. Athenstaedt, K.; Daum, G., Phosphatidic acid, a key intermediate in lipid metabolism. *Eur. J. Biochem.* **1999,** *266* (1), 1-16.

37. Wang, X. M.; Devalah, S. P.; Zhang, W. H.; Welti, R., Signaling functions of phosphatidic acid. *Prog. Lipid Res.* **2006,** *45* (3), 250-278.

38. Cochran, R. E.; Laskina, O.; Jayarathne, T.; Laskin, A.; Laskin, J.; Lin, P.; Sultana, C.; Lee, C.; Moore, K. A.; Cappa, C. D.; Bertram, T. H.; Prather, K. A.; Grassian, V. H.;

Stone, E. A., Analysis of Organic Anionic Surfactants in Fine and Coarse Fractions of Freshly Emitted Sea Spray Aerosol. *Environ. Sci. Technol.* **2016,** *50* (5), 2477-2486.

39. Ackman, R. G., *Marine Biogenic Lipids, Fats, and Oils*. CRC Press: Boca Raton, FL., 1989; Vol. I, p 472.

40. Cochran, R. E.; Laskina, O.; Trueblood, J. V.; Estillore, A. D.; Morris, H. S.; Jayarathne, T.; Sultana, C. M.; Lee, C.; Lin, P.; Laskin, J.; Laskin, A.; Dowling, J. A.; Qin, Z.; Cappa, C. D.; Bertram, T. H.; Tivanski, A. V.; Stone, E. A.; Prather, K. A.; Grassian, V. H., Molecular Diversity of Sea Spray Aerosol Particles: Impact of Ocean Biology on Particle Composition and Hygroscopicity. *Chem-Us* **2017,** *2* (5), 655-667.

41. Lee, Y. L.; Lin, J. Y.; Lee, S., Adsorption behavior of glucose oxidase on a dipalmitoylphosphatic acid monolayer and the characteristics of the mixed monolayer at air/liquid interfaces. *Langmuir* **2007,** *23* (4), 2042-2051.

42. Tervahattu, H.; Juhanoja, J.; Kupiainen, K., Identification of an organic coating on marine aerosol particles by TOF-SIMS. *J. Geophys. Res-Atmos.* **2002,** *107* (D16).

43. Marty, J. C.; Saliot, A.; Buatmenard, P.; Chesselet, R.; Hunter, K. A., Relationship between the lipid compositions of marine aerosols, the sea-surface microlayer, and subsurface water. *J. Geophys. Res-Oc Atm.* **1979,** *84* (Nc9), 5707-5716.

44. Frisch, M. J.; Trucks, G. W.; Schlegel, H. B.; Scuseria, G. E.; Robb, M. A.; Cheeseman, J. R.; Scalmani, G.; Barone, V.; Petersson, G. A.; Nakatsuji, H.; Li, X.; Caricato, M.; Marenich, A. V.; Bloino, J.; Janesko, B. G.; Gomperts, R.; Mennucci, B.; Hratchian, H. P.; Ortiz, J. V.; Izmaylov, A. F.; Sonnenberg, J. L.; Williams; Ding, F.; Lipparini, F.; Egidi, F.; Goings, J.; Peng, B.; Petrone, A.; Henderson, T.; Ranasinghe, D.; Zakrzewski, V. G.; Gao, J.; Rega, N.; Zheng, G.; Liang, W.; Hada, M.; Ehara, M.; Toyota, K.; Fukuda, R.; Hasegawa, J.; Ishida, M.; Nakajima, T.; Honda, Y.; Kitao, O.; Nakai, H.; Vreven, T.; Throssell, K.; Montgomery Jr., J. A.; Peralta, J. E.; Ogliaro, F.; Bearpark, M. J.; Heyd, J. J.; Brothers, E. N.; Kudin, K. N.; Staroverov, V. N.; Keith, T. A.; Kobayashi, R.; Normand, J.; Raghavachari, K.; Rendell, A. P.; Burant, J. C.; Iyengar, S. S.; Tomasi, J.; Cossi, M.; Millam, J. M.; Klene, M.; Adamo, C.; Cammi, R.; Ochterski, J. W.; Martin, R. L.; Morokuma, K.; Farkas, O.; Foresman, J. B.; Fox, D. J. *Gaussian 16*, Wallingford, CT, 2016.

45. Lee, C. T.; Yang, W. T.; Parr, R. G., Development of the Colle-Salvetti correlation-energy formula into a functional of the electron density. *Phys. Rev. B* **1988,** *37* (2), 785-789.

46. Becke, A. D., Density-functional thermochemistry.III. The role of exact exchange. *J. Chem. Phys.* **1993,** *98* (7), 5648-5652.

47. Vosko, S. H.; Wilk, L.; Nusair, M., Accurate spin-dependent electron liquid correlation energies for local spin-density calculations - A critical analysis. *Can. J. Phys.* **1980,** *58* (8), 1200-1211.

48. Gaines, G. L., Jr., *Insoluble Monolayers at Liquid-Gas Interface*. Wiley: New York, 1966.

49. Notter, R. H., *Lung Surfactants: Basic Science and Clinical Applications*. Marcel Dekker, Inc.: 2000; Vol. 149.

50. Henon, S.; Meunier, J., Microscope at the Brewster-Angle - Direct Observation of 1st-Order Phase-Transitions in Monolayers. *Rev. Sci. Instrum.* **1991,** *62* (4), 936-939.

51. Hoenig, D.; Moebius, D., Direct visualization of monolayers at the air-water interface by Brewster angle microscopy. *The Journal of Physical Chemistry* **1991,** *95* (12), 4590-4592.

52. Meunier, J., Why a Brewster angle microscope? *Colloids Surf. A* **2000,** *171* (1-3), 33-40.

53. Mendelsohn, R.; Brauner, J. W.; Gericke, A., External infrared reflection-absorption spectrometry of monolayer films at the air-water interface. *Annu Rev Phys Chem* **1995,** *46*, 305-334.

54. Mendelsohn, R.; Mao, G.; Flach, C. R., Infrared reflection–absorption spectroscopy: Principles and applications to lipid–protein interaction in Langmuir films. *Biochimica et Biophysica Acta (BBA) - Biomembranes* **2010,** *1798* (4), 788-800.

55. Goto, T. E.; Caseli, L., Understanding the Collapse Mechanism in Langmuir Monolayers through Polarization Modulation-Infrared Reflection Absorption Spectroscopy. *Langmuir* **2013,** *29* (29), 9063-9071.

56. Flach, C. R.; Gericke, A.; Mendelsohn, R., Quantitative Determination of Molecular Chain Tilt Angles in Monolayer Films at the Air/Water Interface: Infrared Reflection/Absorption Spectroscopy of Behenic Acid Methyl Ester. *The Journal of Physical Chemistry B* **1997,** *101* (1), 58-65.

57. Aroti, A.; Leontidis, E.; Maltseva, E.; Brezesinski, G., Effects of Hofmeister anions on DPPC Langmuir monolayers at the air-water interface. *J. Phys. Chem. B* **2004,** *108* (39), 15238-15245.

58. Mendelsohn, R.; Flach, C. R., Infrared Reflection – Absorption Spectrometry of Monolayer Films at the Air – Water Interface. In *Handbook of Vibrational Spectroscopy*, John Wiley & Sons, Ltd: 2006, 10.1002/0470027320.s2205.

59. Adams, E. M.; Allen, H. C., Palmitic acid on salt subphases and in mixed monolayers of cerebrosides: application to atmospheric aerosol ahemistry. *Atmosphere* **2013,** *4* (4), 315-336.

60. Griffith, E. C.; Adams, E. M.; Allen, H. C.; Vaida, V., Hydrophobic collapse of a stearic acid film by adsorbed L-phenylalanine at the air-water interface. *J. Phys. Chem. B* **2012,** *116* (27), 7849-7857.

61. Barker, D. R.; Zeitlin, H., Metal-ion concentrations in sea-surface microlayer and size-separated atmospheric aerosol samples in Hawaii. *J. Geophys. Res.* **1972,** *77* (27), 5076-+.

62. Boyle, E. A.; Chapnick, S. D.; Bai, X. X.; Spivack, A., Trace metal enrichments in the Mediterranean sea. *Earth Planet Sc Lett* **1985,** *74* (4), 405-419.

63. Buma, A. G. J.; Debaar, H. J. W.; Nolting, R. F.; Vanbennekom, A. J., Metal Enrichment Experiments in the Weddell-Scotia Seas - Effects of Iron and Manganese on Various Plankton Communities. *Limnol. Oceanogr.* **1991,** *36* (8), 1865-1878.

64. Piotrowicz, S. R.; Duce, R. A.; Hoffman, G. L.; Ray, B. J., Trace Metal Enrichment in Sea-Surface Microlayer. *J. Geophys. Res.* **1972,** *77* (27), 5243-+.

65. Kuma, K.; Katsumoto, A.; Kawakami, H.; Takatori, F.; Matsunaga, K., Spatial variability of Fe(III) hydroxide solubility in the water column of the northern North Pacific Ocean. *Deep-Sea Res. Pt 1* **1998,** *45* (1), 91-113.

66. Wang, X. F.; Sultana, C. M.; Trueblood, J.; Hill, T. C. J.; Malfatti, F.; Lee, C.; Laskina, O.; Moore, K. A.; Beall, C. M.; McCluskey, C. S.; Cornwell, G. C.; Zhou, Y. Y.; Cox, J. L.; Pendergraft, M. A.; Santander, M. V.; Bertram, T. H.; Cappa, C. D.; Azam, F.; DeMott, P. J.; Grassian, V. H.; Prather, K. A., Microbial control of sea spray aerosol composition: A tale of two blooms. *Acs Central Sci* **2015,** *1* (3), 124-131.

67. Russell, L. M.; Hawkins, L. N.; Frossard, A. A.; Quinn, P. K.; Bates, T. S., Carbohydrate-like composition of submicron atmospheric particles and their production from ocean bubble bursting. *Proc. Natl. Acad. Sci USA* **2010,** *107* (15), 6652-6657.

68. Hawkins, L. N.; Russell, L., Polysaccharides, proteins, and phytoplankton fragments: Four chemically distinct types of marine primary organic aerosol classified by single particle spectromicroscopy. *Adv. Meteorol.* **2010**, 10.1155/2010/612132.

69. Leck, C.; Bigg, E. K., Biogenic particles in the surface microlayer and overlaying atmosphere in the central Arctic Ocean during summer. *Tellus B* **2005,** *57* (4), 305-316.

70. Aller, J. Y.; Kuznetsova, M. R.; Jahns, C. J.; Kemp, P. F., The sea surface microlayer as a source of viral and bacterial enrichment in marine aerosols. *J Aerosol Sci* **2005,** *36* (5-6), 801-812.

71. Kuznetsova, M.; Lee, C.; Aller, J., Characterization of the proteinaceous matter in marine aerosols. *Mar Chem* **2005,** *96* (3-4), 359-377.

72. Cunliffe, M.; Engel, A.; Frka, S.; Gasparovic, B.; Guitart, C.; Murrell, J. C.; Salter, M.; Stolle, C.; Upstill-Goddard, R.; Wurl, O., Sea surface microlayers: A unified physicochemical and biological perspective of the air-ocean interface. *Prog. Oceanogr.* **2013,** *109*, 104-116.

73. Espinosa, L. F.; Pantoja, S.; Pinto, L. A.; Rullkotter, J., Water column distribution of phospholipid-derived fatty acids of marine microorganisms in the Humboldt Current system off northern Chile. *Deep-Sea Research Part Ii-Topical Studies in Oceanography* **2009,** *56* (16), 1039-1048.

74. Mochida, M.; Kitamori, Y.; Kawamura, K.; Nojiri, Y.; Suzuki, K., Fatty acids in the marine atmosphere: Factors governing their concentrations and evaluation of organic films on sea-salt particles. *J. Geophys. Res-Atmos.* **2002,** *107* (D17).

75. Zhang, T.; Brantley, S. L.; Verreault, D.; Dhankani, R.; S.A., C.; Allen, H. C., Effect of pH and salt on surface-pK_a of phosphatidic acid monolayers. *Langmuir* **2017**, 10.1021/acs.langmuir.7b03579.

76. Pappenheimer, J. R.; Lepie, M. P.; Wyman, J., The surface tension of aqueous solutions of dipolar ions. *J. Am. Chem. Soc.* **1936,** *58*, 1851-1854.

77. Adams, E. M.; Allen, H. C., Palmitic acid on salt subphases and in mixed monolayers of cerebrosides: Application to atmospheric aerosol chemistry. *Atmosphere* **2013,** *4* (4), 315-336.

78. Hermans, J. J.; Keune, K.; van Loon, A.; Iedema, P. D., The crystallization of metal soaps and fatty acids in oil paint model systems. *Phys. Chem. Chem. Phys.* **2016,** *18* (16), 10896-10905.

79. Eva S, L.; Gizela A, L.; Malbaša, R.; Ljiljana A, K., Preparation and characterization of aluminum stearate. *Acta Periodica Technologica* **2003,** *34*, 55-60.

80. Conkright, M. E.; Gregg, W. W.; Levitus, S., Seasonal cycle of phosphate in the open ocean. *Deep-Sea Res. Pt 1* **2000,** *47* (2), 159-175.

81. Nowack, B., Environmental chemistry of phosphonates. *Water Res.* **2003,** *37* (11), 2533-2546.

82. Hua, W.; Verreault, D.; Adams, E. M.; Huang, Z. S.; Allen, H. C., Impact of salt purity on interfacial water organization revealed by conventional and heterodyne-detected vibrational sum frequency generation spectroscopy. *J. Phys. Chem. C* **2013,** *117* (38), 19577-19585.

83. Finlayson, A. C., The pH range of the Mohr titration for chloride-ion can be usefully extended to 4-10.5. *J. Chem. Educ.* **1992,** *69* (7), 559.

84. Jacobson, K.; Papahadjopoulos, D., Phase-Transitions and Phase Separations in Phospholipid Membranes Induced by Changes in Temperature, Ph, and Concentration of Bivalent-Cations. *Biochemistry* **1975,** *14* (1), 152-161.

85. Rudolphi-Skórska, E.; Zembala, M.; Filek, M., Mechanical and electrokinetic effects of polyamines/phospholipid interactions in model membranes. *J. Membrane Biol.* **2014,** *247* (1), 81-92.

86. Grigoriev, D.; Miller, R.; Wüstneck, R.; Wüstneck, N.; Pison, U.; Möhwald, H., A novel method to evaluate the phase transition thermodynamics of Langmuir monolayers. Application to DPPG monolayers affected by subphase composition. *J. Phys. Chem. B* **2003,** *107* (51), 14283-14288.

87. Yun, H.; Choi, Y. W.; Kim, N. J.; Sohn, D., Physicochemical properties of phosphatidylcholine (PC) monolayers with different alkyl chains, at the air/water interface. *B. Korean Chem. Soc.* **2003,** *24* (3), 377-383.

88. de Meijere, K.; Brezesinski, G.; Möhwald, H., Polyelectrolyte coupling to a charged lipid monolayer. *Macromolecules* **1997,** *30* (8), 2337-2342.

89. Boggs, J. M., Effect of lipid structural modifications on their intermolecular hydrogen-bonding interactions and membrane functions. *Biochem. Cell. Biol.* **1986,** *64* (1), 50-57.

90. Vega Mercado, F.; Maggio, B.; Wilke, N., Phase diagram of mixed monolayers of stearic acid and dimyristoylphosphatidylcholine. Effect of the acid ionization. *Chem. Phys. Lipids* **2011,** *164* (5), 386-392.

91. Wang, W. J.; Anderson, N. A.; Travesset, A.; Vaknin, D., Regulation of the electric charge in phosphatidic acid domains. *J. Phys. Chem. B* **2012,** *116* (34), 10406-10406.

92. Abramson, M. B.; Wilson, C. E.; Gregor, H. P.; Katzman, R., Ionic properties of aqueous dispersions of phosphatidic acid. *J. Biol. Chem.* **1964,** *239* (12), 4066-4072.

93. Patil, G. S.; Dorman, N. J.; Cornwell, D. G., Effects of ionization and counterion binding on the surface areas of phosphatidic acids in monolayers. *J. Lipid Res.* **1979,** *20* (5), 663-668.

94. Miñones Jr., J.; Patino, R.; Miñones, J. M.; Dynarowicz-Latka, P.; Carrera, C., Structural and topographical characteristics of dipalmitoyl phosphatidic acid in Langmuir monolayers. *J. Colloid Interface Sci.* **2002,** *249* (2), 388-397.

95. Dynarowicz-Łatka, P.; Kita, K., Molecular interaction in mixed monolayers at the air/water interface. *Adv. Colloid Interface* **1999,** *79* (1), 1-17.

96. Griffith, E. C.; Vaida, V., Ionization state of L-phenylalanine at the air-water interface. *J. Am. Chem. Soc.* **2013,** *135* (2), 710-716.

97. Kanicky, J. R.; Poniatowski, A. F.; Mehta, N. R.; Shah, D. O., Cooperativity among molecules at interfaces in relation to various technological processes: Effect of chain length on the pKa of fatty acid salt solutions. *Langmuir* **2000,** *16* (1), 172-177.

98. Kanicky, J. R.; Shah, D. O., Effect of degree, type, and position of unsaturation on the pKa of long-chain fatty acids. *J. Colloid Interface Sci.* **2002,** *256* (1), 201-207.

99. Kanicky, J. R.; Shah, D. O., Effect of premicellar aggregation on the pKa of fatty acid soap solutions. *Langmuir* **2003,** *19* (6), 2034-2038.

100. Tang, C. Y.; Huang, Z. S. A.; Allen, H. C., Binding of Mg^{2+} and Ca^{2+} to palmitic acid and deprotonation of the COOH headgroup studied by vibrational sum frequency generation spectroscopy. *J. Phys. Chem. B* **2010,** *114* (51), 17068-17076.

101. Vácha, R.; Siu, S. W. I.; Petrov, M.; Böckmann, R. A.; Barucha-Kraszewska, J.; Jurkiewicz, P.; Hof, M.; Berkowitz, M. L.; Jungwirth, P., Effects of alkali cations and halide anions on the DOPC lipid membrane. *J. Phys. Chem. A* **2009,** *113* (26), 7235-7243.

102. Vaz, W. L. C.; Nicksch, A.; Jahnig, F., Electrostatic interactions at charged lipid-membranes - measurement of surface pH with fluorescent lipid pH indicators. *Eur. J. Biochem.* **1978,** *83* (1), 299-305.

103. Tang, C. Y.; Allen, H. C., Ionic binding of Na^+ versus K^+ to the carboxylic acid headgroup of palmitic acid monolayers studied by vibrational sum frequency generation spectroscopy. *J. Phys. Chem. A* **2009,** *113* (26), 7383-7393.

104. Tang, C. Y.; Huang, Z. S.; Allen, H. C., Interfacial water structure and effects of Mg^{2+} and Ca^{2+} binding to the COOH headgroup of a palmitic acid monolayer studied by sum frequency spectroscopy. *J. Phys. Chem. B* **2011,** *115* (1), 34-40.

105. Casillas-Ituarte, N. N.; Chen, X. K.; Castada, H.; Allen, H. C., Na^+ and Ca^{2+} effect on the hydration and orientation of the phosphate group of DPPC at air-water and air-hydrated silica interfaces. *J. Phys. Chem. B* **2010,** *114* (29), 9485-9495.

106. Marcus, Y., Thermodynamics of solvation of ions. Part 5.-Gibbs free energy of hydration at 298.15 K. *J. Chem. Soc. Faraday T.* **1991,** *87* (18), 2995-2999.

107. Collins, K. D., Charge density-dependent strength of hydration and biological structure. *Biophys. J.* **1997,** *72* (1), 65-76.

108. Cordomí, A.; Edholm, O.; Perez, J. J., Effect of force field parameters on sodium and potassium ion binding to dipalmitoyl phosphatidylcholine bilayers. *J. Chem. Theory Comput.* **2009,** *5* (8), 2125-2134.

109. Gurtovenko, A. A.; Vattulainen, I., Effect of NaCl and KCl on phosphatidylcholine and phosphatidylethanolamine lipid membranes: Insight from atomic-scale simulations for understanding salt-induced effects in the plasma membrane. *J. Phys. Chem. B* **2008,** *112* (7), 1953-1962.

110. Böckmann, R. A.; Hac, A.; Heimburg, T.; Grübmuller, H., Effect of sodium chloride on a lipid bilayer. *Biophys. J.* **2003,** *85* (3), 1647-1655.

111. Mukhopadhyay, P.; Monticelli, L.; Tieleman, D. P., Molecular dynamics simulation of a palmitoyl-oleoyl phosphatidylserine bilayer with Na^+ counterions and NaCl. *Biophys. J.* **2004,** *86* (3), 1601-1609.

112. Giner Casares, J. J.; Camacho, L.; Martín-Romero, M. T.; Cascales, J. J. L., Effect of Na^+ and Ca^{2+} ions on a lipid Langmuir monolayer: an atomistic description by molecular dynamics simulations. *ChemPhysChem* **2008,** *9* (17), 2538-2543.

113. Bu, W.; Flores, K.; Pleasants, J.; Vaknin, D., Preferential affinity of calcium ions to charged phosphatidic acid surface from a mixed calcium/barium solution: X-ray reflectivity and fluorescence studies. *Langmuir* **2009,** *25* (2), 1068-1073.
114. Faraudo, J.; Travesset, A., Phosphatidic acid domains in membranes: Effect of divalent counterions. *Biophys. J.* **2007,** *92* (8), 2806-2818.
115. Phoeung, T.; Aubron, P.; Rydzek, G.; Lafleur, M., pH-triggered release from nonphospholipid LUVs modulated by the pKa of the included fatty acid. *Langmuir* **2010,** *26* (15), 12769-12776.
116. Maltseva, E.; Shapovalov, V. L.; Möhwald, H.; Brezesinski, G., Ionization state and structure of L-1,2-dipalmitoylphosphatidylglycerol monolayers at the liquid/air interface. *J. Phys. Chem. B* **2006,** *110* (2), 919-926.
117. Lahdesmaki, K.; Ollila, O. H. S.; Koivuniemi, A.; Kovanen, P. T.; Hyvonen, M. T., Membrane simulations mimicking acidic pH reveal increased thickness and negative curvature in a bilayer consisting of lysophosphatidylcholines and free fatty acids. *Biochim. Biophys. Acta Biomembranes* **2010,** *1798* (5), 938-946.
118. Teixeira, V. H.; Vila-Vicosa, D.; Baptista, A. M.; Machuqueiro, M., Protonation of DMPC in a Bilayer Environment Using a Linear Response Approximation. *J. Chem. Theory Comput.* **2014,** *10* (5), 2176-2184.
119. Strazdaite, S.; Meister, K.; Bakker, H. J., Reduced acid dissociation of amino-acids at the surface of water. *J. Am. Chem. Soc.* **2017,** *139* (10), 3716-3720.
120. Rao, Y.; Subir, M.; McArthur, E. A.; Turro, N. J.; Eisenthal, K. B., Organic ions at the air/water interface. *Chem. Phys. Lett.* **2009,** *477* (4-6), 241-244.
121. Fears, K. P.; Creager, S. E.; Latour, R. A., Determination of the surface pK of carboxylic- and amine-terminated alkanethiols using surface plasmon resonance spectroscopy. *Langmuir* **2008,** *24* (3), 837-843.
122. Wellen, B. A.; Lach, E. A.; Allen, H. C., Surface pKa of Octanoic, Nonanoic, and Decanoic Fatty Acids at the Air-Water Interface: Applications to Atmospheric Aerosol Chemistry. *Phys. Chem. Chem. Phys.* **2017,** *19* (39), 26551-26558.
123. Fridlind, A. M.; Jacobson, M. Z., A study of gas-aerosol equilibrium and aerosol pH in the remote marine boundary layer during the First Aerosol Characterization Experiment (ACE 1). *J. Geophys. Res-Atmos.* **2000,** *105* (D13), 17325-17340.
124. Guo, H.; Xu, L.; Bougiatioti, A.; Cerully, K. M.; Capps, S. L.; Hite, J. R.; Carlton, A. G.; Lee, S. H.; Bergin, M. H.; Ng, N. L.; Nenes, A.; Weber, R. J., Fine-particle water and pH in the southeastern United States. *Atmos. Chem. Phys.* **2015,** *15* (9), 5211-5228.
125. Ariga, K.; Nakanishi, T.; Hill, J. P.; Shirai, M.; Okuno, M.; Abe, T.; Kikuchi, J., Tunable pKa of amino acid residues at the air-water interface gives an L-zyme (Langmuir enzyme). *J. Am. Chem. Soc.* **2005,** *127* (34), 12074-12080.
126. Micheau, C.; Bauduin, P.; Diat, O.; Faure, S., Specific salt and pH effects on foam film of a pH sensitive surfactant. *Langmuir* **2013,** *29* (27), 8472-8481.
127. Kooijman, E. E.; Carter, K. M.; van Laar, E. G.; Chupin, V.; Burger, K. N. J.; de Kruijff, B., What makes the bioactive lipids phosphatidic acid and lysophosphatidic acid so special? *Biochemistry* **2005,** *44* (51), 17007-17015.

128. Tocanne, J. F.; Teissié, J., Ionization of phospholipids and phospholipid-supported interfacial lateral diffusion of protons in membrane model systems. *Biochim. Biophys. Acta* **1990,** *1031* (1), 111-142.

129. Zhao, X. L.; Ong, S. W.; Wang, H. F.; Eisenthal, K. B., New method for determination of surface pKa using 2nd-harmonic generation. *Chem. Phys. Lett.* **1993,** *214* (2), 203-207.

130. Sandoval, G., *Lipases and Phospholipases: Methods and Protocols*. Humana Press: New York, 2012.

131. Laroche, G.; Dufourc, E. J.; Dufourcq, J.; Pézolet, M., Structure and dynamics of dimyristoylphosphatidic acid calcium complexes by 2H-NMR, infrared, and Raman spectroscopies and small-angle x-ray-diffraction. *Biochemistry* **1991,** *30* (12), 3105-3114.

132. Binder, H.; Zschörnig, O., The effect of metal cations on the phase behavior and hydration characteristics of phospholipid membranes. *Chem. Phys. Lipids* **2002,** *115* (1-2), 39-61.

133. Israelachvili, J. N., *Intermolecular and Surface Forces*. 3rd ed.; Academic Press: Burlington, MA, 2011.

134. Mclaughlin, S., The electrostatic properties of membranes. *Annu. Rev. Biophys. Biophys. Chem,* **1989,** *18*, 113-136.

135. IAPWS *Revised Supplementary Release on Properties of Liquid Water at 0.1 MPa*; http://www.iapws.org/, 2011.

136. Marcus, Y., Evaluation of the static permittivity of aqueous electrolytes. *J. Solution Chem.* **2013,** *42* (12), 2354-2363.

137. Travesset, A.; Vaknin, D., Bjerrum pairing correlations at charged interfaces. *Europhys. Lett.* **2006,** *74* (1), 181-187.

138. Gambinossi, F.; Mecheri, B.; Caminati, G.; Nocentini, M.; Puggelli, M.; Gabrielli, G., Antibiotic interaction with phospholipid monolayers. *Mat. Sci. Eng. C-Bio. S.* **2002,** *22* (2), 283-288.

139. Adams, E. M.; Verreault, D.; Jayarathne, T.; Cochran, R. E.; Stone, E. A.; Allen, H. C., Surface organization of a DPPC monolayer on concentrated SrCl2 and ZnCl2 solutions. *Phys. Chem. Chem. Phys.* **2016,** *18* (47), 32345-32357.

140. Barnes, G.; Gentle, I., *Interfacial science : an introduction*. 2nd ed.; Oxford University Press: Oxford ; New York, 2011, p xxii, 325 p.

141. Meissner, H. P.; Michaels, A. S., Surface tensions of pure liquids and liquid mixtures. *Ind Eng Chem* **1949,** *41* (12), 2782-2787.

142. Wolhoff, J. A.; Overbeek, J. T. G., Determination of equilibrium constants for a number of metal-phosphate complexes. *Recl Trav Chim Pay B* **1959,** *78* (9-10), 759-782.

143. Van Wazer, J. R.; Callis, C. F., Metal complexing by phosphates. *Chem. Rev.* **1958,** *58* (6), 1011-1046.

144. Van Wazer, J. R.; Campanella, D. A., Structure and properties of the condensed phosphates. 4. Complex ion formation in polyphosphate solutions. *J. Am. Chem. Soc.* **1950,** *72* (2), 655-663.

145. Popov, K.; Ronkkomaki, H.; Lajunen, L. H. J., Critical evaluation of stability constants of phosphonic acids (IUPAC technical report). *Pure Appl Chem* **2001,** *73* (10), 1641-1677.

146. Marcus, Y., A simple empirical-model describing the thermodynamics of hydration of ions of widely varying charges, sizes, and shapes. *Biophys. Chem.* **1994,** *51* (2-3), 111-127.

147. Adams, E. M.; Casper, C. B.; Allen, H. C., Effect of cation enrichment on dipalmitoylphosphatidylcholine (DPPC) monolayers at the air-water interface. *J. Colloid Interface Sci.* **2016,** *478*, 353-364.

148. Frieden, E., *Biochemistry of the essential ultratrace elements*. Plenum: New York, 1984, p xviii, 426 p.

149. Krezel, A.; Maret, W., The biological inorganic chemistry of zinc ions. *Arch Biochem Biophys* **2016,** *611*, 3-19.

150. Franks, F., *Aqueous solutions of simple electrolytes*. Plenum Press: New York,, 1973, p xvii, 472 p.

151. Wesseling Perry, K.; Salusky, I. B., Chapter 70 - Chronic kidney disease mineral and bone disorder. In *Endocrinology: Adult and Pediatric (Seventh Edition)*, Groot, L. J. D.; Kretser, D. M. d.; Giudice, L. C.; Grossman, A. B.; Melmed, S.; Potts, J. T.; Weir, G. C., Eds. W.B. Saunders: Philadelphia, 2016, https://doi.org/10.1016/B978-0-323-18907-1.00070-6pp 1214-1229.e6.

152. Kennedy, E. J., Biological drug products: development and strategies. *ChemMedChem* **2014,** *9* (12), 2814-2815.

153. Barber, T. M. Phosphate adsorption by mixed and reduced iron phases in static and dynamic systems. Stanford University, Stanford, CA, 2002.

154. Bertram, T. H.; Cochran, R. E.; Grassian, V. H.; Stone, E. A., Sea spray aerosol chemical composition: elemental and molecular mimics for laboratory studies of heterogeneous and multiphase reactions. *Chemical Society Reviews* **2018**, 10.1039/C7CS00008A.

155. Pham, D. Q.; O'Brien, R.; Fraund, M.; Bonanno, D.; Laskina, O.; Beall, C.; Moore, K. A.; Forestieri, S.; Wang, X.; Lee, C.; Sultana, C.; Grassian, V.; Cappa, C. D.; Prather, K. A.; Moffet, R. C., Biological Impacts on Carbon Speciation and Morphology of Sea Spray Aerosol. *ACS Earth and Space Chemistry* **2017,** *1* (9), 551-561.

156. Estillore, A. D.; Morris, H. S.; Or, V. W.; Lee, H. D.; Alves, M. R.; Marciano, M. A.; Laskina, O.; Qin, Z.; Tivanski, A. V.; Grassian, V. H., Linking hygroscopicity and the surface microstructure of model inorganic salts, simple and complex carbohydrates, and authentic sea spray aerosol particles. *Phys. Chem. Chem. Phys.* **2017,** *19* (31), 21101-21111.

157. Shaloski, M. A.; Sobyra, T. B.; Nathanson, G. M., DCl Transport through Dodecyl Sulfate Films on Salty Glycerol: Effects of Seawater Ions on Gas Entry. *The Journal of Physical Chemistry A* **2015,** *119* (50), 12357-12366.

158. Cosman, L. M.; Knopf, D. A.; Bertram, A. K., N2O5 Reactive Uptake on Aqueous Sulfuric Acid Solutions Coated with Branched and Straight-Chain Insoluble Organic Surfactants. *The Journal of Physical Chemistry A* **2008,** *112* (11), 2386-2396.

159. Chang, W. L.; Bhave, P. V.; Brown, S. S.; Riemer, N.; Stutz, J.; Dabdub, D., Heterogeneous Atmospheric Chemistry, Ambient Measurements, and Model Calculations of N2O5: A Review. *Aerosol Science and Technology* **2011,** *45* (6), 665-695.

160. Ault, A. P.; Guasco, T. L.; Ryder, O. S.; Baltrusaitis, J.; Cuadra-Rodriguez, L. A.; Collins, D. B.; Ruppel, M. J.; Bertram, T. H.; Prather, K. A.; Grassian, V. H., Inside versus Outside: Ion Redistribution in Nitric Acid Reacted Sea Spray Aerosol Particles as Determined by Single Particle Analysis. *J. Am. Chem. Soc.* **2013,** *135* (39), 14528-14531.

161. Keene, W. C.; Maring, H.; Maben, J. R.; Kieber, D. J.; Pszenny, A. A. P.; Dahl, E. E.; Izaguirre, M. A.; Davis, A. J.; Long, M. S.; Zhou, X.; Smoydzin, L.; Sander, R., Chemical and physical characteristics of nascent aerosols produced by bursting bubbles at a model air-sea interface. *Journal of Geophysical Research: Atmospheres* **2007,** *112* (D21), n/a-n/a.

162. Huang, Z. S.; Hua, W.; Verreault, D.; Allen, H. C., Influence of Salt Purity on Na+ and Palmitic Acid Interactions. *J. Phys. Chem. A* **2013,** *117* (50), 13412-13418.

163. Morgan, H.; Taylor, D. M.; Oliveira, O. N., Lateral Conduction at a Monolayer Water Interface. *Thin Solid Films* **1989,** *178*, 73-79.

164. Lukes, P. J.; Petty, M. C.; Yarwood, J., An Infrared Study of the Incorporation of Ion Channel Forming Peptides into Langmuir-Blodgett-Films of Phosphatidic-Acid. *Langmuir* **1992,** *8* (12), 3043-3050.

165. Ahuja, R. C.; Caruso, P. L.; Mobius, D.; Wildburg, G.; Ringsdorf, H.; Philp, D.; Preece, J. A.; Stoddart, J. F., Molecular-organization via ionic interactions at interfaces .1. Monolayers and LB films of cyclic bisbipyridinium tetracations and dimyristoylphosphatidic acid. *Langmuir* **1993,** *9* (6), 1534-1544.

166. Zaitsev, S. Y.; Zubov, V. P.; Mobius, D., Mixed Monolayers of Valinomycin and Dipalmitoylphosphatidic Acid. *Colloids Surf. A* **1995,** *94* (1), 75-83.

167. Kasselouri, A.; Coleman, A. W.; Baszkin, A., Mixed monolayers of amphiphilic cyclodextrins and phospholipids .1. Miscibility under dynamic conditions of compression. *J. Colloid Interface Sci.* **1996,** *180* (2), 384-397.

168. Pemberton, J. E.; Chamberlain, J. R., Raman spectroscopy of model membrane monolayers of dipalmitoylphosphatidic acid at the air-water interface using surface enhancement from buoyant thin silver films. *Biopolymers* **2000,** *57* (2), 103-116.

169. Lee, Y. L.; Lin, J. Y.; Chang, C. H., Thermodynamic characteristics and Langmuir-Blodgett deposition behavior of mixed DPPA/DPPC monolayers at air/liquid interfaces. *J. Colloid Interface Sci.* **2006,** *296* (2), 647-654.

170. McNamee, C. E.; Kappl, M.; Butt, H. J.; Ally, J.; Shigenobu, H.; Iwafuji, Y.; Higashitani, K.; Graf, K., Forces between a monolayer at an air/water interface and a particle in solution: influence of the sign of the surface charges and the subphase salt concentration. *Soft Matter* **2011,** *7* (21), 10182-10192.

171. Risović, D.; Frka, S.; Kozarac, Z., The Structure of Percolating Lipid Monolayers. *J. Colloid Interface Sci.* **2012,** *373*, 116-121.

172. Salay, L. C.; Ferreira, M.; Oliveira, O. N.; Nakaie, C. R.; Schreier, S., Headgroup specificity for the interaction of the antimicrobial peptide tritrpticin with phospholipid Langmuir monolayers. *Colloids Surf. B* **2012,** *100*, 95-102.

Appendix A: Salts and solutions cleanliness

The emphasis on salts and solutions treatment for the removal of organic contaminants was necessary due to the variability regarding the Π–A isotherms of DPPA on water published in the literature. While the phase behavior of DPPA has been well documented, reported MMA values at lift-off, at the TC-UC transition point, as well as at the onset of collapse vary somewhat between sources (Table A.1). Besides different experimental conditions (pH, temperature, spreading solvent, etc.; see Table A.2), other potential sources of variations can include, for example, materials (DPPA, salts, water) purity, incomplete DPPA dissolution, and cleanliness of the experimental procedure, in particular, removal of organic contaminants. The effect of removing residual contaminants is significant, improving reproducibility and determination of the true lift-off area. Previous studies by Allen et al. showed that only ultra-high purity grade salts exhibit insignificant concentrations of impurities without filtration for surface studies [82, 162]. We follow the same procedures to successfully remove impurities. Baking at high temperatures and filtration was adequate for the removal of organic contaminants. The possibility of divalent contamination in monovalent salts was also addressed; for the ACS grade salts, maximum Ca^{2+} and Mg^{2+} concentrations in NaCl and KCl salts were reported to be less than 0.002 and 0.001%, respectively. In addition, trace metal grade HCl and NaOH were used for adjusting the pH of solutions. The presence of contaminants in lower grades of acid/bases can also be a source of discrepancies in isotherms.

Table A.1 List of published values of characteristic mean molecular areas at lift-off ($\mathrm{A_{lo}}$), TC-UC transition ($\mathrm{A_t}$), and at the onset of collapse ($\mathrm{A_c}$) from compression isotherms of DPPA monolayers on water. Values given in parentheses are estimated from the published data. Average values and standard deviations are boldfaced.

pH_b	T (K)	A_{lo} (Å^2)	A_{t} (Å^2)	A_{c} (Å^2)	Ref
5.6	n/a	(48)	(41)	(39)	[163]
7	291	(46)	n/a	42 ± 2	[164]
5.6	294	(47)	(45)	(42)	[165]
n/a	291	(45)	(41)	40	[166]
5.5	296	(42)	(38)	(37)	[167]
n/a	293	(45.5)	(42.5)	(40)	[88]
n/a	n/a	55	44	42	[168]
5.6	293	(47)	(44)	(40)	[138]
6	293	52	41	(40)	[94]
n/a	298	50	(45)	(39)	[169]
n/a	298	56	52	(48)	[41]
n/a	293	(48)	(42)	(40)	[170]
n/a	296	(62)	(52)	(40)	[171]
5.5−6.0	295	(45)	(43)	(40)	[172]
		49.2 ± 5.4	**43.9 ± 4.1**	**40.6 ± 2.5**	
5−6	294	47.5	43.5	42	this

Table A.2 Comparison of experimental conditions for compression isotherms of DPPA monolayers on water obtained in this work and published in literature.

Source (Purity (%))	*T* (K)[I]	Compression rate[II]	Method[III]	Spreading solvent[IV]	Water subphase (Resistivity (MΩ·cm))[V]	pH_b	Ref
Koch Light	293	n/a	LW	Chl:Met (4:1, v/v)	MQ	5.6	[163]
Sigma	291	0.1 AMM	LW?	Chl	n/a	7[a]	[164]
Sigma	294	n/a	FW	Chl or Chl:Met(?)	MQ	5.6	[165]
Fluka	291	20 CMM	LW	Chl	n/a	n/a	[166]
Fluka (99)	296	7 MMM	LW	Chl	DD	5.5	[167]
Avanti Polar	n/a	25 CMM	LW?	Chl	MQ (18.2)	n/a	[168]
Sigma (>99)	293	8 AMM	LW	Chl	MQ (18.2)	5.6	[138]
Sigma (99)	288,	8.5 AMM	LW	Chl:Met (4:1, v/v)	MQ (18)	6	[94]
Avanti Polar	298	4.6 AMM	LW	Chl:Met (9:1, v/v)	MQ (18.2)	n/a	[169]
Avanti Polar	298	4.6 AMM	LW	Chl:Met (9:1, v/v)	MQ (18.2)	n/a	[41]
Fluka (≥98)	293	67.8 AMM	LW	Chl:Met (9:1, v/v)	MQ (18.2)	n/a	[170]
Sigma	296	~0.6 NMM	FW	n/a	n/a	n/a	[171]
Avanti Polar	295	10 MMM	LW	Chl	MQ	5.5−	[172]
Avanti Polar	294	5 MMM	LW	Chl:Met (7:3, v/v)	MQ (18.2)	5−6	this

Abbreviations used:

[I] Temperature: RT, room temperature.

[II] Compression rate: AMM, Å^2/molecule·min; CMM, cm^2/min; MMM, mm/min; NMM, nm^2/molecule.

[III] Method: FW, Fromherz trough/Wilhelmy balance; LW, Langmuir trough/Wilhelmy balance.

[IV] Spreading solvent: Chl, chloroform; Met, methanol.

[V] Water subphase: D, distilled; DD, doubly distilled; MQ, Milli-Q.

[a] Unbuffered.

Appendix B: Calibration of DPPA Concentrations via IR for a Standardized Isotherm

Initial isotherms with prepared DPPA solutions observed a liftoff area of ~37 Å^2, with a molecular footprint of 35 Å^2. In the initial review stages of the paper "Cation effects on phosphatidic acid monolayers at various pH conditions", reviewers took issue with the improbability of the value, given that the minimum footprint area of single upright acyl chain is 20 Å^2, in agreement with isotherms observed of C_{16} palmitic acid.[77] Thus for DPPA with two acyl chains, the minimum molecular footprint possible would be 40 Å^2, yet initial isotherms reported a footprint area of 35 Å^2.

Calibration of DPPA solution concentration to determine a correct isotherm liftoff MMA was necessary due to imprecise mass measurements and evaporation of the volatile chloroform solvent. Due to the low solubility of DPPA, only low concentrations ~1 mM could be prepared (higher concentrations resulted in unstable solutions that eventually turned cloudiness and precipitation). Such low concentrations required low sample masses ~10 mg, which was near the limit of the analytical balance which was only displayed 4 decimal places, with the 4th decimal place subject to uncertainty error. In addition, the chloroform-methanol solvent is highly volatile, evaporating even during solution preparation.

To overcome these issues, another lipid, DPPC was chosen as a standard as it is nearly identical to DPPA but is commercially available at a known concentration. 1.0 mg/mL stock solution in a sealed glass ampule was purchased from Avanti Polar Lipids (Alabaster, AL) and used to make a set of 4 reference standards. IR spectra of DPPC in a liquid flow cell are plotted in the C=O region in Figure B.1. DPPC and DPPA share the same carbonyl structure, so the dependence of peak area of the C=O stretch at ~1740 cm^{-1} on concentration is the same for both molecules. The C=O peaks in Figure B.1 are background subtracted with a horizontal baseline between the two vertical lines. The peak areas are plotted with a linear calibration fit in Figure B.2 (black data points). IR liquid flow cell spectra of DPPA solutions at two different concentrations were taken and their C=O peak area fits also plotted in the same figure (blue data points). All calibration and measurement IR spectra were taken within one hour due to solvent volatility.

The corresponding concentrations of the two DPPA solutions calculated from the plot were compared by running surface pressure compression isotherms with both in good agreement of a liftoff area of ~47.5 Å^2, and a footprint area of 45 Å^2. This footprint size of 45 Å^2 is a more reasonable area for a double acyl chain phospholipid, and thus is set as the correct standardized DPPA isotherm.

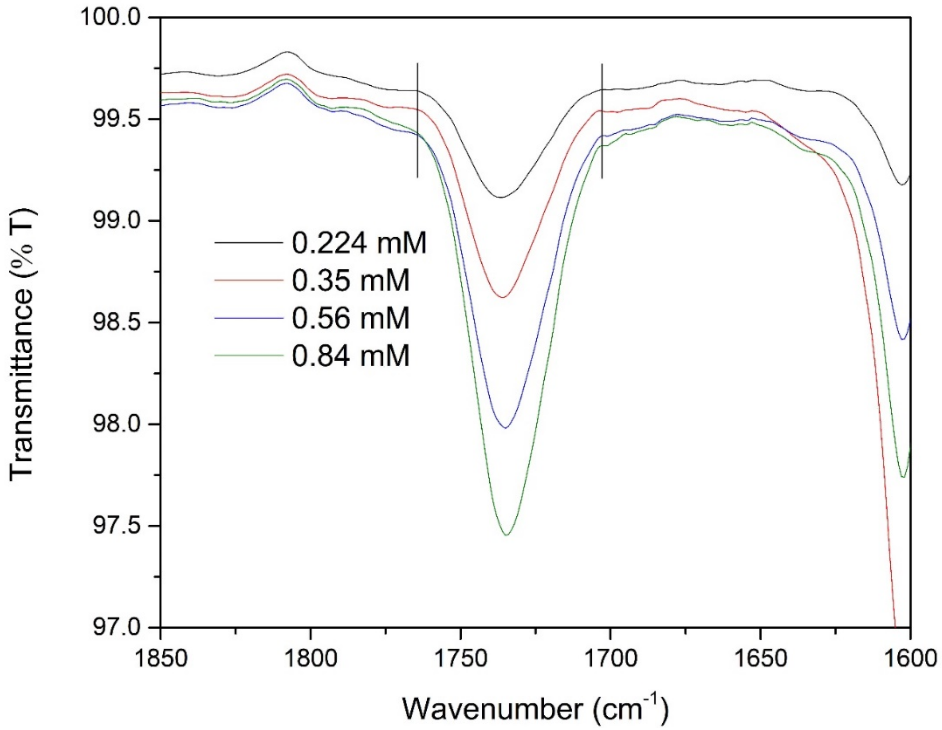

Figure B.1 IR Spectra of DPPC reference standard solutions in the carbonyl region. The two vertical lines indicate where the horizontal baseline begins and ends.

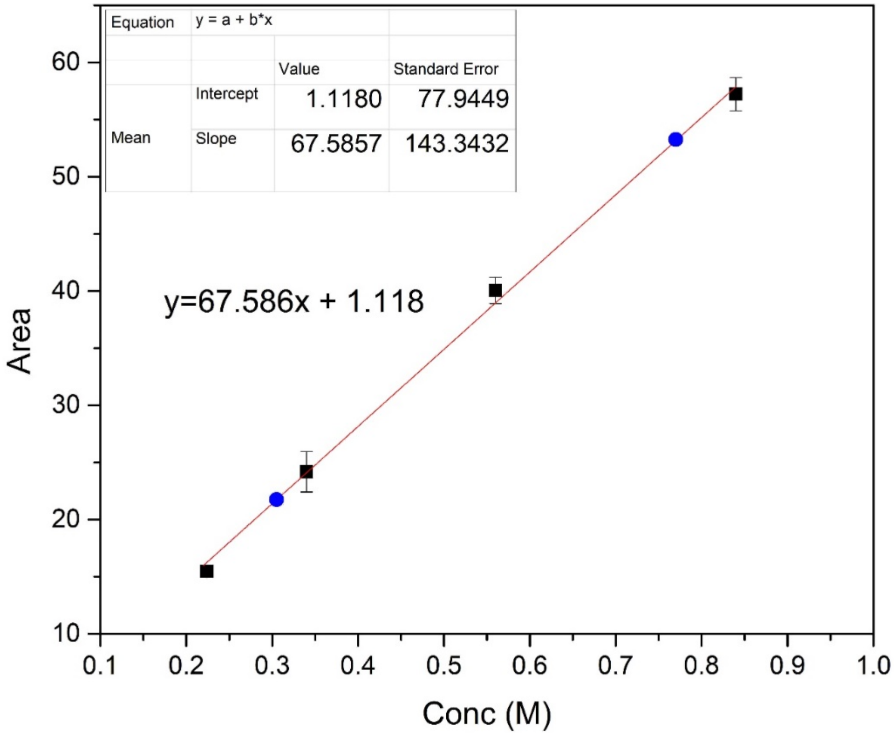

Figure B.2 Plotted peak areas of the C=O mode from Fig D.1. Square data points are DPPC solutions, blue circle data points DPPA solutions. Both solutions gave identical isotherms verifying the validity of the calibration curve.

Figure B.3 IR liquid cell in sample compartment chamber of FTIR spectrometer.

Appendix C: IRRAS Optimization and Spectra Processing

The quality of IRRAS spectra is extremely parameter dependent. Some important steps in optimizing IRRAS peak intensities for better signal to noise are detailed here. The IR beam width coming out of the FTIR spectrometer is wide (~1 inch). The first mirror should be positioned at the correct focal length (marked by a spot in the FTIR chamber) or as close to as possible. Positioning away from the focal point causes beam divergence such that the beam width after reflection off the 2^{nd} mirror is wider than the KBr detector windows of the FTIR spectrometer, resulting in intensity loss. The mirror heights must be adjusted such that there is no leakage of the IR beam underneath the mirrors directly into the detector windows. The vertical profile of the mirrors is smaller than the beam width, thus beam leakage above the mirror occurs but is blocked from reaching the detector window by the mirror mounts. As mentioned in the theory of IRRAS section, an angle of close to ~47° is desired, but some adjustment may be needed depending on the height of the same stage whether a Langmuir trough or petri dish is used. Although the height, position and angle of the mirrors are accounted for, the IR beam is invisible, thus divergence of the beam still occurs. Manual optimization such as adjusting the horizontal rotation stage angles and leveling the mirrors is required to adequately focus the IR beam into the center of the detector windows.

In addition to optimization of the IRRAS optics, additional parameters must be accounted for when maximizing IRRAS peak intensities. To calibrate the IRRAS peak intensities, the IR beam energy when reflected off a gold mirror must be at least 15000 counts. The IR source lamp of the FTIR spectrometer can degrade over the years. Cleaning and replacement of the IR source resulted in significant enhancement of beam energies, and the resulting IRRAS spectral intensities. It is also sometimes necessary to perform ambient IRRAS: when a Langmuir trough is present, the sample compartment chamber of the FTIR spectrometer cannot be closed. Thus environmental conditions must be monitored. It was found that ambient room light had little impact on the quality of IRRAS spectra, whether the lights were on or off made no noticeable difference as long as they were constant. However the critical environmental parameter to monitor is CO_2 and water vapor. It is necessary to allow time for the headspace above the trough to equilibrate with the ambient air (~10 minutes). In a large room, the CO_2 and water vapor remain fairly constant, allowing for adequate background subtraction. However, if water vapor remains an issue in background subtraction due to conditions like high traffic movement through the workspace or changing humidity, it may be necessary to enclose and nitrogen purge the IRRAS setup. A makeshift solution was utilized by wrapping a large plastic bag around the entire FTIR spectrometer and allowing a 10minute N_2 purge. A low flowrate N_2 purge is recommended as higher flow rates will accelerate evaporation of the aqueous solution. Since the IR mirrors are calibrated and optimized for a specific sample stage height, evaporation and consequent lowering of the sample stage height will result in reduction of IR signal. A low flow rate is also recommended for enclosed purged experiments such as petri dish IRRAS.

Baseline correction of IRRAS spectra is performed in OriginPro 9.0.0 (OriginLab). An example spectrum is plotted in the phosphate region (1250-950 cm^{-1}) and then processed (Fig. C.1). To perform a baseline correction, the reflectance-absorbance peaks in the original spectrum (Fig. C.1) are removed from the spectrum as shown in Figure C.2. The remaining points in the spectrum are fit with a fourth order polynomial, as shown in Figure C.3. The fitted polynomial is considered the new baseline, and is subtracted from the original spectrum to obtain the baseline corrected spectrum, as shown in Figure C.4. A minimum of three baseline corrected spectra are averaged to obtain a final spectrum reported in figures. An anchor point ~1130 cm^{-1} was present in all fittings except spectra of DPPA on Al, Fe, and Zn.

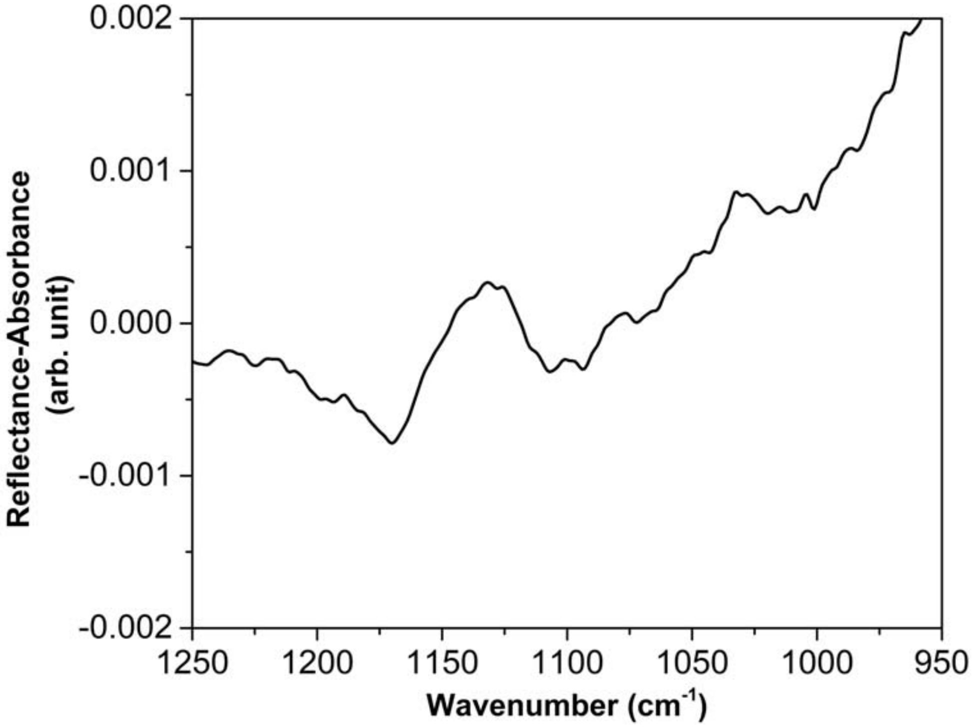

Figure C.1 Unprocessed IRRAS spectra of DPPA on pH 10 water in the phosphate region

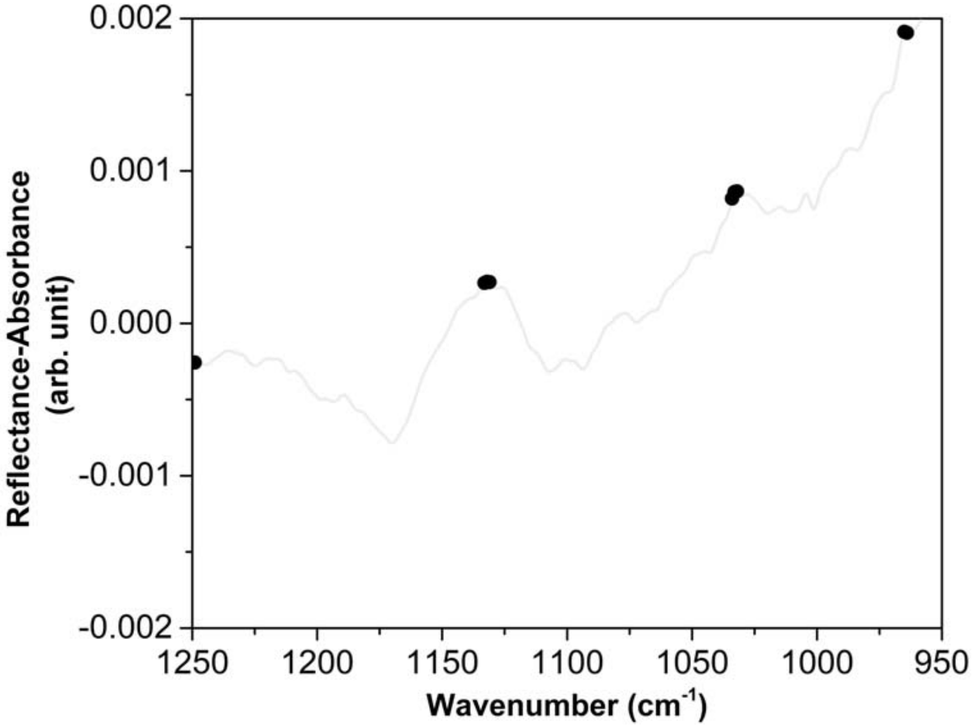

Figure C.2 Spectrum from Fig. B.1 after reflectance-absorbance peaks are removed.

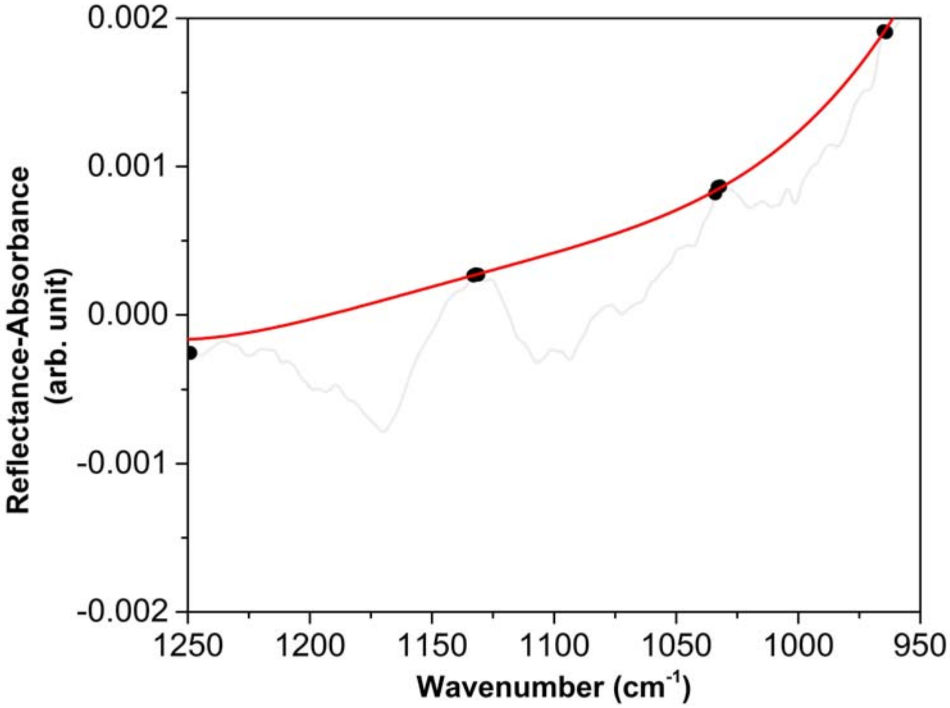

Figure C.3 Remaining points from Fig. B.2 fitted to a fourth-order polynomial

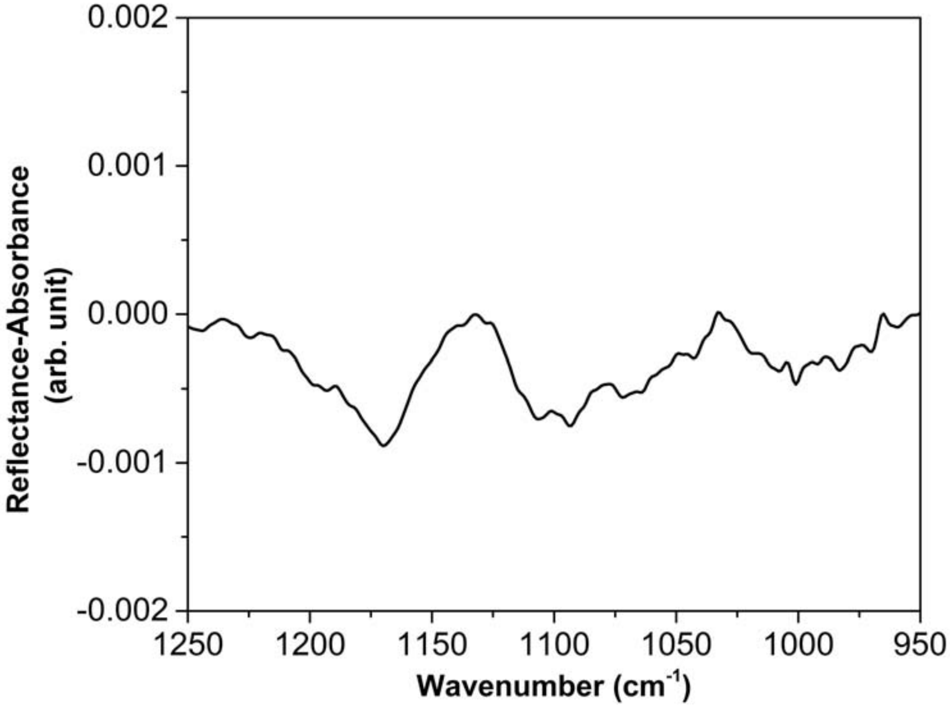

Figure C.4 Final baseline corrected IRRAS spectrum after the fourth-order polynomial is subtracted from the original spectrum (Fig. B.1)

Appendix D: Calculations of DPPA Monolayers Species Fractions and Surface Charge Density

D.1 DPPA Species Fractions

In order to determine the DPPA species fractions at a given bulk pH, one assumes a model DPPA (L) monolayer spread on an aqueous solution of fixed pH containing both hydronium (H^+) ions and sodium (Na^+) counter-cations. It is further assumed that these ions bind competitively with DPPA headgroups and that metal cations form 1:1 complexes. The equilibrium protonation (proton binding) and complexation (metal binding) reactions are given by

$$\mathrm{LH_2^0} \rightleftharpoons \mathrm{LH^-} + \mathrm{H^+}_{(aq)} \tag{D.1a}$$

$$\mathrm{LH^-} \rightleftharpoons \mathrm{L^{2-}} + \mathrm{H^+}_{(aq)} \tag{D.1b}$$

$$\mathrm{LNaH^0} \rightleftharpoons \mathrm{LH^-} + \mathrm{Na^+}_{(aq)} \tag{D.1c}$$

$$\mathrm{LNa^-} \rightleftharpoons \mathrm{L^{2-}} + \mathrm{Na^+}_{(aq)} \tag{D.1d}$$

where $\mathrm{LH_2^0}$ denotes the fully protonated DPPA species, whereas $\mathrm{LH^-}$ and $\mathrm{L^{2-}}$ refer to the singly deprotonated and fully deprotonated species, respectively. $\mathrm{LNaH^0}$ and $\mathrm{LNa^-}$ represent the lipid-Na^+-complexed species.

The equilibrium acid dissociation constants associated with the protonation reactions are given by

$$K_{a1} = \frac{[\mathrm{LH^-}]_s[\mathrm{H^+}]_{s*}}{[\mathrm{LH_2^0}]_s} \tag{D.2a}$$

$$K_{a2} = \frac{[\mathrm{L}^{2-}]_s[\mathrm{H}^+]_{s*}}{[\mathrm{LH}^-]_s} \tag{D.2b}$$

whereas the equilibrium complexation reactions are governed by the equilibrium metal binding constants are

$$K_{m1}^{-1} = \frac{[\mathrm{LH}^-]_s[\mathrm{Na}^+]_{s*}}{[\mathrm{LNaH}^0]_s} \tag{D.3a}$$

$$K_{m2}^{-1} = \frac{[\mathrm{L}^{2-}]_s[\mathrm{Na}^+]_{s*}}{[\mathrm{LNa}^-]_s} \tag{D.3b}$$

where the subscript s and s* refers, respectively, to interfacial (m^{-2}) and volume (but near the interface; M) concentrations. Effective pK_{a1} and pK_{a2} values for DPPA are believed to be around 2–3 and 7–9, respectively.[1] Effective metal binding constants to phosphatidic acid headgroups have been reviewed in Ref. 128 and estimated in Ref. 137.

The fractions of the different DPPA surface species (i.e., protonated, singly deprotonated, metal-complexed) are defined as

$$f_{\mathrm{LH}^-} = \frac{[\mathrm{LH}^-]_s}{[\mathrm{L}^{2-}]_s + [\mathrm{LH}^-]_s + [\mathrm{LH}_2^0]_s + [\mathrm{LNa}^-]_s + [\mathrm{LNaH}^0]_s} \tag{D.4a}$$

$$f_{\mathrm{LH}_2^0} = \frac{[\mathrm{LH}_2^0]_s}{[\mathrm{L}^{2-}]_s + [\mathrm{LH}^-]_s + [\mathrm{LH}_2^0]_s + [\mathrm{LNa}^-]_s + [\mathrm{LNaH}^0]_s} \tag{D.4b}$$

$$f_{\mathrm{LNa}^-} = \frac{[\mathrm{LNa}^-]_s}{[\mathrm{L}^{2-}]_s + [\mathrm{LH}^-]_s + [\mathrm{LH}_2^0]_s + [\mathrm{LNa}^-]_s + [\mathrm{LNaH}^0]_s} \tag{D.4c}$$

$$f_{\mathrm{LNaH}^0} = \frac{[\mathrm{LNaH}^0]_s}{[\mathrm{L}^{2-}]_s + [\mathrm{LH}^-]_s + [\mathrm{LH}_2^0]_s + [\mathrm{LNa}^-]_s + [\mathrm{LNaH}^0]_s} \tag{D.4d}$$

whereas the fully deprotonated and non-complexed DPPA fraction is given by

$$\begin{aligned} f_{\mathrm{L}^{2-}} &= 1 - \left(f_{\mathrm{LH}_2^0} + f_{\mathrm{LH}^-} + f_{\mathrm{LNa}^-} + f_{\mathrm{LNaH}^0}\right) \\ &= \frac{[\mathrm{L}^{2-}]_s}{[\mathrm{L}^{2-}]_s + [\mathrm{LH}^-]_s + [\mathrm{LH}_2^0]_s + [\mathrm{LNa}^-]_s + [\mathrm{LNaH}^0]_s} \end{aligned} \tag{D.4e}$$

Using Eqs. (D.2a,b) and (D.3a,b), and inserting into Eqs. (D.4a-e), the DPPA species fraction can be expressed as function of the acid and metal binding constants such as

$$f_{\mathrm{L}^{2-}} = \frac{K_{a1}K_{a2}[\mathrm{H}^+]_{s*}^{-2}}{1 + K_{a1}[\mathrm{H}^+]_{s*}^{-1} + K_{a1}K_{a2}[\mathrm{H}^+]_{s*}^{-2} + K_{a1}K_{m1}[\mathrm{H}^+]_{s*}^{-1}[\mathrm{Na}^+]_{s*} + K_{a1}K_{a2}K_{m2}[\mathrm{H}^+]_{s*}^{-2}[\mathrm{Na}^+]_{s*}} \tag{D.5a}$$

$$f_{\mathrm{LH}^-} = \frac{K_{a1}[\mathrm{H}^+]_{s*}^{-1}}{1 + K_{a1}[\mathrm{H}^+]_{s*}^{-1} + K_{a1}K_{a2}[\mathrm{H}^+]_{s*}^{-2} + K_{a1}K_{m1}[\mathrm{H}^+]_{s*}^{-1}[\mathrm{Na}^+]_{s*} + K_{a1}K_{a2}K_{m2}[\mathrm{H}^+]_{s*}^{-2}[\mathrm{Na}^+]_{s*}} \tag{D.5b}$$

$$f_{\mathrm{LH}_2^0} = \frac{1}{1 + K_{a1}[\mathrm{H}^+]_{s*}^{-1} + K_{a1}K_{a2}[\mathrm{H}^+]_{s*}^{-2} + K_{a1}K_{m1}[\mathrm{H}^+]_{s*}^{-1}[\mathrm{Na}^+]_{s*} + K_{a1}K_{a2}K_{m2}[\mathrm{H}^+]_{s*}^{-2}[\mathrm{Na}^+]_{s*}} \tag{D.5c}$$

$$f_{\mathrm{LNa}^-} = \frac{K_{a1}K_{a2}K_{m2}[\mathrm{H}^+]_{s*}^{-2}[\mathrm{Na}^+]_{s*}}{1 + K_{a1}[\mathrm{H}^+]_{s*}^{-1} + K_{a1}K_{a2}[\mathrm{H}^+]_{s*}^{-2} + K_{a1}K_{m1}[\mathrm{H}^+]_{s*}^{-1}[\mathrm{Na}^+]_{s*} + K_{a1}K_{a2}K_{m2}[\mathrm{H}^+]_{s*}^{-2}[\mathrm{Na}^+]_{s*}} \tag{D.5d}$$

$$f_{\mathrm{LNaH}^0} = \frac{K_{a1}K_{m1}[\mathrm{H}^+]_{s*}^{-1}[\mathrm{Na}^+]_{s*}}{1 + K_{a1}[\mathrm{H}^+]_{s*}^{-1} + K_{a1}K_{a2}[\mathrm{H}^+]_{s*}^{-2} + K_{a1}K_{m1}[\mathrm{H}^+]_{s*}^{-1}[\mathrm{Na}^+]_{s*} + K_{a1}K_{a2}K_{m2}[\mathrm{H}^+]_{s*}^{-2}[\mathrm{Na}^+]_{s*}} \tag{D.5e}$$

which after further rearrangement gives

$$\begin{aligned} &f_{\mathrm{L}^{2-}} \\ &= \frac{10^{(2\mathrm{pH}_{s*} - \mathrm{p}K_{a1} - \mathrm{p}K_{a2})}}{1 + 10^{(\mathrm{pH}_{s*} - \mathrm{p}K_{a1})}\left(1 + 10^{-(\mathrm{pNa}_{s*} + \mathrm{p}K_{m1})}\right) + 10^{(2\mathrm{pH}_{s*} - \mathrm{p}K_{a1} - \mathrm{p}K_{a2})}\left(1 + 10^{-(\mathrm{pNa}_{s*} + \mathrm{p}K_{m2})}\right)} \end{aligned} \tag{D.6a}$$

$$\begin{aligned} &f_{\mathrm{LH}^-} \\ &= \frac{10^{(\mathrm{pH}_{s*} - \mathrm{p}K_{a1})}}{1 + 10^{(\mathrm{pH}_{s*} - \mathrm{p}K_{a1})}\left(1 + 10^{-(\mathrm{pNa}_{s*} + \mathrm{p}K_{m1})}\right) + 10^{(2\mathrm{pH}_{s*} - \mathrm{p}K_{a1} - \mathrm{p}K_{a2})}\left(1 + 10^{-(\mathrm{pNa}_{s*} + \mathrm{p}K_{m2})}\right)} \end{aligned} \tag{D.6b}$$

$$f_{\mathrm{LH}_2^0} = \frac{1}{1 + 10^{(\mathrm{pH}_{s*} - \mathrm{p}K_{a1})}\left(1 + 10^{-(\mathrm{pNa}_{s*} + \mathrm{p}K_{m1})}\right) + 10^{(2\mathrm{pH}_{s*} - \mathrm{p}K_{a1} - \mathrm{p}K_{a2})}\left(1 + 10^{-(\mathrm{pNa}_{s*} + \mathrm{p}K_{m2})}\right)} \tag{D.6c}$$

$$f_{\mathrm{LNa}^-} = \frac{10^{(2\mathrm{pH}_{s*} - \mathrm{p}K_{a1} - \mathrm{p}K_{a2})}10^{-(\mathrm{pNa}_{s*} + \mathrm{p}K_{m2})}}{1 + 10^{(\mathrm{pH}_{s*} - \mathrm{p}K_{a1})}\left(1 + 10^{-(\mathrm{pNa}_{s*} + \mathrm{p}K_{m1})}\right) + 10^{(2\mathrm{pH}_{s*} - \mathrm{p}K_{a1} - \mathrm{p}K_{a2})}\left(1 + 10^{-(\mathrm{pNa}_{s*} + \mathrm{p}K_{m2})}\right)} \tag{D.6d}$$

$$f_{\mathrm{LNaH}^0} = \frac{10^{(\mathrm{pH}_{s*} - \mathrm{p}K_{a1})}10^{-(\mathrm{pNa}_{s*} + \mathrm{p}K_{m1})}}{1 + 10^{(\mathrm{pH}_{s*} - \mathrm{p}K_{a1})}\left(1 + 10^{-(\mathrm{pNa}_{s*} + \mathrm{p}K_{m1})}\right) + 10^{(2\mathrm{pH}_{s*} - \mathrm{p}K_{a1} - \mathrm{p}K_{a2})}\left(1 + 10^{-(\mathrm{pNa}_{s*} + \mathrm{p}K_{m2})}\right)} \tag{D.6e}$$

where, according to the usual definitions, $\mathrm{pH}_{s*} = -\log_{10}[\mathrm{H}^+]_{s*}$, $\mathrm{pNa}_{s*} = -\log_{10}[\mathrm{Na}^+]_{s*}$, and $\mathrm{p}K_a = -\log_{10} K_a$ and $\mathrm{p}K_m = -\log_{10} K_m$.

As the DPPA phosphate headgroups become increasingly negatively charged with the increase in the solution bulk pH, they will generate an interfacial electrostatic potential ψ_0 that imposes a new distribution of protons and cations near the interface. As a result, the interfacial ion (volume) concentrations will be significantly different from their bulk values. This effect must be taken into account by using Boltzmann equation

$$10^{-\mathrm{pH}_{s*}} = 10^{-\mathrm{pH}_b} e^{-F\psi_0/RT} \tag{D.7a}$$

$$10^{-\mathrm{pNa}_{s*}} = 10^{-\mathrm{pNa}_b} e^{-F\psi_0/RT} \tag{D.7b}$$

where pH_b and pNa_b refer to the bulk H^+ and Na^+ ion concentrations, respectively. F and R are the Faraday (9.649×10^4 A·mol^{-1}) and ideal gas (8.314 J·mol^{-1}·K^{-1}) constants, respectively, and T is the absolute temperature.

Using Eqs. (D.7a,b) with Eqs. (D.6a-e), the DPPA species fraction for a NaCl (1:1) salt solution can be expressed as function of the surface potential and bulk pH such as

$$f_{\mathrm{L}^{2-}} = \frac{10^{(2\mathrm{pH}_b - \mathrm{p}K_{a1} - \mathrm{p}K_{a2})} e^{2F\psi_0/RT}}{1 + 10^{(\mathrm{pH}_b - \mathrm{p}K_{a1})}\left(e^{F\psi_0/RT} + 10^{-(\mathrm{pNa}_b + \mathrm{p}K_{m1})}\right) + 10^{(2\mathrm{pH}_b - \mathrm{p}K_{a1} - \mathrm{p}K_{a2})}\left(e^{2F\psi_0/RT} + 10^{-(\mathrm{pNa}_b + \mathrm{p}K_{m2})} e^{F\psi_0/RT}\right)} \tag{D.8a}$$

$$f_{\mathrm{LH}^{-}} = \frac{10^{(\mathrm{pH}_b - \mathrm{p}K_{a1})} e^{F\psi_0/RT}}{1 + 10^{(\mathrm{pH}_b - \mathrm{p}K_{a1})}\left(e^{F\psi_0/RT} + 10^{-(\mathrm{pNa}_b + \mathrm{p}K_{m1})}\right) + 10^{(2\mathrm{pH}_b - \mathrm{p}K_{a1} - \mathrm{p}K_{a2})}\left(e^{2F\psi_0/RT} + 10^{-(\mathrm{pNa}_b + \mathrm{p}K_{m2})} e^{F\psi_0/RT}\right)} \tag{D.8b}$$

$$f_{\mathrm{LH}_2^0} = \frac{1}{1 + 10^{(\mathrm{pH}_b - \mathrm{p}K_{a1})}\left(e^{F\psi_0/RT} + 10^{-(\mathrm{pNa}_b + \mathrm{p}K_{m1})}\right) + 10^{(2\mathrm{pH}_b - \mathrm{p}K_{a1} - \mathrm{p}K_{a2})}\left(e^{2F\psi_0/RT} + 10^{-(\mathrm{pNa}_b + \mathrm{p}K_{m2})} e^{F\psi_0/RT}\right)} \tag{D.8c}$$

$$f_{\mathrm{LNa}^{-}} = \frac{10^{(2\mathrm{pH}_b - \mathrm{p}K_{a1} - \mathrm{p}K_{a2})} 10^{-(\mathrm{pNa}_b + \mathrm{p}K_{m2})} e^{F\psi_0/RT}}{1 + 10^{(\mathrm{pH}_b - \mathrm{p}K_{a1})}\left(e^{F\psi_0/RT} + 10^{-(\mathrm{pNa}_b + \mathrm{p}K_{m1})}\right) + 10^{(2\mathrm{pH}_b - \mathrm{p}K_{a1} - \mathrm{p}K_{a2})}\left(e^{2F\psi_0/RT} + 10^{-(\mathrm{pNa}_b + \mathrm{p}K_{m2})} e^{F\psi_0/RT}\right)} \tag{D.8d}$$

$$f_{\mathrm{LNaH}^0} = \frac{10^{(\mathrm{pH}_b - \mathrm{p}K_{a1})} 10^{-(\mathrm{pNa}_b + \mathrm{p}K_{m1})}}{1 + 10^{(\mathrm{pH}_b - \mathrm{p}K_{a1})}\left(e^{F\psi_0/RT} + 10^{-(\mathrm{pNa}_b + \mathrm{p}K_{m1})}\right) + 10^{(2\mathrm{pH}_b - \mathrm{p}K_{a1} - \mathrm{p}K_{a2})}\left(e^{2F\psi_0/RT} + 10^{-(\mathrm{pNa}_b + \mathrm{p}K_{m2})} e^{F\psi_0/RT}\right)} \tag{D.8e}$$

In the absence of cations ($[\mathrm{Na}^+]_b = K_{m1} = K_{m2} = 0$), Eqs. (D.8a-e) simply give the DPPA species fraction on water

$$f_{\mathrm{L}^{2-}} = \frac{10^{(2\mathrm{pH}_b - \mathrm{p}K_{a1} - \mathrm{p}K_{a2})} e^{2F\psi_0/RT}}{1 + 10^{(\mathrm{pH}_b - \mathrm{p}K_{a1})} e^{F\psi_0/RT} + 10^{(2\mathrm{pH}_b - \mathrm{p}K_{a1} - \mathrm{p}K_{a2})} e^{2F\psi_0/RT}} \tag{D.9a}$$

$$f_{\mathrm{LH}^{-}} = \frac{10^{(\mathrm{pH}_b - \mathrm{p}K_{a1})} e^{F\psi_0/RT}}{1 + 10^{(\mathrm{pH}_b - \mathrm{p}K_{a1})} e^{F\psi_0/RT} + 10^{(2\mathrm{pH}_b - \mathrm{p}K_{a1} - \mathrm{p}K_{a2})} e^{2F\psi_0/RT}} \tag{D.9b}$$

$$f_{\mathrm{LH}_2^0} = \frac{1}{1 + 10^{(\mathrm{pH}_b - \mathrm{p}K_{a1})} e^{F\psi_0/RT} + 10^{(2\mathrm{pH}_b - \mathrm{p}K_{a1} - \mathrm{p}K_{a2})} e^{2F\psi_0/RT}} \tag{D.9c}$$

D.2 DPPA Surface Charge Density

The fraction (α) of charged (i.e., deprotonated and metal-complexed) species present in the DPPA monolayer is given by

$$\begin{aligned} \alpha &= \frac{[\mathrm{L}^{2-}]_s + [\mathrm{LH}^-]_s + [\mathrm{LNa}^-]_s}{[\mathrm{L}^{2-}]_s + [\mathrm{LH}^-]_s + [\mathrm{LH}_2^0]_s + [\mathrm{LNa}^-]_s + [\mathrm{LNaH}^0]_s} \\ &= \frac{1 + K_{a2}^{-1}[\mathrm{H}^+]_{s*} + K_{m2}[\mathrm{Na}^+]_{s*}}{1 + K_{a2}^{-1}[\mathrm{H}^+]_{s*} + K_{a1}^{-1}K_{a2}^{-1}[\mathrm{H}^+]_{s*}^2 + K_{m2}[\mathrm{Na}^+]_{s*} + K_{a2}^{-1}K_{m1}[\mathrm{H}^+]_{s*}[\mathrm{Na}^+]_{s*}} \end{aligned} \tag{D.10}$$

or, equivalently,

$$\alpha = \frac{10^{(\mathrm{pH}_s - \mathrm{p}K_{a1})} + 10^{(2\mathrm{pH}_s - \mathrm{p}K_{a1} - \mathrm{p}K_{a2})}\left(1 + 10^{-(\mathrm{pNa}_s + \mathrm{p}K_{m2})}\right)}{1 + 10^{(\mathrm{pH}_s - \mathrm{p}K_{a1})}\left(1 + 10^{-(\mathrm{pNa}_s + \mathrm{p}K_{m1})}\right) + 10^{(2\mathrm{pH}_s - \mathrm{p}K_{a1} - \mathrm{p}K_{a2})}\left(1 + 10^{-(\mathrm{pNa}_s + \mathrm{p}K_{m2})}\right)} \qquad \text{(D.11)}$$

Using Eqs. (C.7a,b), Eq. (C.11) can finally be written in terms of bulk pH and surface potential as

$$\alpha(\psi_0) = \frac{10^{(\mathrm{pH}_b - \mathrm{p}K_{a1})} e^{F\psi_0/RT} + 10^{(2\mathrm{pH}_b - \mathrm{p}K_{a1} - \mathrm{p}K_{a2})}\left(e^{2F\psi_0/RT} + 10^{-(\mathrm{pNa}_b + \mathrm{p}K_{m2})} e^{F\psi_0/RT}\right)}{1 + 10^{(\mathrm{pH}_b - \mathrm{p}K_{a1})}\left(e^{F\psi_0/RT} + 10^{-(\mathrm{pNa}_b + \mathrm{p}K_{m1})}\right) + 10^{(2\mathrm{pH}_b - \mathrm{p}K_{a1} - \mathrm{p}K_{a2})}\left(e^{2F\psi_0/RT} + 10^{-(\mathrm{pNa}_b + \mathrm{p}K_{m2})} e^{F\psi_0/RT}\right)} \qquad \text{(D.12)}$$

Knowing α, the surface charge density of the DPPA monolayer spread on a NaCl solution is then given by

$$\sigma(\psi_0) = \sigma_0 \alpha = -\frac{2e}{A_L}\left[\frac{\left(10^{(\mathrm{pH}_b - \mathrm{p}K_{a1})} + 10^{(2\mathrm{pH}_b - \mathrm{p}K_{a1} - \mathrm{p}K_{a2})} 10^{-(\mathrm{pNa}_b + \mathrm{p}K_{m2})}\right) e^{F\psi_0/RT} + 10^{(2\mathrm{pH}_b - \mathrm{p}K_{a1} - \mathrm{p}K_{a2})} e^{2F\psi_0/RT}}{1 + 10^{(\mathrm{pH}_b - \mathrm{p}K_{a1})}\left(e^{F\psi_0/RT} + 10^{-(\mathrm{pNa}_b + \mathrm{p}K_{m1})}\right) + 10^{(2\mathrm{pH}_b - \mathrm{p}K_{a1} - \mathrm{p}K_{a2})}\left(e^{2F\psi_0/RT} + 10^{-(\mathrm{pNa}_b + \mathrm{p}K_{m2})} e^{F\psi_0/RT}\right)}\right] \qquad \text{(D.13)}$$

where σ_0 is the maximal surface charge density of the DPPA monolayer and e is the electronic charge. When the DPPA headgroups are fully dissociated, $\sigma_0 = -2e/A_L$. From Eq. (C.13), it is clear that ion binding reduces the value of the surface charge density σ_0.

For the case of DPPA on water (i.e., in the absence of Na^+ cations), Eq. (D.13) reduces to

$$\sigma(\psi_0) = \sigma_0 \alpha = -\frac{2e}{A_L}\left[\frac{10^{(\mathrm{pH}_b - \mathrm{p}K_{a1})} e^{F\psi_0/RT} + 10^{(2\mathrm{pH}_b - \mathrm{p}K_{a1} - \mathrm{p}K_{a2})} e^{2F\psi_0/RT}}{1 + 10^{(\mathrm{pH}_b - \mathrm{p}K_{a1})} e^{F\psi_0/RT} + 10^{(2\mathrm{pH}_b - \mathrm{p}K_{a1} - \mathrm{p}K_{a2})} e^{2F\psi_0/RT}}\right] \qquad \text{(D.14)}$$

Appendix E: Rights & Permissions

Reprinted (adapted) with permission from (Zhang, T; Brantley, S.B.; Verreault, D.; Allen, H.C. "Effect of pH and Salt on Surface-pKa of Phosphatidic Acid Monolayers" Langmuir, 2018, 34 (1), 530–539.) Copyright (2018) American Chemical Society.

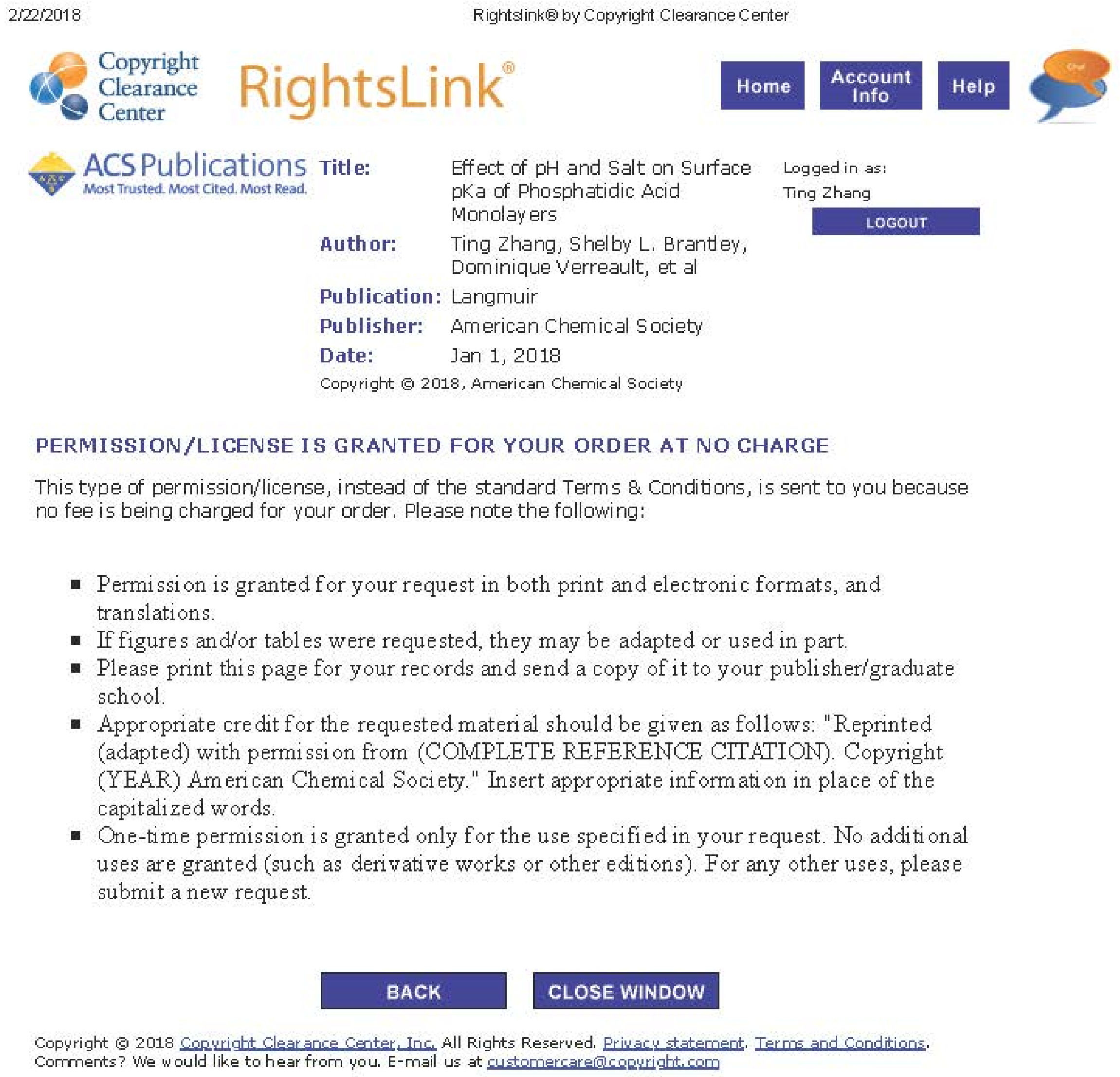

2/22/2018 Rightslink® by Copyright Clearance Center

Title: Effect of pH and Salt on Surface pKa of Phosphatidic Acid Monolayers

Author: Ting Zhang, Shelby L. Brantley, Dominique Verreault, et al

Publication: Langmuir

Publisher: American Chemical Society

Date: Jan 1, 2018

Copyright © 2018, American Chemical Society

Logged in as:
Ting Zhang

PERMISSION/LICENSE IS GRANTED FOR YOUR ORDER AT NO CHARGE

This type of permission/license, instead of the standard Terms & Conditions, is sent to you because no fee is being charged for your order. Please note the following:

- Permission is granted for your request in both print and electronic formats, and translations.
- If figures and/or tables were requested, they may be adapted or used in part.
- Please print this page for your records and send a copy of it to your publisher/graduate school.
- Appropriate credit for the requested material should be given as follows: "Reprinted (adapted) with permission from (COMPLETE REFERENCE CITATION). Copyright (YEAR) American Chemical Society." Insert appropriate information in place of the capitalized words.
- One-time permission is granted only for the use specified in your request. No additional uses are granted (such as derivative works or other editions). For any other uses, please submit a new request.

Copyright © 2018 Copyright Clearance Center, Inc. All Rights Reserved. Privacy statement. Terms and Conditions.
Comments? We would like to hear from you. E-mail us at customercare@copyright.com